Technical Physics Letters, Vol. 26, No. 6, 2000, pp. 447–451. Translated from Pis'ma v Zhurnal Tekhnicheskoĭ Fiziki, Vol. 26, No. 11, 2000, pp. 1–9.

Transmittance of Dispersed Nematic/Polymer Systems of the NCAP Type

O. A. Afonin and V. F. Nazvanov

Saratov State University, Saratov, 410601 Russia

Received September 9, 1999

Abstract—A stationary effect of the electric-field-induced variation of the transmittance of thin-film disperse systems was studied theoretically. The systems consisting of a nematic liquid crystal (NLC) and a polymer (NCAP-type systems) represent flattened spheroid droplets with a bipolar NLC structure. These systems are characterized by a nonmonotonic dependence of the optical transmittance on the applied field strength for the normal incidence of light. This dependence is interpreted within the framework of a proposed phenomenological model based on the approximations of single scattering and anomalous diffraction. Experimental verification of the model is performed for dispersed systems with a poly(vinyl alcohol) matrix. A good agreement of the theoretical and experimental results is obtained. © *2000 MAIK "Nauka/Interperiodica".*

The study of electric-field-controlled attenuation and scattering of light in dispersed systems representing the suspensions of droplets of nematic liquid crystals (NLCs) in polymer matrices [1, 2] is an important modern trend in the optics of liquid crystals. We will consider NLC/polymer thin-film dispersed systems of the so-called NCAP (Nematic Curvilinear Aligned Phase) type formed by droplets of a bipolar NLC structure slightly flattened along the normal $\hat{\mathbf{m}}$ to the film. If the NLC exhibits positive anisotropy of the dielectric permittivity $\Delta\varepsilon > 0$ and the electric field $\mathbf{E}$ is parallel to $\hat{\mathbf{m}}$, then the electrooptical response of such systems is characterized by a pronounced minimum (sometimes, with oscillations) of the field dependence of the optical transmittance $T(E)$ [3–7]. This fact can be used for significant improvement of the contrast ratio of projection displays based on LC dispersions.

Earlier experiments [2, 3, 5, 8, 9] made it possible to determine a scenario of the field orientation of a bipolar NLC droplet having the shape of a flattened spheroid with semiaxes a and b, $b \le a$ (Fig. 1a). There are three stages in this process: (I) azimuth-degenerate orientation of a droplet director $\hat{\mathbf{N}}$ in the film plane for small values of the electric field strength ($0 \le E < E_{c1}$); (II) threshold reorientation of an NLC local director $\hat{\mathbf{n}}(\mathbf{r})$ in the central part of a droplet at a certain critical value $E_{c1}(b)$, with retained initial positions of the poles in the bipolar NLC structure; (III) orientational transition $\hat{\mathbf{N}} \perp \mathbf{E} \longrightarrow \hat{\mathbf{N}} \parallel \mathbf{E}$ at a field strength $E_{c2}(b) \ge E_{c1}$, followed by smooth increase of the orientation ordering $\hat{\mathbf{n}}(\mathbf{r})$ along $\mathbf{E}$. In the case of a strong azimuthal surface binding of NLC and polymer molecules and/or significant anisometry of polymer capsules, it is possible that $E_{c2} \longrightarrow \infty$, which implies that the orientational process is restricted to the stages (I) and (II) [5, 10].

In this work, we have performed for the first time an approximate theoretical analysis of the above-mentioned electrooptical phenomena for the case when the wave vector of the incident light $\mathbf{k}_0$ is parallel to the direction of the orienting field $\mathbf{E}$. In continuation of our preceding works [11, 12], we compare the results of the theoretical analysis with the experimental data obtained previously.

With neglect of the effects of multiple light scattering [13, 14], the transmittance (transparency) of an NLC/polymer dispersed system for nonpolarized or linearly polarized light at normal incidence onto a layer ($\mathbf{k}_0 \parallel \mathbf{E}$) is given by the Bouguer law: $T = T_0\exp(-\tau)$, where τ is the optical thickness of the dispersed medium and the coefficient T_0 takes into account the Fresnel reflection at flat interfaces and the absorption in transparent electrodes of an electrooptical cell. An expression for τ, which corresponds to the scenario of the field orientation of bipolar NLC droplets (Fig. 1a) can be presented as [11, 12]:

$$\tau = \frac{3C_V d}{4\langle b^3\rangle}\left\{\frac{1}{2}\int_0^{b_c^-(E)} b^2[Q_1(E, \vartheta_N = \pi/2) + Q_2(E, \vartheta_N = \pi/2)]h(b)db + (1 - C_V)\int_{b_c^+(E)}^{\infty} b^2 Q_{1\equiv 2}(E, \vartheta_N = 0)h(b)db\right\}, \quad (1)$$

1063-7850/00/2606-0447$20.00 © 2000 MAIK "Nauka/Interperiodica"

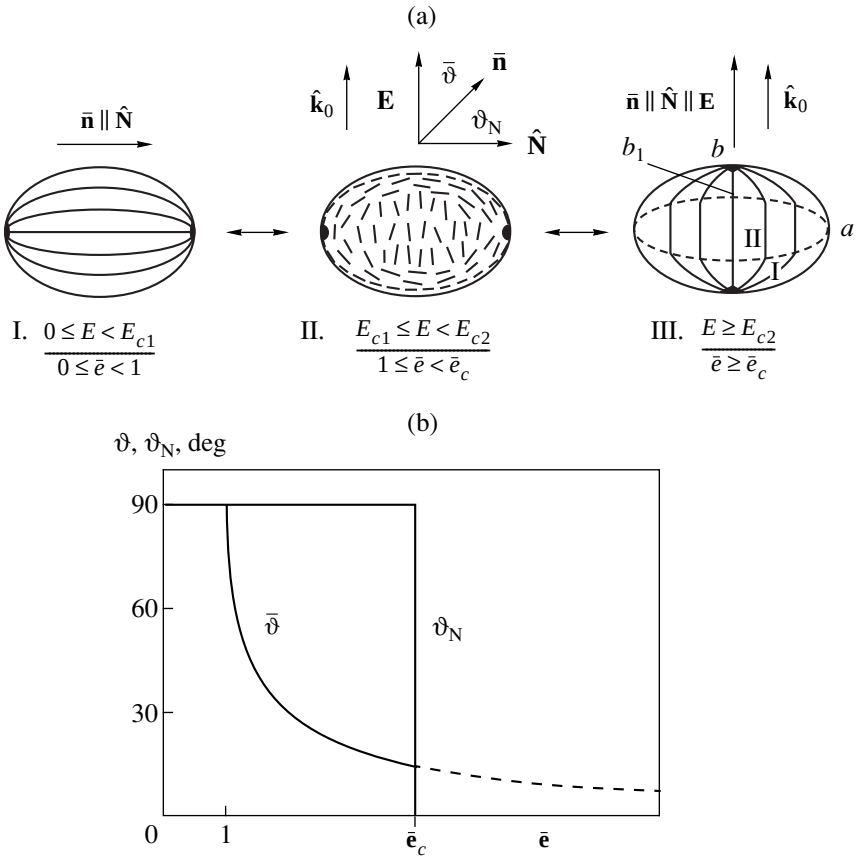

Fig. 1. (a) A schematic diagram of structural changes in a bipolar NLC droplet of a flattened spheroid shape in an external electric field **E**, showing cross sections by the ($\hat{\mathbf{N}}$, **E**) plane. Vector $\hat{\mathbf{N}}$ (droplet director) indicates the direction of a line connecting point defects of the NLC at the surface of a polymer capsule (see text for further details). (b) Plots of the mean orientation angle $\bar{\vartheta}$ of NLC molecules in a droplet and the orientation angle ϑ_N of the droplet director $\hat{\mathbf{N}}$ versus the reduced field strength $\bar{e}$.

where $0 < C_V < 1$ is a volume fraction of droplets; d is the thickness of the layer; $Q_1(E, \vartheta_N)$ and $Q_2(E, \vartheta_N)$ are the attenuation efficiency factors for the components polarized parallel and perpendicularly to the plane ($\mathbf{k_0}$, $\hat{\mathbf{N}}$), respectively; $h(b)$ is the droplet size distribution function; and $b_c(E)$ is a droplet size at which the field of the strength E causes a threshold reorientation $\hat{\mathbf{N}} \perp \mathbf{E} \longrightarrow \hat{\mathbf{N}} \parallel \mathbf{E}$. Coefficient $1 - C_V$ in the second term of (1) takes into account an increase in transparency ("clarification") of a dispersed medium at $C_V \longrightarrow 1$ [15, 16].

Let us consider first a field dependence of the attenuation efficiency factors $Q_1(E, \vartheta_N = \pi/2)$ and $Q_2(E, \vartheta_N = \pi/2)$ describing the droplets with the orientation $\hat{\mathbf{N}} \perp \mathbf{E}$ at $0 < E < E_{c2}$ (stages I and II in Fig. 1a). Precise calculation of a vector field of the NLC local director in a droplet $\hat{\mathbf{n}}(E, \mathbf{r})$ and the corresponding functions $Q_1(E)$ and $Q_2(E)$ appears to be a rather complicated physical problem. An approximate solution can be obtained using a concept of the mean (over the droplet volume V) direction of orientation of the NLC molecules $\bar{\mathbf{n}}(E) = \langle \hat{\mathbf{n}}(E, \mathbf{r}) \rangle_V$, which makes it possible to employ a uniform uniaxial anisotropic spheroid with an optical axis oriented parallel to $\bar{\mathbf{n}}(E)$ as an optical model of the NLC droplet. In this case, vector $\hat{\mathbf{N}}$ is not collinear with the mean orientation direction $\bar{\mathbf{n}}(E)$ (Fig. 1a, II). Within the framework of this model, the attenuation efficiency factors Q_1 and Q_2 at a wavelength λ are given, in the approximation of anomalous diffraction, by a well-known formula [17, 18]:

$$Q_i = 2 - 4\rho_i^{-1}\sin\rho_i = 4\rho_i^{-2}(1 - \cos\rho_i), \quad i = 1, 2, \quad (2)$$

where

$$\begin{Bmatrix} \rho_1 \\ \rho_2 \end{Bmatrix} = 4\pi\lambda^{-1} b \left[\begin{Bmatrix} n_e^*(\bar{\vartheta}) \\ n_o \end{Bmatrix} - n_p \right], \quad (3)$$

$$n_e^*(\bar{\vartheta}) = \frac{n_o n_e}{[n_o^2 + (n_e^2 - n_o^2)\cos^2\bar{\vartheta}]^{1/2}}, \quad (4)$$

$\cos\bar{\vartheta} = \bar{\mathbf{n}} \cdot \mathbf{E}/E$; n_o and n_e are the NLC refractive indices for ordinary and extraordinary waves, respectively; and n_p is the refractive index of the polymer matrix.

The function $\bar{\vartheta}(E)$ can be obtained from the solution of a balance equation for elastic Γ_K and dielectric Γ_E torsional moments acting upon a liquid crystal inside a droplet: $\Gamma_K + \Gamma_E = 0$. We used the simplest tangential form of the elastic moment [19] $\Gamma_K \approx -\frac{3}{4}\pi A^2 RK \tan(\vartheta_N - \bar{\vartheta})$ and defined the dielectric moment as $\Gamma_E \approx \frac{2}{3}\pi R^3 g^2 \varepsilon_0 (\varepsilon_\parallel - \varepsilon_\perp) E^2 \sin 2\bar{\vartheta}$, where A is a constant close to unity; $R = l^{2/3}b$ is the radius of a sphere of equivalent volume; K is the mean modulus of elasticity of NLC; $g = 3\varepsilon_p/(2\varepsilon_p + \bar{\varepsilon}_{LC})$; $\bar{\varepsilon}_{LC} = (\varepsilon_\parallel + 2\varepsilon_\perp)/3$; and $\varepsilon_\parallel$, $\varepsilon_\perp$, and ε_p are the principal dielectric permittivities of NLC and the polymer dielectric permittivity, respectively. In this case, the static equation for $\bar{\vartheta}$ can be represented as $\tan(\vartheta_N - \bar{\vartheta}) - \frac{1}{2}\bar{e}^2 \sin 2\bar{\vartheta} = 0$, where $\bar{e} = gERA^{-1}[\varepsilon_0(\varepsilon_\parallel - \varepsilon_\perp)K^{-1}]^{1/2}$ is a reduced field related to the orientation of $\bar{\mathbf{n}}$. A solution of this equation at $\vartheta_N = \pi/2$ that is of interest for us is given by:

$$\cos^2\bar{\vartheta} = (\bar{e}^2 - 1)/\bar{e}^2, \quad \bar{e} \geq 1. \tag{5}$$

Figure 1b shows the curves of $\bar{\vartheta}(\bar{e}, \vartheta_N = \pi/2)$ and $\vartheta_N(\bar{e})$. It is seen that structural changes of a single bipolar NLC droplet start at $\bar{e} = 1$ ($E = E_{c1}$). After that, a smooth decrease of the angle $\bar{\vartheta}$ leads, according to (3) and (4), to a decrease of a phase delay of an extraordinary ray in the droplet. At a certain value $\bar{e} = \bar{e}_c$ ($E = E_{c2}$), a threshold orientational transition $\hat{\mathbf{N}} \perp \mathbf{E} \longrightarrow \hat{\mathbf{N}} \parallel \mathbf{E}$ takes place. We demonstrated earlier [10] that $\bar{e}_c$ is given by $\bar{e}_c = [5.7(l^2 - 1)l^{-2} + 2.1W_a RK^{-1}]^{1/2}$, where W_a is the coefficient of an azimuthal surface binding of NLC and polymer molecules. The corresponding value of $b_c(E)$ in (1) is a solution of the following equation:

$$E = \frac{A}{gbl^{2/3}}\left[\frac{5.7K(l^2 - 1)l^{-2} + 2.1W_a bl^{2/3}}{\varepsilon_0(\varepsilon_\parallel - \varepsilon_\perp)}\right]^{1/2}. \tag{6}$$

We used a structural model developed previously [11] (Fig 1a, (III)) to describe the oriented state of a bipolar NLC droplet ($\hat{\mathbf{N}} \parallel \mathbf{E}$). Assume that a droplet consists of a central part, with a uniform uniaxial orientation of the local director $\hat{\mathbf{n}}$ along $\hat{\mathbf{N}}$ induced by the applied field $\mathbf{E}$, and an outer part with an undisturbed bipolar orientation $\hat{\mathbf{n}}(\mathbf{r})$ maintained by a strong tangential surface binding of NLC and polymer molecules. The interface between these areas is determined by a flattened spheroid (inscribed into the droplet) with semiaxes:

$$a_1 = a, \quad b_1 = b\bar{e}/(\bar{e} + 1). \tag{7}$$

Thus, the droplet exhibits a bipolar structure with $\hat{\mathbf{n}}(\mathbf{r})$ at $\bar{e} = 0$. If $\bar{e} \longrightarrow \infty$, the droplet can be considered as a uniform uniaxial anisotropic particle with the orientation $\hat{\mathbf{n}} \parallel \mathbf{E}$. The corresponding attenuation efficiency factor $Q_{1 \equiv 2}(\vartheta_N = 0)$ is calculated in the approximation of anomalous diffraction with the use of equations (10) and (12)–(16) from [11] modified so as to take into account the flattened shape of a droplet.

We carried out an experimental verification of the proposed model of the transparency variation effect for NLC/polymer dispersed systems prepared by emulsification of a commercially available mixture of SZhK-(1–4) cyanobiphenyls in a 10% aqueous solution of poly(vinyl alcohol) (PVA). A suspension of bipolar NLC droplets in a thin PVA film was obtained by dehydration. The droplets size distribution function $h(b)$ exhibited a maximum at $b_m \approx 0.5$ μm and could be described well by a generalized gamma-distribution [20]:

$$h(b) = \frac{\eta(\mu/\eta)^{(\mu+1)/\eta}}{\Gamma[(\mu + 1)/\eta]}\left(\frac{b}{b_m}\right)^\mu \frac{1}{b_m}\exp\left[-\frac{\mu}{\eta}\left(\frac{b}{b_m}\right)^\eta\right] \tag{8}$$

with the parameters $\mu = 4$ and $\eta = 0.515$. The film was placed between two glass plates with transparent ITO electrodes deposited on the inner surfaces. The thickness of the film d and the volume concentration of droplets C_V were varied from 15 to 65 μm and from 0.15 to 0.45, respectively. A sinusoidal electric field with a frequency of 1 kHz and a strength of up to 10^6 V/μm provided variation of the transparency of the cells. The transmittance T was measured using a He–Ne laser (λ = 633 nm) at a temperature of 25°C and a detector collection angle of 20′.

Figure 2a shows the curves of reduced optical thickness $\tau(E)/C_V d$ (where $\tau = -\ln(T/T_0)$) versus field strength obtained by averaging of the experimental data for a series of samples with different values of C_V and d. The values of the concentration parameter $C_V d$ correspond to a linear fragment of the curve $\tau(C_V d, E = 0)$, shown in the inset in Fig. 2. The theoretical curve $\tau(E)/C_V d$ (solid line in Fig. 2a) was calculated for the following set of parameters corresponding to the experimental conditions: $n_0 = 1.52$, $n_e = 1.72$, $n_p = 1.51$, λ = 633 nm, $l = 1.5$, $b_m = 0.5$, $\mu = 4$, $\eta = 0.515$, $K = 10^{-11}$ H, $W_a = 10^{-5}$ N/m, $\varepsilon_\perp = 5$, $\varepsilon_\parallel = 19$, and $\varepsilon_p = 8$. The value of

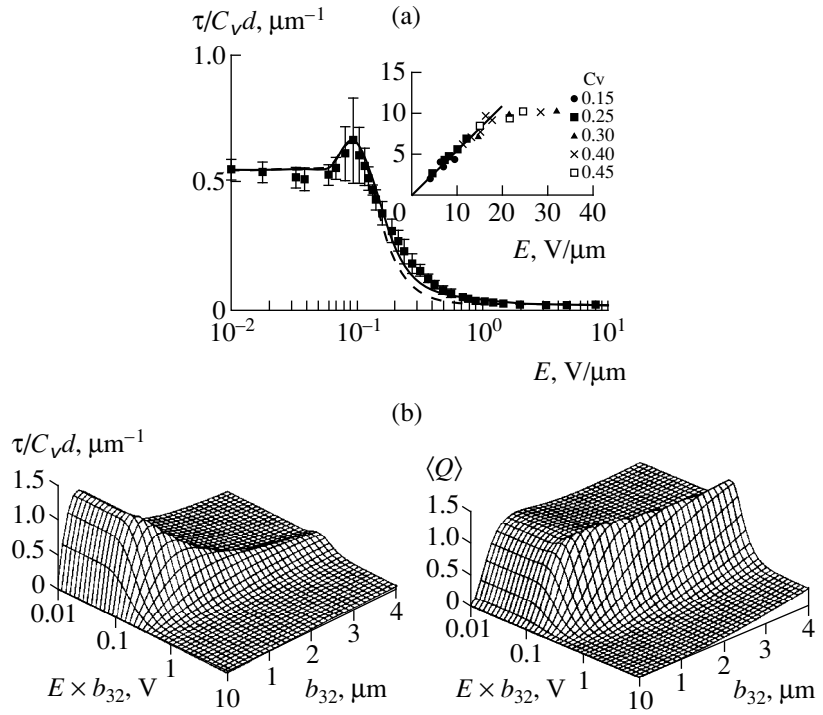

Fig. 2. (a) Plots of the reduced optical thickness $\tau/C_V d$ of an SZhK-(1–4)/PVA thin-film disperse system versus root-mean-square strength of the applied sinusoidal electric field E with a frequency of 1 kHz at the normal incidence of light with the wavelength $\lambda = 633$ nm: (symbols) experimental data, (solid line) theoretical calculations (see text for the values of parameters), (dashed line) theoretical calculations at $\bar{e}_c \longrightarrow \infty$. The inset shows an experimental curve of $\tau(C_V d)$ at $E = 0$. (b) Theoretical maps of the optical thickness $\tau/C_V d$ and the mean attenuation efficiency factor $\langle Q(\vartheta_N = \pi/2)\rangle$ versus the field strength E and the mean droplet size b_{32}.

the fitting parameter was $A = 0.5$. The dashed curve in Fig. 2a was calculated for $\bar{e}_c \longrightarrow \infty$ (or $b_c(E) \longrightarrow \infty$), which corresponds to a static position of poles in the bipolar structure of a droplet [5].

Figure 2b shows the curves of the optical thickness $\tau(E)/C_V d$ of a SZhK-(1–4)/PVA system and the mean attenuation efficiency factor $\langle Q(\vartheta_N = \pi/2)\rangle = \frac{1}{2}[Q_1(\vartheta_N = \pi/2) + Q_2(\vartheta_N = \pi/2)]$ versus the field strength E and the mean size of a droplet $b_{32} = \langle b^3\rangle/\langle b^2\rangle$ for a group of droplets belonging to the orientational states I and II (Fig. 1a). It is clearly seen that a nonmonotonic character of $\tau(E)$ is typical of large droplets and is related to certain features in behavior of the function $\langle Q(E, b_{32})\rangle$. The nonmonotonic character of $\tau(E)$ disappears with decreasing b_{32} and the corresponding curve $T(E)$ becomes S-shaped. The calculations show that the value of the parameter $\nu = b_{32}(n_e - n_p)\lambda^{-1}$ that determines a boundary between the areas of monotonic and nonmonotonic behavior of $\tau(E)$ and $T(E)$ is $\nu \approx 0.2$.

Thus, a good agreement between the theoretical and experimental results provides evidence of the adequacy of the model proposed for a description of the electric-field-controlled variation of the transparency of NCAP-type liquid-crystalline disperse systems.

REFERENCES

1. G. M. Zharkova and A. S. Sonin, *Liquid-Crystalline Composites* (Nauka, Novosibirsk, 1994).
2. P. S. Drzaic, *Liquid Crystal Dispersions* (World Scientific, Singapore, 1995).
3. P. S. Drzaic, Liq. Cryst. **3**, 1543 (1988).
4. A. V. Kaznacheev, G. B. Nosov, and A. S. Sonin, Opt. Zh., No. 7, 29 (1993).
5. V. Ya. Zyryanov, V. V. Presnyakov, and V. F. Shabanov, Pis'ma Zh. Tekh. Fiz. **22** (14), 22 (1996) [Tech. Phys. Lett. **22**, 563 (1996)].
6. O. A. Aphonin and V. F. Nazvanov, Mol. Cryst. Liq. Cryst. **303**, 29 (1997).
7. O. A. Afonin, in *Problems of Physical Optics. Proceedings of the International School for Young Scientists in Optics, Laser Physics, and Electronics, Saratov, 1997* (Saratov. Gos. Univ., Saratov, 1997), pp. 178–180.
8. A. V. Koval'chuk, M. V. Kurik, O. D. Lavrentovich, and V. V. Sergan, Zh. Éksp. Teor. Fiz. **94** (5), 350 (1988) [Sov. Phys. JETP **67**, 1065 (1988)].
9. S. C. Jain and D. K. Rout, J. Appl. Phys. **70**, 6988 (1991).
10. O. A. Afonin and V. F. Nazvanov, Pis'ma Zh. Tekh. Fiz. **24** (11), 87 (1998) [Tech. Phys. Lett. **24**, 451 (1998)].

11. O. A. Afonin and V. F. Nazvanov, Zh. Tekh. Fiz. **60** (10), 93 (1990) [Sov. Phys. Tech. Phys. **35**, 1168 (1990)].
12. O. A. Aphonin and V. F. Nazvanov, Liq. Cryst. **23**, 845 (1997).
13. A. P. Ivanov, V. A. Loĭko, and V. P. Dik, *Light Propagation in Closely Packed Disperse Media* (Nauka i Tekhnika, Minsk, 1988).
14. J. H. M. Neijzed, H. M. J. Boots, F. A. M. A. Paulissen, *et al.*, Liq. Cryst. **22**, 255 (1997).
15. V. Twersky, J. Opt. Soc. Am. **52**, 145 (1962).
16. P. S. Drzaic, Mol. Cryst. Liq. Cryst. **261**, 383 (1995).
17. H. C. van de Hulst, *Light Scattering by Small Particles* (Wiley, New York, 1957; Inostrannaya Literatura, Moscow, 1961).
18. S. Zumer, Phys. Rev. A **37**, 4006 (1988).
19. A. N. Rakhmanov and V. I. Shmal'gauzen, Kvantovaya Élektron. **21**, 878 (1994).
20. K. S. Shifrin, *Introduction to the Optics of Ocean* (Gidrometeoizdat, Leningrad, 1983).

Translated by A. Chikishev

Technical Physics Letters, Vol. 26, No. 6, 2000, pp. 452–454. Translated from Pis'ma v Zhurnal Tekhnicheskoĭ Fiziki, Vol. 26, No. 11, 2000, pp. 10–17.

The Interaction between Capillary Waves near a Charged Liquid–Liquid Interface with a Tangential Discontinuity of the Velocity Field

S. O. Shiryaeva, O. A. Grigor'ev, and D. F. Belonozhko

Yaroslavl State University, Yaroslavl, 150000 Russia

Received January 10, 2000

Abstract—The evolution of capillary waves in a system of two liquid layers with a charged interface and the upper layer with a free surface and finite thickness translating at a constant velocity parallel to the semi-infinite lower layer is studied numerically within the framework of a linear mathematical model of capillary wave motion. The interacting waves generated at the free surface of the upper layer and at the interface give rise to an oscillatory instability of the interface, in addition to the Kelvin–Helmholtz instability. The new instability arises if the upper layer velocity is sufficiently small. The increment of oscillations depends on the density ratio of the liquids, velocity magnitude, and the charge at the interface. *© 2000 MAIK "Nauka/Interperiodica".*

This paper deals with the instability of a charged interface between two immiscible ideal liquids with differing densities, the upper liquid flowing with a constant velocity U parallel to the interface. The problem was extensively studied by experimenters and theorists inspired by various applications in geophysics, applied physics, and chemical engineering [1–6]. However, the research has been devoted to the case where each of the liquids occupies a half-space, and little is known about the instability development if the upper layer has finite thickness.

1. Consider the simplest case of ideal incompressible liquids in the gravitational field $\mathbf{g}$, the upper layer of a dielectric liquid having finite thickness h. Denote the densities of the upper and the lower layer as ρ_1 and ρ_2, respectively. Introduce the Cartesian coordinates such that the XOY-plane includes an unperturbed interface and the unit vector of the z-axis $\mathbf{n}_z$ is perpendicular to the interface and antiparallel to $\mathbf{g}$. Thus, the lower layer occupies the semi-infinite space $z < 0$. Let the interface possess an electric charge of density σ in the absence of perturbations from capillary flow.

In this system, the evolution of capillary waves can be determined upon finding the harmonic potentials ψ_1 and ψ_2 of the velocity field in the upper and the lower layer, respectively. The equations for ψ_1 and ψ_2 are

$$\Delta\psi_j = 0; \quad j = 1; 2; \tag{1}$$

the boundary conditions being

$z = h$

$$\frac{\partial\psi_1}{\partial z} \approx U\frac{\partial\zeta}{\partial x} + \frac{\partial\zeta}{\partial t};$$
$$\rho_1\frac{\partial\psi_1}{\partial t} + \rho_1 g\zeta + \frac{1}{2}\rho_1(\nabla\psi_1)^2 - \alpha_1\frac{\partial^2\zeta}{\partial x^2} = 0, \tag{2}$$

$z = 0$

$$\frac{\partial\psi_1}{\partial z} \approx U\frac{\partial\xi}{\partial x} + \frac{\partial\xi}{\partial t}; \quad \frac{\partial\psi_2}{\partial z} \approx \frac{\partial\xi}{\partial t};$$
$$\rho_1\left[\frac{\partial\psi_1}{\partial t} + g\xi + \frac{1}{2}(\nabla\psi_1)^2\right] \tag{3}$$
$$= \rho_2\left[\frac{\partial\psi_2}{\partial t} + g\xi\right] + \frac{4\pi}{\varepsilon}\sigma^2 k\xi - \alpha_2\frac{\partial^2\xi}{\partial x^2}.$$

Here, $\zeta(x, t)$ and $\xi(x, t)$ are the perturbations of the free surface (in the upper layer) and the interface, respectively, due to capillary waves; $\mathbf{U}$ is the constant velocity of the upper layer relative to the lower one; α_1 and α_2 are the surface-tension coefficients of the free surface and the interface, respectively; and ε is the permittivity of the upper layer [6]. The X-axis is conveniently directed along $\mathbf{U}$. It is reasonable to seek for ψ_1, ψ_2, $\zeta(x, t)$, and $\xi(x, t)$ in the form

$$\psi_1 = (A_1\exp(kz) + A_2\exp(-kz))\cos(kx - \omega t) + Ux;$$
$$\psi_2 = B\exp(kz)\cos(kx - \omega t); \tag{4}$$
$$\zeta = C\sin(kx - \omega t); \quad \xi = D\sin(kx - \omega t).$$

1063-7850/00/2606-0452$20.00 © 2000 MAIK "Nauka/Interperiodica"

Following [6], let us write expressions for the time dependence of the capillary wave amplitudes for the free surface and the interface in the context of (1)–(4):

$$\zeta = \zeta_0 \mathrm{Re}\exp\{it[kU + (Hkg + H\alpha_1\rho_1^{-1}k^3)^{1/2}]\}, \quad (5)$$

$$\xi = \xi_0 \mathrm{Re}\exp\{[it - k\rho U \pm (G\rho(\omega_*^2 + \rho\rho_2\rho_1^{-1}k^2U^2))^{1/2}]\}, \quad (6)$$

where

$$\omega_*^2 \equiv \rho_1^{-1}[gk(\rho_2 - \rho_1) + \alpha_2 k^3 - 4\pi\varepsilon^{-1}\sigma k^2] = 0,$$

$$\rho \equiv \frac{\rho_1}{G\rho_2 - \rho_1}, \quad G = \frac{A_1 - A_2}{A_1 + A_2},$$

$$H = \frac{A_1\exp(kh) - A_2\exp(-kh)}{A_1\exp(kh) + A_2\exp(-kh)},$$

ζ_0 and ξ_0 being the initial values of the capillary wave amplitudes.

Consider the case where the upper layer is so thin that the velocity field of the capillary flow in this layer depends on h very slightly. Then we can assume that G and H are equal in magnitude but differ in sign. [At any boundary, the signs of G and H characterize the contributions of the terms with $\exp(kz)$ and $\exp(-kz)$ to ψ_1, respectively.] Let us consider the interaction between waves generated at the free surface and the interface. Being linear with respect to small perturbations ζ and ξ, the model implies the wave interaction to be resonant, so that the wave frequencies are the same. From this fact, we easily arrive at a quadratic equation for H:

$$H^2 - H[kU^2(g + \alpha_1\rho_1^{-1}k^2)^{-1} - 2\rho_1\rho_2^{-1}] + \rho_1\rho_2^{-1} = 0. \quad (7)$$

An analysis of equation (7) indicates that the parameter space has several regions where both of the roots are positive. In particular, the roots are positive and differ in magnitude materially if the coefficient of H is much larger than the free term. Each of the roots H_j is associated with two stable and two unstable waves, as follows from (5) and (6) with $G = -H$. The waves corresponding to various H_j can easily be differentiated from each other, since the corresponding instability increments are approximately proportional to $H_j^{1/2}$ and have different orders of magnitude. Thus, there may be several regions of instability in the parameter space if the upper layer is sufficiently thin. To be specific, let us look at the dispersion relation of the problem.

2. With dimensionless quantities, substituting (7) into (2)–(6) at $\rho_2 = \alpha_2 = g = 1$ yields the dispersion relation

$$[1 + \rho_1\tanh(kh)]\omega^4 - 2Uk[2\rho_1\tanh(kh) + 1]\omega^3 + \left[\rho_1\tanh(kh)\left[6(Uk)^2 - \frac{k}{\rho_1}\left(1 + \frac{\alpha k^2}{\rho_1}\right)\right] + k[1 + k^2 + \alpha k^2 - Wk] - (Uk)^2\right]\omega^2 - 2k^2U[2\rho_1 kU^2\tanh(kh) - (1 + k^2 + \alpha k^2 - Wk)]\omega - k^2\left[\rho_1\tanh(kh) \times \left[1 + \frac{\alpha k}{\rho_1} + U^4k^2 + \left(\frac{\alpha k}{\rho_1} + 1\right)(1 - k^2) + Wk\right] + U^2k[1 + k^2 - Wk - \rho_1]\right] = 0; \quad (8)$$

$$W \equiv 4\pi\sigma^2\varepsilon^{-1}.$$

The figure numerically computed from (8) illustrates the pattern of instability development as affected by the thickness of the upper layer. The real part of ω determines the frequency of the capillary wave, whereas the imaginary part represents the instability increment (if $\mathrm{Im}\,\omega > 0$) or the damping constant (if $\mathrm{Im}\,\omega < 0$).

In panel (a), branches *1–3* refer to the capillary wave motions from the interface, whereas branches *4* and *5* refer to those from the free surface. It is seen that the two wave types do not interact with each other. Also note that branches *4* and *5* are parallel straight lines whose angle with the *U*-axis is dictated by the Doppler effect. Obviously, branch *4* corresponds to a wave directed as **U**, whereas branch *5* represents a similar wave traveling in the opposite direction.

Panel (b) is computed for the upper layer thickness h reduced to about 1. Here, the interaction between branches *1–3* and *4–5* results in the appearance of new components *6–10*, whereas branches *1*, *2*, and *4* change their shape. Branches *4*, *6*, *7*, and *9* represent nondecaying waves, whereas branches *8* and *10* contain both periodic exponentially decaying components ($\mathrm{Im}\,\omega < 0$) and exponentially growing periodic waves ($\mathrm{Im}\,\omega > 0$), the latter implying instability. The unstable branch *10* corresponds to the classical Kelvin–Helmholtz instability. Here, the critical velocity U_* of the instability onset goes up as h goes down, as illustrated by panels (a–c) in the figure. In branch *8*, the instability results from the interaction between the capillary waves generated at the free surface and the interface. The computation shows that the instability branches *8* and *10* move in opposite directions as h decreases, branch *8* shifting toward smaller values of *U*. The effect becomes more pronounced with decreasing ρ_1, as seen from panels (b) and (c).

3. The conclusions of this study are as follows. There exists the interaction between the capillary

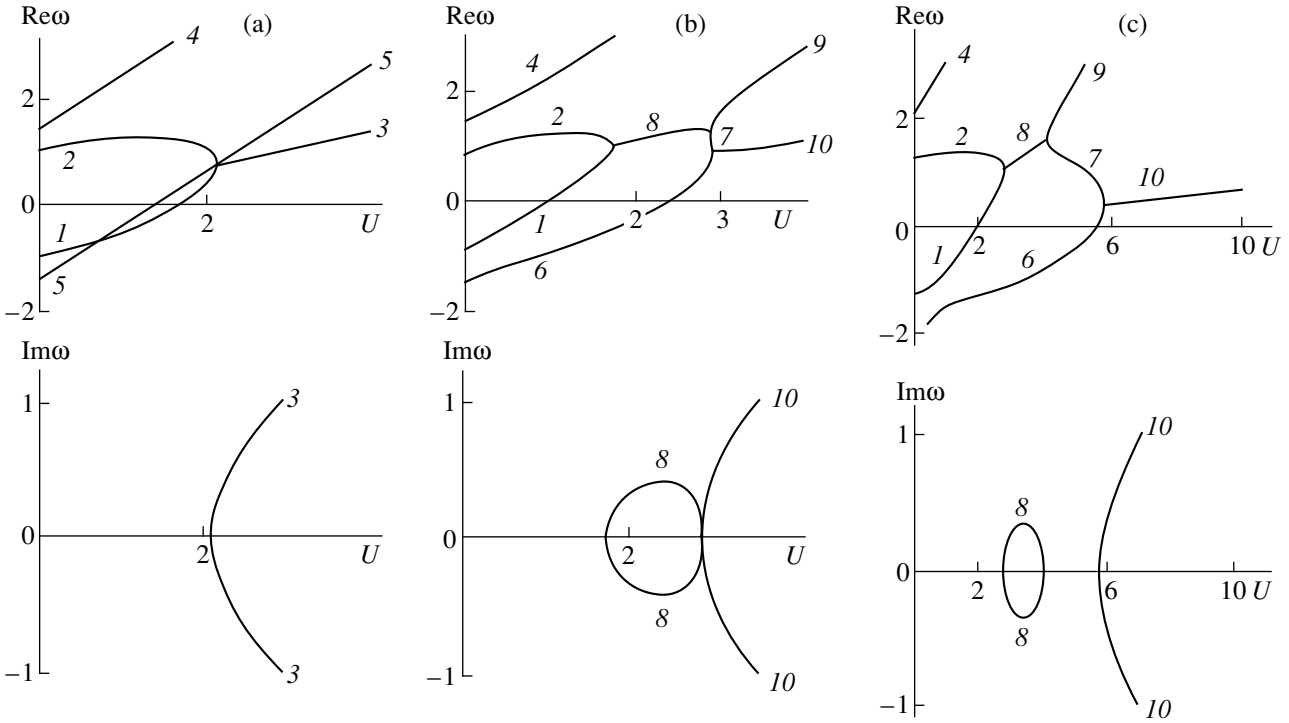

Fig. 1. Instability development illustrated by the plots of the complex frequency components $\mathrm{Re}\,\omega = \mathrm{Re}\,\omega(U)$ and $\mathrm{Im}\,\omega = \mathrm{Im}\,\omega(U)$ vs. the upper layer velocity U at $k = 1$, $\alpha_1 = 0.5$, and $W = 0$ for (a) $h = 5$ and $\rho_1 = 0.5$, (b) $h = 0.9$ and $\rho_1 = 0.5$, or (c) $h = 0.9$ and $\rho_1 = 0.1$.

waves generated at the free surface and the interface, if the upper layer thickness is less than the capillary constant of the lower liquid. The interaction leads to the previously unknown oscillatory instability, the instability threshold lowers with the thickness of the upper layer, although the increment falls as well. The effect is more pronounced if the interface has an uncompensated electric charge.

REFERENCES

1. R. D. Sydora, J. S. Wagner, J. S. Lee, *et al.*, Phys. Fluids **26**, 2986 (1983).
2. A. D. Sneyd, J. Fluid Mech. **156**, 223 (1985).
3. V. M. Kuznetsov and P. M. Lushnikov, Zh. Éksp. Teor. Fiz. **108**, 614 (1995) [JETP **81**, 332 (1995)].
4. O. A. Grigor'ev and S. O. Shiryaeva, Zh. Tekh. Fiz. **66** (2), 23 (1996) [Tech. Phys. **41**, 124 (1996)].
5. A. I. Grigor'ev, V. A. Koromyslov, and S. O. Shiryaeva, Zh. Tekh. Fiz. **69** (5), 7 (1999) [Tech. Phys. **44**, 486 (1999)].
6. A. I. Grigor'ev, Zh. Tekh. Fiz. **70** (1), 24 (2000) [Tech. Phys. **45**, 22 (2000)].

Translated by A. Sharshakov

Technical Physics Letters, Vol. 26, No. 6, 2000, pp. 455–457. Translated from Pis'ma v Zhurnal Tekhnicheskoĭ Fiziki, Vol. 26, No. 11, 2000, pp. 18–22.

On Mechanisms of Defect Formation in Aluminum Crystals Bombarded by Low-Energy Heavy Ions

G. V. Kornich[1], G. Betz[2], and A.I. Bazhin[3]

[1] *Zaporozhye State Technical University, Zaporozhye, 69063 Ukraine*
[2] *Institut für Allgemeine Physik, Technische Universität Wien, A-1040 Wien, Austria*
[3] *Donetsk State University, Donetsk, 340055 Ukraine*

Received January 17, 2000

Abstract—The mechanisms of formation of vacancies and radiation-induced adsorbed and interstitial atoms in the cascades of atomic collisions induced by 25-, 40- and 50-eV Ar and Xe ions normally incident onto the Al(100) surface at 300 K are discussed within the framework of the molecular dynamics approach. The numbers of bulk and surface vacancies formed in the course of a collision cascade exhibit two maxima in the case of Xe ions and a single maximum in the case of Ar ions. *© 2000 MAIK "Nauka/Interperiodica".*

The formation of surface and bulk vacancies and radiation-induced adsorbed (adatoms) and interstitial atoms in the atomic collision cascades induced by 25-, 40-, and 50-eV Ar and Xe ions normally incident onto the Al(100) surface has been simulated by the molecular dynamics methods [1].

A model aluminum crystal consisted of 4032 atoms arranged in 14 layers and had a lattice parameter of 4.05 Å. In the simulation, the periodic boundary conditions were imposed onto the side boundaries [1]. At high ion energies, a many-body atom–atom interaction potential was added to the ZBL potential suggested in [2]. The ion–atom interactions were also described by the ZBL potential. The temperature was modeled by setting a layer having a constant temperature at the side boundaries and on the crystal "bottom" [3]. Interstitial atoms and vacancies were generated by the algorithm suggested in [4]. The initial coordinates of ions incident onto a given region of the surface [5] were calculated by the law of random numbers. In each case, we made 200 calculations for the cascades taking place in the initial crystal, every cascade being followed over a time of 4 ps.

It was established that 40- and 50-eV Ar ions lose about 90% of their initial energy in the first and second atomic layers, whereas Xe ions, which penetrate deeper into the Al crystal, lose about 60% of the energy in the third and fourth layers. The reflection coefficient of Ar ions was equal to unity, whereas that for Xe ions decreased with an increase of the ion energy (0.96 for 25 eV, 0.73 for 40 eV, and 0.44 for 50 eV Xe ions). The simultaneous interactions of an ion with two or three recoil atoms and atoms from deeper layers of the crystal resulted in the change of the sign of the velocity component normal to the surface within the time intervals of 0.2–0.4 ps and 0.1–0.2 ps upon the cascade initiation for Xe and Ar ions, respectively. In this case, the ion reflection can be considered as completion of the "way clearing" for a heavy ion by light recoil atoms [6].

Figure 1 shows that Xe ions generate a larger number of stable adatoms than do Ar ions irrespective of their energies. For Xe ions, the maximum number of adatoms N_{ad} is attained somewhat later (within ~0.8–1.0 ps) than that for Ar ions (~0.2–0.6 ps). In the 0.2–0.4 ps time interval, the number of adatoms N_{ad} is determined by interactions between an impinging ion and the primary recoil atoms with the surface atoms, and, possibly, by the curvilinear atomic collision sequences emerging at the surface [7]. According to [8], the threshold energy for generating atomic displacement collision sequences along the ⟨110⟩ directions in Al crystals with the potential suggested in [2] equals 6 eV, and therefore the atomic displacement collision sequences along the ⟨110⟩ directions can arise even for an ion energy as low as 25 eV. These mechanisms are responsible for the formation of almost all the adatoms and, within the 0.2–0.4 ps time interval, are more effective for Ar than for Xe ions (because the Ar ions provide for the formation of primary recoil Al atoms with higher energies and with the velocity component in the (100) plane exceeding its normal component). The maximum mean square displacements of adatoms in the case of Ar ions (not discussed in detail here) are formed within the ~0.5–0.6 ps interval and, thus, confirm that the process of adatom formation by Ar ions is restricted to the collisional stage of the cascade.

In the case of Xe ions, the maximum value of N_{ad} is attained due to interactions of the surface atoms with a reflected ion and recoil atoms formed in the crystal bulk within the 0.8–1.0 ps time interval. This process is accompanied by an increase of the mean square displacement of both adatoms and atoms in the crystal bulk in the 0.5–1.0 ps time interval. The momentum can be transferred from the bulk to surface atoms within

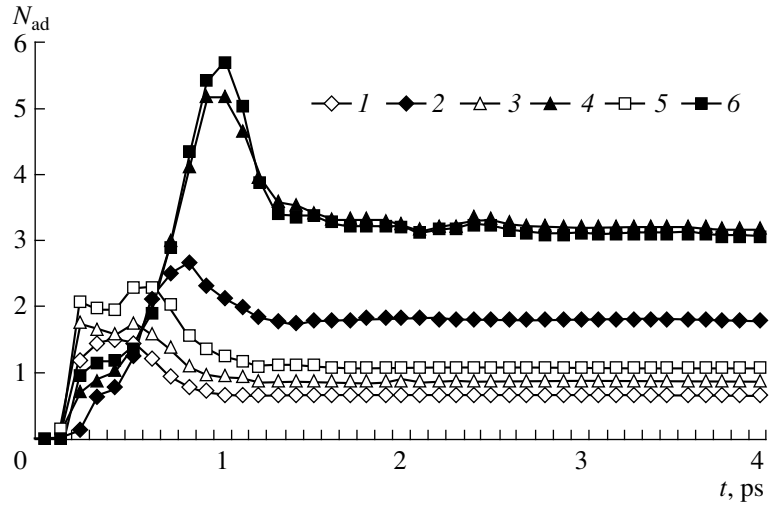

Fig. 1. Numbers of adatoms (N_{ad}) formed in a model Al crystal bombarded with (*1*) 25-, (*3*) 40-, or (*5*) 50-eV Ar ions and (*2*) 25-, (*4*) 40-, and (*6*) 50-eV Xe ions as functions of the cascade duration.

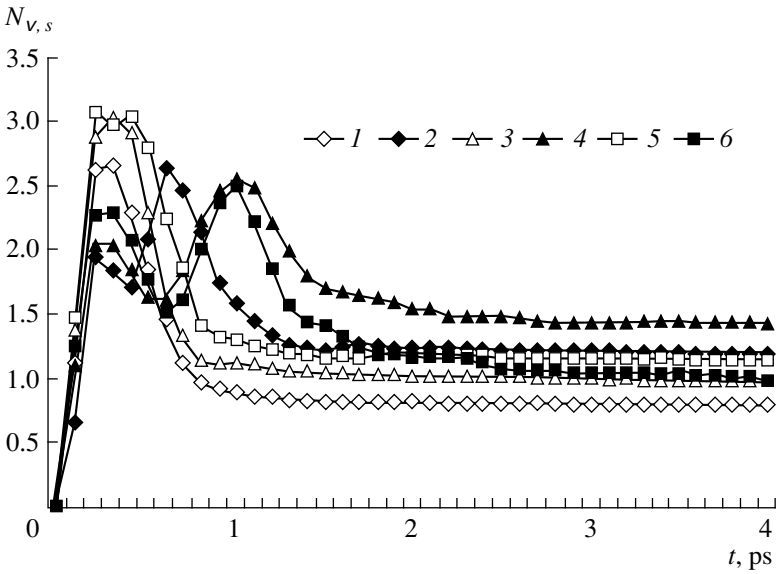

Fig. 2. Numbers of surface vacancies ($N_{v,s}$) formed during the model crystal bombardment with (*1*) 25-, (*3*) 40-, or (*5*) 50-eV Ar ions and (*2*) 25-, (*4*) 40-, or (*6*) 50-eV Xe ions as functions of the cascade duration.

two to three steps of the atomic displacement collision sequences within the 0.4–0.6 ps time interval. If an ion leaves the crystal, the probability of adatom formation is higher for Xe than for Ar ions, because the former ions leave the crystal with an average energy of 2.5–5.5 eV, whereas the latter ions leave it with an average energy ranging within 1.5–2.0 eV, depending on their initial energy. Also, almost no Ar ions can penetrate into the crystal depth; the Ar ions can be inside the crystal for only about 0.5 ps irrespective of their initial energy, whereas 40- and 50-eV Xe ions can occur in the crystal for about 1.2 ps and the 25-eV Xe ions, for about 0.7 ps, which is comparable with the time necessary for the formation of a maximum number of adatoms with maximum mean square displacements.

It is seen from Fig. 2, that, irrespective of the initial energy of Ar ions, the only maximum in the number of surface vacancies $N_{v,s}$ (vacancies in the first atomic layer) is attained within 0.2–0.3 ps. The time intervals of the Ar ion penetration into the crystal and its motion out of the crystal differ by less than 0.1 ps, which results in the overlap of the times characteristic of the operation of various mechanisms of the vacancy and adatom production and, thus, in the formation of a common resulting $N_{v,s}$ maximum. In the case of Xe ions, two $N_{v,s}$ maxima are formed, of which the first one arises within the same time interval as in the case of Ar ions. The time corresponding to the second $N_{v,s}$ maximum depends on the initial energy of ions. Usually, this maximum is formed by those Xe ions which penetrate

into small crystal depths (1–3 atomic layers) and, leaving the target, possess an energy sufficient for the formation of an adatom and a surface vacancy. Dependence of the number of bulk vacancies $N_{v,b}$ on the cascade duration is similar to the time dependence of $N_{v,s}$ irrespective of the bombardment conditions.

Data on the relocations of atoms show that the number N_{WS} of atoms leaving their Wigner–Seitz cells in the Xe-induced cascades attain two maxima, whereas in the Ar-induced cascades, there is only one such maximum. The times necessary to attain the maximum N_{WS} values coincide with the times of attaining the $N_{v,s}$ and $N_{v,b}$ maxima. Different numbers of the N_{WS} maxima and, accordingly, of the $N_{v,s}$ and $N_{v,b}$ maxima, for Ar and Xe ions are associated not only with different characteristic times of the forward and the reverse ion motion in the crystal, but also with the fact that the number of atomic relocations from the nth to the $(n-1)$th or $(n-2)$th layer during the motion of a reflected Ar ion in the crystal is much smaller than the number of such relocations for a Xe ion. For example, at the primary ion energy of 50 eV, the number of interlayer atomic relocations along the [100] direction within one cascade equals to about 3.2 for both Ar and Xe ions moving into the crystal bulk, whereas the numbers of reverse relocations (toward the surface) are 5.85 for Xe and only 1.8 for Ar ions.

In the case of Ar ions, a 2 ps-long cascade evolution leads to the formation of a slightly larger number of interstitial atoms than in the case of Xe ions, which is explained by a higher probability of development of an atomic displacement collision sequences along the ⟨110⟩ directions by Ar ions at the collisional stage of the cascade. Another possible mechanism for the formation of interstitials in an Al crystal may consist in the relocation of atoms into the crystal for a depth of 1.5–2.0 lattice constants [9, 10]. For 50-eV Ar and Xe ions, there are about 0.35 of such migrations per cascade. The time of formation of the resulting maximum number of interstitials N_{in} (0.2–0.3 ps) is independent of the incident ion type and energy and corresponds to the collisional stage of the cascade development.

The simulations performed for Cu and Ni crystals under the same bombardment conditions with the use of the potentials suggested in [11] and [2], respectively, showed that, usually, only one $N_{v,s}$ maximum and one or two N_{ad} maxima can be formed within one cascade.

REFERENCES

1. M. J. Haile, *Molecular Dynamics Simulation: Elementary Methods* (Wiley Interscience, New York, 1992).
2. F. Gao, D. J. Bacon, and G. J. Ackland, Philos. Mag. A **67**, 275 (1993).
3. H. J. Berendsen, J. P. M. Postma, W. F. van Gunsteren, *et al.*, J. Chem. Phys. **81**, 3684 (1984).
4. F. Karetta and H. M. Urbassek, J. Appl. Phys. **71**, 5410 (1992).
5. G. Betz, M. J. Pellin, J. W. Burnett, and D. M. Gruen, Nucl. Instrum. Methods Phys. Res. B **58**, 429 (1991).
6. V. I. Shulga, M. Vicanek, and P. Sigmund, Phys. Rev. A **39**, 3360 (1989).
7. A. M. Mazzone, Philos. Mag. Lett. **70**, 93 (1994).
8. D. J. Bacon, H. F. Deng, and F. Gao, J. Nucl. Mater. **205**, 84 (1993).
9. S. Valkealahti and R. M. Nieminen, Nucl. Instrum. Methods Phys. Res. B **18**, 356 (1987).
10. G. V. Kornich and G. Betz, Nucl. Instrum. Methods Phys. Res. B **143**, 455 (1998).
11. H. Gades and H. M. Urbassek, Nucl. Instrum. Methods Phys. Res. B **69**, 232 (1992).

Translated by L. Man

Technical Physics Letters, Vol. 26, No. 6, 2000, pp. 458–460. Translated from Pis'ma v Zhurnal Tekhnicheskoĭ Fiziki, Vol. 26, No. 11, 2000, pp. 23–28.

Half-lives of Atomic Tritium and Free Triton Determined from the Chemical Shift of the Beta Decay Time Constant

Yu. A. Akulov and B. A. Mamyrin

Ioffe Physicotechnical Institute, Russian Academy of Sciences, St. Petersburg, 194021 Russia

Received January 22, 2000

Abstract—Data on the chemical shift of the beta decay time constant were used to determine the experimentally justified half-lives of atomic tritium $(t_{1/2})_a$ = 12.264 ± 0.018 year and free triton $(t_{1/2})_t$ = 12.238 ± 0.020 year. © *2000 MAIK "Nauka/Interperiodica".*

The beta decay of tritium represents a superallowed transition of the $1/2^+ \longrightarrow 1/2^+$ type between terms of the isospin doublet:

$$^3_1\mathrm{H} \longrightarrow {}^3_2\mathrm{He} + e^- + \tilde{\nu} + 18.6\ \mathrm{keV}.$$

A theoretical analysis of this process in the particular case of a comparatively simple three-nucleon problem allows us to study various models of intranuclear interactions. In order to verify adequacy of the existing notions about the structure of nuclear wavefunctions, the shape of the intranuclear potential, and the role of the internucleon meson exchange in the beta decay, it is necessary to know exact values of the main characteristics of this transition, including the half-life of the free triton (tritium nucleus).

The excess mass of the second neutron in the tritium nucleus being very close to the Coulomb energy of the second proton in the helium nucleus makes the two isospin states almost completely degenerate. Small value of the liberated energy makes the beta spectrum highly sensitive with respect to the structure of the electron phase space accessible for the beta-electron (β-electron) appearing in the vicinity of the beta-active nucleus. The electron environment of a triton affects the beta decay rate, these changes exceeding in magnitude the half-life variations related to differences in the accepted models of intranuclear interactions. As a result, the experimental values of the beta decay half-life $t_{1/2}$ (or the decay time constant $\lambda = \ln 2/t_{1/2}$), corresponding to the decay of a triton entering into certain atomic-molecular system, can be used in theoretical calculations only provided that changes (chemical shifts) of the decay time constant related to the effect of electron environment upon the beta process in the triton can be measured or calculated with sufficient precision for the given atomic-molecular system.

In considering the process of β-electron formation in the phase space of tritium-containing atomic-molecular systems, it is a common practice to take into account three possible reaction channels: (1) direct formation of electrons with a continuous spectrum; (2) electrons with a continuous spectrum formed at the expense of orbital electrons replaced by β-electrons; (3) decay into bound states, whereby β-electrons are formed in the shells of daughter atoms. Although the existing theory developed in [1, 2] is capable, in principle, of determining the probabilities of decay into bound states for an arbitrary electron environment of a triton, the values calculated by various researchers show satisfactory agreement only for the simplest atomic systems such as triton (T^+) and tritium (T). The ratio of probabilities for the decay into bound state and continuum calculated for T^+ in [3–5] are 1.10, 1.03, and 1.08%, respectively ($\Delta\lambda_{bt}/\lambda = 1.07 \pm 0.04\%$). A relative increase in the decay rate, caused by the decay into bound states, calculated for the T atom in [1–3, 5] is 0.56, 0.69, 0.66, and 0.55%, respectively ($\Delta\lambda_{ba}/\lambda = 0.62 \pm 0.07\%$). The interaction between a β-electron and an orbital electron in the final state leads to the transfer of the orbital electron to a state in continuum, while the β-electron may either stay in the bound state in the resulting helium atom or occur in an *s*-state of the continuous spectrum as well. This electron interaction must produce an $\Delta\lambda_{ch}/\lambda \approx 0.15\%$ increase the relative decay rate of triton in the T atom [5, 6]. In tritium-containing systems, where the phase volume accessible for the beta-electron in the vicinity of triton is deformed by molecular orbitals, the calculation of exchange corrections to the beta decay probabilities may have only a qualitative character.

For the direct formation of electrons with a continuous spectrum as a result of the beta decay in the Coulomb field of the nucleus, the effect of electron environment on the magnitude of the phase-space factor (*f*) is described by introducing a parameter of screening of the nucleus charge by orbital electrons and a parameter of decrease in the observed upper boundary energy caused by the excitation of atomic electrons as a result of their interaction with the β-electron in the final state [7]. In recent years, a considerable effort of researchers in solving the task of evaluating the mass of neutrino has

1063-7850/00/2606-0458$20.00 © 2000 MAIK "Nauka/Interperiodica"

stimulated theoretical investigations of the atomic effects taking place in the high-energy part of the beta spectrum of some tritium-containing atomic-molecular systems such as T, T^-, T_2, CH_3T, etc. [4, 5, 9, 10]. In the case of decay in the ground state of a tritium atom, about 70% of the electron transitions are to the 1*s* state of $^3He^+$ ion, ~25% of the transitions—to the 2*s* state, ~1.3%—to the 3*s* state, and so on [6, 8]. As a result, the decay rate of triton in the tritium atom increases by $\Delta\lambda_{ex}/\lambda \approx 0.50\%$ [4, 5] as compared to the value for the free triton. The effect of electron screening, producing perturbation in the low-energy part of the beta spectrum, was theoretically studied in detail only for the decay of triton in the T atom and the T^- ion [5] where the screening potential is formed by simple electron configurations, such as ns^1 in the $^3He^+$ ion and $1s^2$, $2s^2$, or ns^1ms^1 in the neutral He atom. In the case of T atom, the screening decreases the decay time constant by $\Delta\lambda_s/\lambda \approx = 0.41\%$ as compared to the value for the free triton.

Thus, a complete set of theoretical corrections for the decay half-life, taking into account four possible atomic effects accompanying the beta process (decay into bound states, exchange effect, screening of the nuclear charge by orbital electrons, and excitation of the orbital electrons) is available only for the free triton and free tritium atom. This implies that the absolute value of the decay half-life for the free triton can be calculated only using the absolute value of this parameter for the tritium atom, which has to be determined in experiment. Direct measurement of the decay half-life for the atomic tritium requires solving a very complicated task of stabilizing free hydrogen atoms over a period of time comparable with their half-life (the same circumstance hinders the experimental determination of decay half- lives of the T^+ and T^- ions).

An alternative approach to solving the task of experimental determination of the time characteristics of beta decay in unstable atomic-molecular systems consists in performing special experiments on measuring a difference in the decay rates of tritium in two compounds, one of which can be characterized by the absolute value of the decay time constant. Previously [11], we have suggested a method for determining a difference between the decay time constants of tritium by comparing the growth rates of the relative content of radiogenic helium-3 and the base helium-4 in these compounds. This method was used to measure a difference between the beta decay time constants of the atomic and molecular tritium. According to the experimental scheme, two identical samples of a gas mixture, containing helium-4 and molecular tritium, were prepared and then one sample was modified so as to convert tritium into the atomic state. Thermalized free tritium atoms were obtained by the mechanism of resonance dissociation, whereby T_2 molecules gained the energy necessary to break the interatomic bond from the second-order impact upon collisions with mercury atoms excited in an RF discharge. The discharge, initiated by an electric field with a strength of ~100 V/cm at a frequency of 1 MHz, was maintained for a time period of 171 min during which 2×10^{13} helium-3 atoms are formed in the gas mixtures. The possible leaks of tritium and helium atoms from the ampules were detected by proportional counters (sensitivity, ~10^6 T atoms) and an isotope mass spectrometer (sensitivity, ~3×10^4 helium atoms). Five series of measurements of the helium isotope ratios were performed by sequentially admitting the gas mixtures with molecular and atomic tritium into a mass spectrometer chamber. The relative difference of the beta decay time constant for the molecular and atomic tritium determined from these data is $(\lambda_a - \lambda_m)/\lambda_m = 0.00257 \pm 0.00045$ [12]. The indicated uncertainty corresponds to a single standard deviation and is related primarily to the scatter of helium isotope ratios from series to series.

Using the above result, we can determine the absolute value of the half-life of atomic tritium, since the half-life of molecular tritium was measured in direct experiments. We have taken a weighted average of the two most recently published (and well mutually consistent) molecular tritium half-lives determined using the helium isotope method [13] and the decay curve plotted by measuring the bremsstrahlung radiation of β-electrons [14]: $\langle(t_{1/2})_m\rangle = 12.296 \pm 0.017$ year. Taking into account that $\Delta t_{1/2}/t_{1/2} = -\Delta\lambda/\lambda$ for $\Delta\lambda/\lambda \ll 1$, we obtain $(\Delta t_{1/2})_{ma} = (t_{1/2})_m - (t_{1/2})_a = 0.0316 \pm 0.0055$ year. Therefore, the absolute value of the half- life of atomic tritium is $(t_{1/2})_a = 12.264 \pm 0.018$ year with an error determined almost completely by the uncertainty of $\langle(t_{1/2})_m\rangle$. Since the $\langle(t_{1/2})_m\rangle$ and $(\Delta t_{1/2})_{ma}$ values were determined by the experimental methods taking into account all the possible beta decay reaction channels, the $(t_{1/2})_a$ value determined as described above corresponds to the total probability of decay in the atomic tritium (including both the processes leading to the continuous electron spectrum and the decay into bound states). Therefore, in using this $(t_{1/2})_a$ value to estimate the half-life of triton $(t_{1/2})_t$, we have to take into account all four corrections mentioned above for atomic effects in the free tritium. Taking into account that each of these atomic corrections is much less than unity, the half-life of the free triton can be determined from the following relationship:

$$(t_{1/2})_a\left(1 + \frac{\Delta\lambda_{ba} + \Delta\lambda_{ch} + \Delta\lambda_{ex} - \Delta\lambda_s}{\lambda}\right) = (t_{1/2})_t\left(1 + \frac{\Delta\lambda_{bt}}{\lambda}\right),$$

where the second term in parentheses in the right-hand part of this equation reflects a change in the $(t_{1/2})_t$ value due to decay into the bound states of $^3He^+$ ion–the only possible atomic effect in the decay of the free triton. Using the above theoretical atomic corrections and the

experimental value of $(t_{1/2})_a$, we obtain the half-life of the free triton $(t_{1/2})_t = 12.238 \pm 0.020$ year. This half-life characterizes, for example, a decrease in the concentration of tritium nuclei as a result of beta decay in a fully ionized hydrogen plasma.

In the case when only the Coulomb field of the nucleus has to be taken into account (that is, when the phase-space factor is calculated using the standard Fermi energy and the decay into bound states is ignored), the half-life of triton is $(t_{1/2})_{tc} = 12.396 \pm 0.020$ year. This value should be employed, in particular, for determining the beta decay energy deposition in a tritiated plasma, where the energy liberated upon decay into bound states is almost entirely carried away by antineutrinos. The $(t_{1/2})_{tc}$ value must be also used in calculating the reduced half-life of triton $ft_{1/2}$ when the upper energy boundary of the integration interval in the phase space is taken equal to the difference of nuclear masses of tritium and helium-3 (i.e., a difference in the binding energies of the orbital electrons in the initial and final atomic-molecular systems is neglected). Once the exact $ft_{1/2}$ value for triton is available, we may also obtain independent estimates of some fundamental quantities, such as the ratio of the Fermi and Gamov–Teller coupling constants in the weak interactions and the lifetime of the free neutron.

This work was supported by the Russian foundation for Basic Research (project no. 97-03-33665) and the State Scientific-Technological Program “Fundamental Metrology” (project no. 4.06.)

REFERENCES

1. P. M. Sherk, Phys. Rev. **75**, 789 (1949).
2. J. N. Bahcall, Phys. Rev. **124**, 495 (1961).
3. V. N. Tikhonov and F. E. Chukreev, Vopr. At. Nauki Tekh., Ser. At. Mater. **1** (4), 12 (1980).
4. B. Budick, Phys. Rev. Lett. **51**, 1034 (1983).
5. M. R. Harston and N. C. Pyper, Phys. Rev. A **48**, 268 (1993).
6. W. S. Haxton, Phys. Rev. Lett. **55**, 807 (1985).
7. K.-E. Bergkvist, Phys. Scr. **4**, 23 (1971).
8. R. D. Williams and S. E. Koonin, Phys. Rev. C **27**, 1815 (1983).
9. P. Froelich, B. Jeziorski, W. Kolos, *et al.*, Phys. Rev. Lett. **71**, 2871 (1993).
10. I. G. Kaplan, G. V. Smelov, and V. N. Smutny, Phys. Lett. B **161**, 389 (1985).
11. Yu. A. Akulov, B. A. Mamyrin, and P. M. Shikhaliev, Pis’ma Zh. Tekh. Fiz. **19** (18), 72 (1993) [Tech. Phys. Lett. **19**, 594 (1993)].
12. Yu. A. Akulov and B. A. Mamyrin, Pis’ma Zh. Éksp. Teor. Fiz. **68**, 167 (1998) [JETP Lett. **68**, 175 (1998)].
13. Yu. A. Akulov, B. A. Mamyrin, and L. V. Khabarin, Pis’ma Zh. Tekh. Fiz. **14**, 940 (1988) [Sov. Tech. Phys. Lett. **14**, 416 (1988)].
14. B. Budick, Jianshen Chen, and Hong Lin, Phys. Rev. Lett. **67**, 2630 (1991).

Translated by P. Pozdeev

Technical Physics Letters, Vol. 26, No. 6, 2000, pp. 461–463. Translated from Pis'ma v Zhurnal Tekhnicheskoĭ Fiziki, Vol. 26, No. 11, 2000, pp. 29–35.

Structural Changes of the Friction Surface and Wear Resistance of a ZrO_2–Y_2O_3 Ceramic

N. L. Savchenko, P. V. Korolev, S. Yu. Tarasov, and S. N. Kul'kov

Institute of Strength Physics and Materials Sciences, Siberian Division, Russian Academy of Sciences, Tomsk, 634055 Russia

Received January 10, 1999

Abstract—Quantitative parameters of the surface structures and the wear resistance of a ZrO_2–Y_2O_3 ceramic tested by friction on a steal disk have been determined. It is shown that the friction contact gives rise to quasiperiodic cracks on the friction surface of the ceramic and leads to the formation of a transfer layer. It is established that the wear intensity correlates with the intercrack spacing along the sliding direction and the amount of the steel counterbody elements on the ceramic surface. © *2000 MAIK "Nauka/Interperiodica".*

The viscous phase-transformation-hardened ZrO_2–Y_2O_3 ceramics are promising materials for various tribotechnical applications [1]. A special feature of this ceramic is the possibility to modify its structure, phase composition, and mechanical properties over a wide range and to influence the acting hardening (strengthening) mechanism by changing the chemical composition, sintering mode, and thermal treatment [1, 2].

It is well known that the friction occurring in metal–ceramic couples can give rise to the systems of cracks on the ceramic surface [3–7]. In particular, it was found [5, 6] that high-speed friction (4–10 m/s) between a ZrO_2–Y_2O_3 ceramic and a steel counterbody results in the formation of quasiperiodic cracks on the ceramic surface dividing it into band fragments. Another important feature of the friction and wear in such couples is the transfer of a metal onto the ceramic surface with the formation of the so-called transfer layer [3–7], whose role in the surface structure formation and the wear resistance of the ceramic is not completely understood as yet. Quantitative information on the characteristics of the transfer layer and their correlation with the parameters of the crack structure and the wear intensity would elucidate the wear mechanisms operative in ceramic materials under the conditions of high-speed friction on steel.

Our study was aimed at establishing a relationship between the characteristics of the transfer layer formed on the ceramic surface, the parameters of quasiperiodic cracks formed on this surface, and the wear intensity of ZrO_2-based ceramic during its high-speed sliding over a steel surface.

We studied the specimens of a ceramic having the composition 97 mol % ZrO_2 + 3 mol % Y_2O_3 prepared by two methods–three-hour sintering in vacuum at 1750°C and five-hour sintering in air at 1600°C. These methods, chosen in accordance with the recommendations given in [2], were dictated by the necessity of studying the surface structures and the wear resistance of materials with markedly different grain size and hardening mechanisms. The material obtained by sintering in air consisted of 0.8-μm grains, in which the hardening occurred mainly by the phase-transformation-induced mechanism. The other material, obtained by sintering in vacuum, consisted of 4-μm grains, in which the hardening occurred by the phase transformation mechanism combined with some other hardening mechanisms. The physical and mechanical properties of the ceramics of both types and the specific features of the hardening mechanisms operative in these materials were considered elsewhere [2].

The friction tests were performed by the pin-on-disk scheme. The counterbody was a disk fabricated from a cast high-speed steel. The sliding velocity ranged within 4–10 m/s, the pressure varied from 1 to 10 MPa. Both pressure and sliding velocity were selected by analogy with other similar tests providing for the formation of a system of cracks on the ceramic surface dividing it into band fragments [5]. The friction path was 1000 m irrespective of the test regime. The wear intensity was measured by the loss in the material volume related to the friction path.

The microstructure of the ceramic samples was studied prior to and upon the friction tests on a Neophot 21 optical microscope and a JEOL JSM-84 scanning electron microscope equipped with a special Link-860 attachment for the electron microprobe analysis.

Figure 1 shows a typical friction surface with quasiperiodic cracks. Upon measuring the intercrack spacings along the sliding direction, we determined and analyzed their distribution. It was established that the shapes of such distributions were close to that of a normal distribution with pronounced maximum. The average intercrack spacing changed depending on the friction regime.

1063-7850/00/2606-0461$20.00

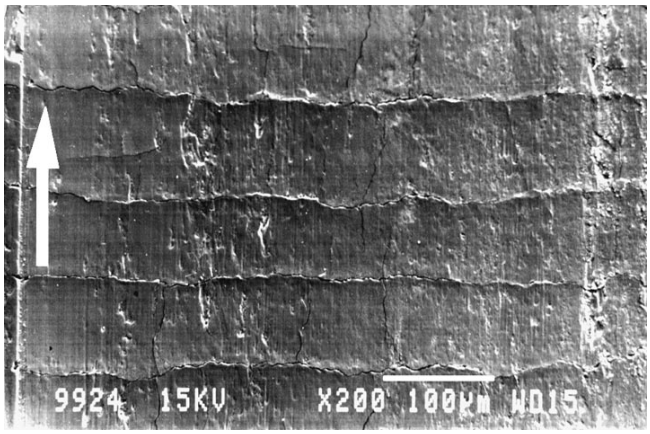

Fig. 1. Typical cracks on the friction surface of a ceramic. The arrow indicates the sliding direction.

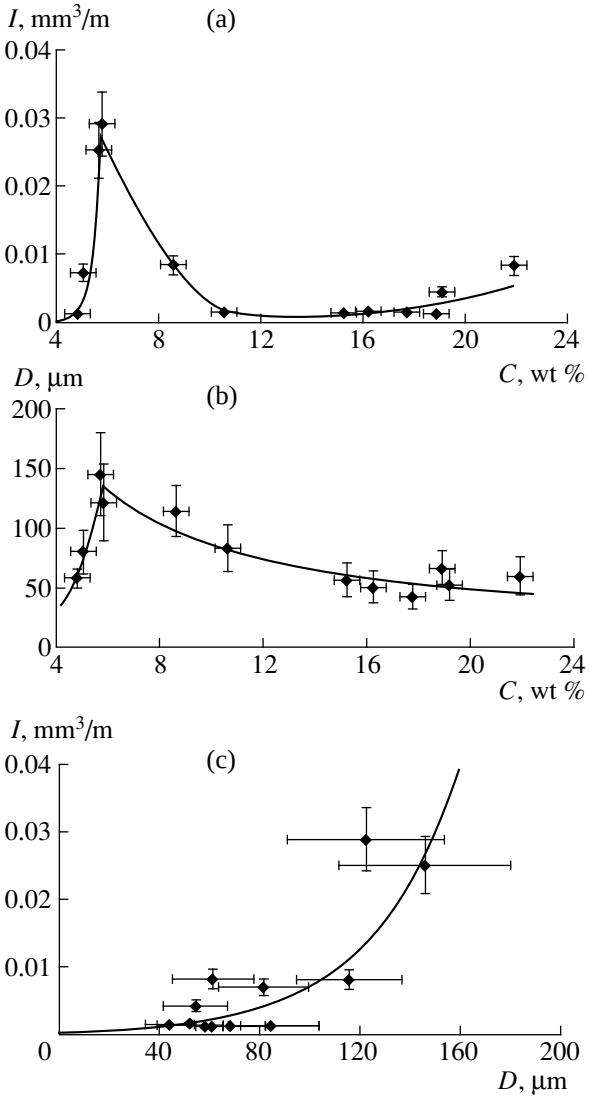

Fig. 2. The plots of (a) wear intensity and (b) the intercrack spacing along the sliding direction versus the concentration of the elements transferred from the steel disk onto the ceramic surface, and (c) the wear intensity versus the intercrack spacing along the sliding direction.

The electron microprobe analysis showed that the friction surface of all the specimens contained the chemical elements transferred from the steel counterbody (Fe, V, Cr, Mn, W, and Mo), the concentrations of which depended on the friction regime. The metallography and electron microscopy studies showed that if the concentrations of elements from the steel disk on the ceramic surface was low, the transfer layer was nonuniformly distributed over the surface–large regions of the ceramic surface contained no transfer layer at all. At high concentrations of these elements, the transfer layer uniformly coated the whole friction surface of the ceramic.

Figures 2a and 2b show the plots of the wear intensity I and the average intercrack spacing D along the sliding direction as functions of the concentration C of the elements from the steel counterbody on the ceramic surface. To within the measurement error, the experimental data for both studied materials were described by the same relationships, which allowed the obtained results to be analyzed irrespective of the initial structure of the ceramic and the friction parameters. As is seen from Fig. 2a, the function $I(C)$ is nonmonotonic. First, with an increase in C, the wear intensity also increases. Then, at $C > 6\%$, the growth changes to decrease and finally, at $C > 17\%$, the wear intensity slightly increases again. A similar behavior, especially in the concentration range from 0 to 17%, is also characteristic of the $D(C)$ function. The similar shapes of the $I(C)$ and $D(C)$ curves suggests a direct relationship between the I and D values. Indeed, the data presented in Fig. 2c confirm the presence of such a correlation: an increase in D results in the corresponding increase in I. This indicates that the volume of the material removed from the ceramic surface is determined by the characteristic spacing in the crack system.

One can assume that the above correlations are caused by the following. The increase in D and I at a concentration C ranging within 0–6% corresponds to a situation where the dominating process is the transfer of the ceramic material onto the steel counterbody. It is highly probable that this process is favored by a relatively low temperature (below the melting point of the steel) in the contact zone and a relatively high viscosity of the transfer layer, which facilitates the "adhesion detachment" of the ceramic fragments separated by the cracks. The maximum at $C = 6\%$ in Figs. 2a and 2b corresponds to a regime providing the strongest adhesion seizure because of a high diffusion activity of the transfer layer. This process is accompanied by the development of considerable contact stresses, cracking-induced separation of the fragments, and subsequent delamination, and detachment of large ceramic fragments. The temperatures attained in the zone of the friction contact were estimated by a method analogous to the calculations of Lim and Ashby [8]. These estimates show that the concentrations C ranging from 0 to 6% correspond to the temperatures ranging from 700 to 1000°C, i.e., the temperatures lower that the melting

point of steel, whereas at $C > 6\%$, the temperature increases and, finally, reaches a level of 2000°C. Apparently, the formation of maxima on the $I(C)$ and $D(C)$ curves (Fig. 2a, b) corresponds to the transition of the solid transfer layer into a quasiliquid state.

A decrease of both D and I with an increase in the concentration observed for $C > 6\%$ corresponds to a situation where the transfer of the material from the steel counterbody onto the ceramic surface is prevailing. The material transfer is favored by high temperatures (which can be as high as the melting point of steel) developed in the zone of the tribological contact. As a result, a quasiliquid film is formed on the ceramic surface. A continuous transfer layer formed on the ceramic surface plays the role of a soft coating increasing the real sample–counterbody contact area and, thus, providing a lower level of contact stresses on the friction surface of the ceramic. As a result, the processes of stress relaxation in the surface layers of the ceramic are accompanied by the formation of a quasiperiodic structure of cracks separated by small spacings (which is seen from the moderate wear intensity). A slight increase in I at $C > 17\%$ seems to be associated with degradation of the mechanical properties of the subsurface layers of the ceramic. This degradation increases with the temperature in the tribological contact zone.

Thus, our studies proved a certain correlation between the quantitative parameters of the quasiperiodic structure of cracks, the concentration of chemical elements transferred from the steel counterbody to the ceramic surface, and wear resistance of the ceramic. Under the friction conditions studied, there are at least two factors that influence the intercrack spacing and the wear intensity. The first is the adhesion detachment of fragments of the ceramic at temperatures be low the melting point of the steel in the tribological contact zone. The second factor is a decrease of the level of contact stresses caused by the transition of the transfer layer into a quasiliquid state at temperatures in the tribological contact zone exceeding the melting point of the steel. In this case, the characteristic spacing in the crack system determines the volume of the material removed from the ceramic surface.

REFERENCES

1. L. Nettleship and R. Stevens, Int. J. High Technol. Ceram., No. 3, 1 (1987).
2. N. L. Savchenko, T. Yu. Sablina, and S. N. Kul'kov, Izv. Vyssh. Uchebn. Zaved. Fiz., No. 8, 89 (1994).
3. P. C. Becker, T. A. Libsch, and S. K. Rhee, Ceram. Eng. Sci. Proc., Nos. 7–8, 1040 (1985).
4. A. Ravikiran, V. S. Nagarajan, S. K. Biswas, *et al.*, J. Am. Ceram. Soc. **78**, 356 (1995).
5. S. N. Kul'kov, N. L. Savchenko, S. Yu. Tarasov, *et al.*, Trenie Iznos **18**, 798 (1997).
6. N. Savchenko, S. Tarassov, A. Melnikov, *et al.*, in *Proceedings of the European Conference on Composite Materials, Science, Technologies and Applications (ECCM-8), Naples, Italy, June 3–6, 1998* (Woodhead, Cambridge, 1998), Vol. 4, pp. 343–350.
7. A. Ravikiran and B. N. Pramila Bai, J. Mater. Sci. **30**, 1999 (1995).
8. S. C. Lim and M. F. Ashby, Acta Metall. **35**, 1 (1987).

Translated by L. Man

Technical Physics Letters, Vol. 26, No. 6, 2000, pp. 464–466. Translated from Pis'ma v Zhurnal Tekhnicheskoĭ Fiziki, Vol. 26, No. 11, 2000, pp. 36–40.

Annealing of the Radiation-Induced Defects in Natural Diamond

V. N. Amosov, A. V. Krasil'nikov, S. N. Tugarinov, V. V. Frunze, and A. Yu. Tsutskikh

Troitsk Institute of Innovation and Thermonuclear Investigations (TRINITI), Troitsk, Moscow oblast, 142092 Russia

Received January 10, 2000

Abstract—Radiation-induced defects in a natural type IIa diamond were studied by analysis of the electronic absorption spectra in the visible range measured upon annealing of the pre-irradiated samples for various times at 550°C. Equations describing the growth and decay of intensity for the absorption peaks of seven defects are presented. © *2000 MAIK "Nauka/Interperiodica".*

We have studied the formation of neutron-irradiation-induced defects and their behavior during subsequent vacuum annealing in a natural type IIa diamond–a wide-bandgap photoconductor with a small concentration of nitrogen impurity ($>10^{17}$ cm^{-3}) [1]. The radiation defects, produced in a diamond sample (X20) by exposure to a neutron flux in a nuclear reactor, were transformed by isothermal annealing at 550°C in a vacuum of 6×10^{-3} Torr for various times (varied within several tens of hours), with periodic extraction of the sample from the furnace. In order to provide for a better resolution of the absorption peaks in the visible rage, the spectra were measured upon cooling the sample to 80 K.

Figure 1 shows the optical absorption spectra measured on the sample upon irradiation in an IR-8 reactor and subsequent isothermal annealing for t = 10, 20, and 30 h. The spectra exhibit the following clearly distinguishable peaks (nm): 741 (1.673 eV; defect type, GR1) [1–6], 723 (1.713 eV) [7], 594.4 (2.086 eV) [3, 8], 503.2 (2.463 eV) [1, 3–5], 486 (2.549 eV), 470 (2.638 eV; defect type, TR12) [1, 3, 6], 465 (2.664 eV), 446 (2.781 eV), 429 (2.888 eV; defect type, N3) [3]. Ann additional weakly resolved peak is observed at 657.4 nm (1.837 nm).

As seen from Fig. 1, the annealing results in variation of the relative peak intensities, including both the growth of some peaks (594.4 and 503.2 nm; defect type, H3) and the drop of some others (741 nm (GR1), and 723, 675.4, 446, and 429 nm). No changes were observed in intensity of the peaks at 465, 470 (TR12), and 486 nm), probably, because the annealing duration

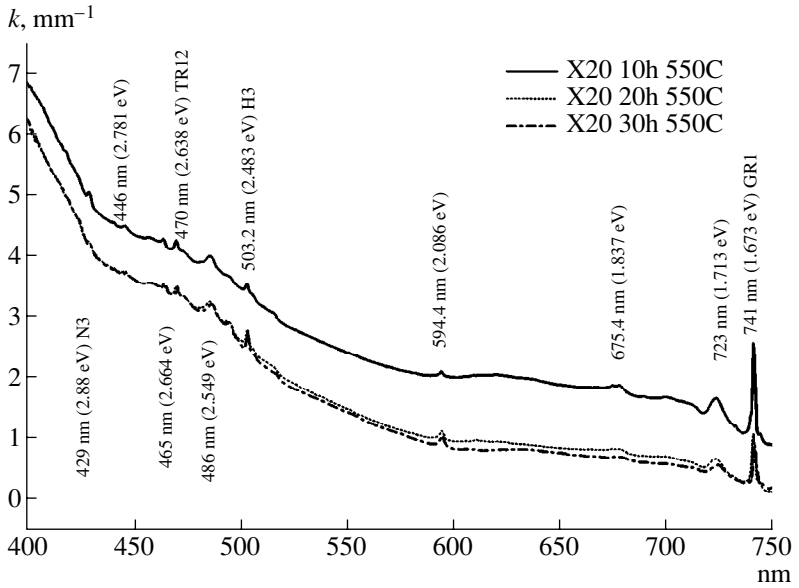

Fig. 1. Variation of the optical absorption spectra (specific absorbance k, mm^{-1}, versus wavelength λ, nm) measured at 80 K for the type IIa diamond sample X20 irradiated in the IR-8 reactor and isothermally annealed at 550°C for t = 10, 20, and 30 h.

1063-7850/00/2606-0464$20.00 © 2000 MAIK "Nauka/Interperiodica"

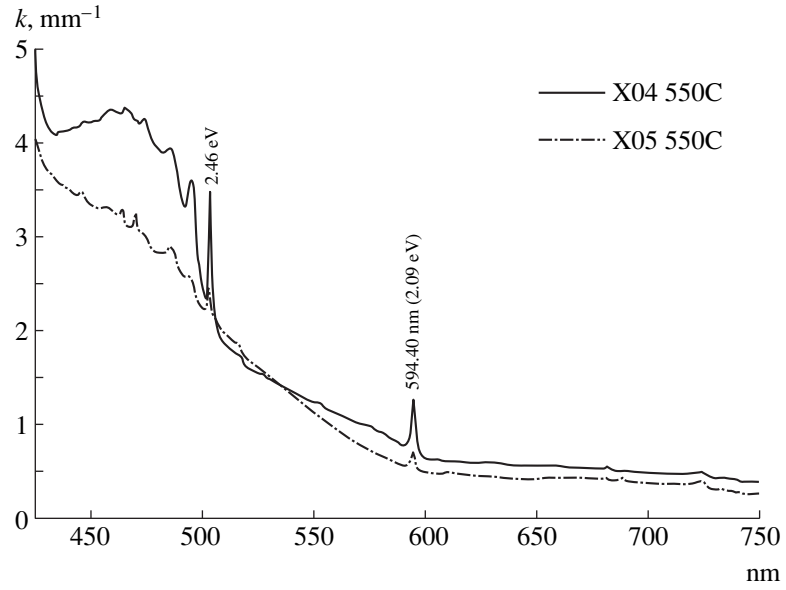

Fig. 2. The optical absorption spectra (specific absorbance k, mm^{-1}, versus wavelength λ, nm) measured at 80 K for the type IaA (sample X04) and type IIa (sample \$05) diamonds irradiated in the IR-8 reactor and isothermally annealed at 550 °C for t = 50 h.

(several tens of hours at 550°C) was insufficient for manifestation of the corresponding defect kinetics.

Taking into account that the amount of annealed defects (decreasing with increasing annealing time) is proportional to the area under the absorption peak and can be described by a sum of two (fast and slow) exponents [4, 5], the density of these defects normalized to unity can be expressed as

$$A = (a_1/(a_1 + a_2))\exp(-t/\tau_{fast}) + ((a_2/(a_1 + a_2))\exp(-t/\tau_{slow}). \quad (1)$$

The normalized density of unannealed (multiplicated) defects increases with time as

$$A = 1 - (a_1/(a_1 + a_2))\exp(-t/\tau_{fast}) - (a_2/(a_1 + a_2))\exp(-t/\tau_{slow}). \quad (2)$$

The unknown coefficients a_1, a_2, τ_{fast}, and τ_{slow} can be determined from the experimental data (Fig. 1). Note that the sum of coefficients at the exponents in equations (1) and (2) is unity.

An analysis of the experimental data obtained during the isothermal annealing (550°C) of a radiation-induced defect manifested by the peak at 723 nm showed that the time variation of the defect density can be described by the equation

$$A_{723} = 0.56\exp(-t/5.25) + 0.44\exp(-t/81.59). \quad (3)$$

Here, the defect density was normalized to unity according to formula (1) before annealing of the diamond sample (t = 0, A_{723} = 1). The decay time constants of the slow components for the defects manifested at 723 and 741 nm were quite close to each other (81.59 and 94.98 h).

According to the exponential decay model, a considerable decrease (to a level of exp(–4) ≅ 0.02) of the fast and slow decay components for the 723-nm defect is observed upon the annealing at 550°C for $t = 4\tau_{fast}$ = 21.0 h and $t = 4\tau_{slow}$ = 326.16 h, respectively.

The density of defects manifested at 594.4 nm increases with the annealing time in IIa diamond by the law

$$A_{594.4} = 1 - 0.30\exp(-t/20) - 0.70\exp(-t/350). \quad (4)$$

As is known, the growth of this defect continues during the annealing at temperatures up to 1000 K [3]. The defect structure begins to breaks at 1100 K and is completely annealed at 1300 K. The growth of this defect was not correlated with the behavior of the GR1 defects (with decreasing density), while there is a definite relationship with the growth reported for H3:

$$A_{GR1} = 0.74\exp(-t/12.34) + 0.26\exp(-t/94.98), \quad (5)$$

$$A_{H3} = 1 - 0.74\exp(-t/12.34) - 0.26\exp(-t/94.98). \quad (6)$$

During the annealing at 550°C, the density of GR1 drops to a level of exp(–4) = 0.02 after 250 h, while the density of H3 increases by this time to 0.981 of the nominal value.

It was reported that the concentration of the TR12 defects in a sample annealed at 460°C increases during 5 h and then remains constant. No defects with such dynamics were observed under our experimental conditions (550°C, 10–30 h) for the times exceeding 5 h.

The absorption peak assigned to the uncharged vacancies V_0 (429 nm; GR2, GR3) decreases in the course of annealing according to equation (1) with the

coefficients $a_1/(a_1 + a_2) = 0.81$, $\tau_{fast} = 4.48$ h, and $\tau_{slow} = 60.40$ h.

We have also observed another decreasing peak at 446 nm not previously reported in the literature. The behavior of this peak is also described by equation (1) with the coefficients $a_1/(a_1 + a_2) = 0.37$ and the characteristic fast and slow component ties $\tau_{fast} = 7.24$ h, and $\tau_{slow} = 330.43$ h.

In order to gain additional statistics, we have continuously annealed two other samples (X04, IaA type; X05, IIa type) for 50 h at the same temperature. After this prolonged annealing, amplitudes of the peaks at 741, 723, and 675.4 nm significantly dropped and could be no longer resolved in the spectra. At the same time, amplitudes of the growing peaks at 594.4 and 503.2 nm markedly increased, while all the other peaks remained unchanged, probably, because the annealing temperature (550°C) was insufficient to modify the defect structures (Fig. 2).

Thus, we have studied isothermal annealing of the radiation- induced defects in natural diamonds of the IIa type and determined coefficients of the equations describing the dynamics of variation of the density of defects corresponding to well resolved peaks in the visible range of the optical absorption spectra. The experimental data reveal the transformation of GR1 defects into H3.

The authors are grateful to the staff of the IR-8 reactor (Kurchatov Institute of Atomic Energy, Moscow) and Yu.A. Kashchuk for their help in the irradiation of diamond samples.

The work was supported by the International Science and Technology Center, project no. 447.

REFERENCES

1. *Natural Diamonds in Russia*, Ed. by V. B. Kvaskov (Polyaron, Moscow, 1997).
2. C. D. Clark and J. Walker, Diamond Res., 2 (1972).
3. G. Davies, Nature **269**, 498 (1977).
4. G. Davies, S. C. Lawson, A. T. Collins, *et al.*, Phys. Rev. B **46**, 13157 (1992).
5. G. Davies and A. T. Collins, Diamond Relat. Mater. **2**, 80 (1993).
6. L. Allers, A. T. Collins, and J. Hiscock, Diamond Relat. Mater. **7**, 228 (1998).
7. A. Osvet, V. Palm, and I. Sildos, J. Appl. Phys. **79**, 8290 (1996).
8. G. Davies and M. H. Nazare, J. Phys. C **15**, 4127 (1980).

Translated by P. Pozdeev

Technical Physics Letters, Vol. 26, No. 6, 2000, pp. 467–469. Translated from Pis'ma v Zhurnal Tekhnicheskoĭ Fiziki, Vol. 26, No. 11, 2000, pp. 41–46.

Energy and Mechanism of Quasimicroplastic Deformation in Solids

G. G. Kochegarov

Joint Institute of Geology, Geophysics, and Mineralogy, Siberian Division, Russian Academy of Sciences, Novosibirsk, 630090 Russia

Received January 10, 2000

Abstract—The mechanism of inelastic quasimicroplastic deformation revealed earlier in solids in the range of very low strains ($\varepsilon \approx 10^{-6}$) has been considered. The calculation of the energy density of the quasimicroplastic deformation shows that it proceeds by the mechanism of single structural relaxation events in the vicinity of point defects in the lattice. © *2000 MAIK "Nauka/Interperiodica".*

We have studied irreversible quansimicroplastic (QMP) room-temperature deformation in the range of low strains ($\varepsilon \approx 10^{-6}$), which is usually considered as elastic deformation. The QMP deformation was observed for all types of both plastic and brittle materials characterized by qualitatively opposite trends in the physical and mechanical properties and, hence, can be regarded as a fundamental property of solids [1].

The plane-parallel plates of various materials were tested by the of three-point bending method according to the loading–unloading scheme with a 1- to 2-s-long stepwise increase of loading in the range of initial deformation. The total deformation of loaded samples was measured by the opticomechanical method, after which the samples were unloaded and their residual deformation was measured. No material creep was observed during these tests. A more detailed description of these tests is given elsewhere [1].

Stresses resulting in the irreversible QMP deformation ($\sigma = 5 \times 10^4$–10^5 Pa) are lower by about six orders of magnitude than the theoretical ultimate shear strength, by about four orders, than the yield point and the real ultimate strength, and by two orders than the stress of microplastic flow in metals (i.e., the minimum stress giving rise to a dislocation motion [2]) [1]. The potential Peierls barrier, which should be overcome by moving dislocations in covalent crystals, is much higher than the barrier in plastic metals. Calculations show that the activation energy per unit dislocation length in copper is smaller by five orders of magnitude than that in corundum, whereas the critical shear stress σ_c is smaller by four orders of magnitude in copper than in corundum. In other words, the critical stresses of the dislocation motion in copper, σ_c, and in a covalent crystal, σ, are related as $\sigma_c \sim 10^{-4}\sigma$ [1, 3], which explains a comparatively high brittleness of the covalent crystals. The calculated value of the critical shear stress σ in covalent crystals is higher by about five orders of magnitude than the stress of the QMP deformation measured in our experiments [1]. All these facts indicate that the mechanism of QMP deformation is of a specific nature, not related to the collective motion of dislocations. In order to elucidate the mechanism of QMP deformation, we have to estimate the energy stored by a solid during deformation.

The potential energy of elastic stresses in a solid is a function of the stress and displacement tensors, which, in the general case, can be represented as

$$dU = \sum_{i,k=1}^{3} \bar{\sigma}_{i,k} ds_{i,k},$$

where $\bar{\sigma}_{i,k}$ and $s_{i,k}$ are the components of the stress and strain tensors, respectively.

Reducing the above expression to the principal axes of the stress tensor, we arrive at the relationship

$$dU = \sum_{i}^{3} \bar{\sigma}_{ii} ds_{ii},$$

where $\bar{\sigma}_{ii}$ are the principal stresses and s_{ii} are the diagonal components of the strain tensor, which, for isotropic media, are related as $s_{ii} = (\sigma_{11}/E) - \nu(\sigma_{22} + \sigma_{33})/E$, where E is Young's modulus and ν is Poisson's ratio.

The energy stored by a solid during deformation can be estimated under the assumption that, in the first approximation, $\sigma_{11} = \sigma_{22} = \sigma_{33} = \sigma$. Thus, we obtain

$$dU = 3\sigma ds_{ii}, \quad (1)$$

$$s_{ii} = s(1 - 2\nu)/E. \quad (2)$$

Solving (1) and (2) simultaneously, performing integration (at $\nu = 0.3$), and taking into account that $E = 2G(1 + \nu)$ (where G is the shear modulus), we arrive at the relationship for estimating the energy density in a solid undergoing shear deformation

$$U = 0.5\sigma^2/G.$$

1063-7850/00/2606-0467$20.00

A similar expression was used to estimate the elastic energy density and the mechanical decrement for a copper sample in the fatigue tests [4].

Under shear stresses, $G = \sigma/\tan\alpha$ (where α is the shear angle) and, therefore, $U = 0.5\sigma\tan\alpha$. If a dislocation migrates along the sliding direction, the mutual displacement of two atoms located on different sides of the sliding plane is determined as the function $s(x) = s(\tan\alpha)$. The total path of a dislocation moving in the Peierls potential relief is $S = \sum s_i(x) = \sum s_i(\tan\alpha) = \varepsilon_q$, where ε_q is the relative residual strain of the sample or, in our case, the QMP deformation, which can be determined experimentally. Therefore, the energy density of the QMP deformation can be estimated using the relationship

$$U_q = 0.5\sigma\varepsilon_q. \quad (3)$$

The energy density of plastic deformation can be estimated by the relationship $U_p = EN$, where $N = l/V$ is the dislocation density in the volume V, $E = (Gb^2l/4\pi)\ln(R/r)$ is the dislocation energy (where b is the Burgers vector, R is the dislocation radius, r is the radius of the dislocation core, and l is the dislocation unit length). The energy of the dislocation unit length in copper, determined from the above formula upon the substitution of the parameters characteristic of copper samples ($G = 4.9 \times 10^{10}$ Pa, $b = 2.56 \times 10^{-10}$ m, $R = 1 \times 10^{-2}$ m, $r = 1 \times 10^{-10}$ m [6]), is $E = 4.47 \times 10^{-11}$ J/cm. Taking for a deformed metal $N = 10^{12}$ cm^{-2} [6], we obtain for copper $U_p = 44.7$ J/cm^3 (which agrees, to within the order of magnitude, with the latent energy of deformation in copper experimentally determined at the average degree of sample deformation 28.8 J/cm^3 [7]).

The energy densities of the QMP deformation in various materials, U_q, estimated by (3) using the experimentally determined ε_q values, are given in the table. It is seen that the U_q values of the materials tested are smaller by 8–10 orders of magnitude than the energy density of the same material experiencing plastic flow, U_p. As is also seen from this table, the QMP properties are also inherent in some typical brittle materials such as cast iron, glass, and marble, which are characterized by the absence of noticeable plastic deformation before fracture. We would like to especially point out the data on the QMP deformation of polished single-crystal samples of natural and synthetic quartz, germanium and silicon possessing, a higher degree of their structural perfection, a high brittleness, in comparison with that of the corresponding polycrystal line samples. The nature of chemical bonding in covalent crystals [1] excludes any noticeable plastic flow in these crystals even at high stresses and temperatures [8, 9]. It was also emphasized [10] that, below a certain temperature (250°C for germanium and 600°C for silicon), the mechanism of plastic deformation in covalent crystals exhibits substantial changes. However, as is seen from the table, high brittleness of covalent single crystals does not exclude the manifestation of noticeable QMP properties in these crystals.

Along with the estimates of the activation energy and the critical shear stress of the dislocation motion [1], our energy density calculations for the QMP deformation show that the generation of dislocations and the formation of a dislocation structure during QMP deformation is impossible even for a typical plastic material such as copper. Thus, the QMP deformation has a specific nature different from the nature of the mechanisms of macro- and microplastic flow in metals. Comparable levels of energy losses during the QMP deformation in materials possessing opposite trends in the physical and mechanical properties indicate that the mechanism of the QMP effect is the same in various classes of solids.

Variation of the structural and mechanical properties of solids under various mechanical factors (resulting in the destruction of their crystal lattice) and the action of the liquid phase on the crystal structure and strength of various materials were considered in [11, 12]. It was shown that mechanical properties of solids are directly related to the character of imperfections in their real structure characterized by the presence of various defects and microdistortions (vacancies, atoms in metastable states, dislocations, crowdions, etc.). Elastic pulses in a solid, which can be generated even by very small mechanical actions, may give rise to substructural changes in the region of defect localization [12]. The use of the above concepts can help in elucidation of the QMP mechanism.

Since the nucleation and motion of dislocations during the QMP deformation are impossible because of

Energy density of the QMP deformation in solids

No.	Material	U_k, J/cm^3	ε, 10^{-6}	No.	Material	U_k, J/cm^3	ε, 10^{-6}
1	Quartz (natural single crystal)	3.4×10^{-8}	0.8	2	Quartz (synthetic single crystal)	7.1×10^{-9}	0.4
3	Silicon (single crystal)	4.1×10^{-9}	0.6	4	Silicon (polycrystal)	1.0×10^{-7}	1.0
5	Germanium (single crystal)	3.2×10^{-8}	0.9	6	Cast iron	4.8×10^{-7}	3.6
7	Copper	1.1×10^{-7}	1.1	8	Glass	3.0×10^{-8}	0.8
9	Marble	3.0×10^{-8}	2.1	10	Quartz (fused)	2.1×10^{-8}	0.6

insufficient energy transferred to a solid, it can be assumed that the QMP deformation proceeds by the mechanism of single structural-relaxation events in the vicinity of defects, which requires a considerably lower energy. Indeed, it is well known that the energy U required for the generation and migration of point defects varies within $(1.2–4.4) \times 10^{-19}$ J [6]. Therefore, proceeding from the energy U_q absorbed by a solid, one can state that the QMP deformation, e.g., in a copper sample, can give rise up to 10^{12} cm^{-3} point defects. This is consistent with the data on the number of point defects formed during the plastic deformation in NaCl ($\varepsilon = 10\%$)—~10^{18} cm^{-3} [13]. However, atoms occurring in nonequilibrium positions in the region of defect localization are not located in the potential minima and, therefore, can migrate into more stable positions by overcoming lower energy barriers than those overcome by an atom located at the crystal lattice site. With due regard for these facts, one can assume that the energy of QMP deformation is spent mainly for displacing the vacancies or atoms from metastable positions in defect regions of the lattice to more stable positions. This conclusion is also confirmed by data on the migration energies of defects [6], which, on the average, are almost half as small as the energies of their generation.

REFERENCES

1. G. G. Kochegarov, Pis'ma Zh. Tekh. Fiz. **25** (17), 29 (1999) [Tech. Phys. Lett. **25**, 688 (1999)].
2. E. F. Dudarev, *Microplastic Deformation and Yield Stress of Polycrystals* (Tomsk. Univ., Tomsk, 1988).
3. A. H. Cottrell, *Theory of the Crystal Dislocation* (Blackie, London, 1964).
4. N. Mott, in *Dislocations and Mechanical Properties of Crystals* (Wiley, New York, 1958), pp. 315–337.
5. G. G. Kochegarov, Dokl. Akad. Nauk **350**, 187 (1996) [Phys. Dokl. **41**, 399 (1996)].
6. H. G. van Bueren, *Imperfections in Crystals* (North-Holland, Amsterdam, 1960).
7. V. I. Khotkevich, É. F. Chaĭkovskiĭ, and V. V. Zashkvara, Dokl. Akad. Nauk SSSR **90**, 483 (1954).
8. I. S. Delitsin and A. G. Zhabin, Dokl. Akad. Nauk SSSR **234**, 433 (1977).
9. E. V. Tsinzerling, Zap. Vses. Mineral. O–va **986**, 213 (1969).
10. V. I. Trefilov and Yu. V. Mil'man, Dokl. Akad. Nauk SSSR **153**, 824 (1963) [Sov. Phys. Dokl. **8**, 1240 (1963)].
11. G. G. Kochegarov, Izv. Akad. Nauk SSSR, Neorg. Mater. **24**, 73 (1988).
12. G. G. Kochegarov, Izv. Sib. Otd. Akad. Nauk SSSR, Ser. Khim. Nauk **1** (2), 65 (1986).
13. A. V. Stepanov and E. A. Mil'kamanovich, Zh. Éksp. Teor. Fiz. **21**, 401 (1951).

Translated by L. Man

Technical Physics Letters, Vol. 26, No. 6, 2000, pp. 470–471. Translated from Pis'ma v Zhurnal Tekhnicheskoĭ Fiziki, Vol. 26, No. 11, 2000, pp. 47–51.

A Capacitance Technique for the Study of Trapping Centers in Powdered Luminophors

E. M. Bibanina, V. A. Goryunov, B. N. Denisov, and E. V. Nikishin

Mordvinian State University, Saransk, Mordvinia, Russia

Received December 17, 1999

Abstract—A method of thermostimulated capacitance (TSC) measurements is suggested for the investigation of trapping centers and energy band structure of powdered luminophors with the recombination emission type. Expressions were derived for the capacitance of a luminophor layer in a slit planar structure. A ZnS–In luminophor was studied using a special sample configuration adapted for the TSC measurements. © *2000 MAIK "Nauka/Interperiodica".*

Using parallel measurements implementing various thermoactivated effects, it is possible to determine parameters of the charge trapping centers and the energy band structure of semiconductor crystals and films [1]. Powdered luminophors are predominantly studied by methods based on the thermoluminescence (TL) and photostimulated current measurements, which sometimes fail to reveal the trapping centers present in the samples.

We believe that implementation of the method of thermostimulated capacitance (TSC) measurements in powdered materials would provide for a higher quality of the impurity monitoring in luminophors used in various light sources and data display systems. The TSC method can be based on the phenomenon of the external field screening by free charge carriers in a symmetric metal–insulator–metal structure [2–4]. The capacitance of these structures depends on the applied voltage and the concentration of free charge carriers.

We have studied the powdered semiconductor materials by TSC method using special slit planar structures comprising a system of parallel conducting (aluminum) interdigital strip electrodes formed by a photolithographic method on a sitall (glass-ceramic) substrate (Fig. 1a). A distance between the electrode strips was comparable to the luminophor grain size (40 μm) and the metal strip width was 16.7 μm. Then, the substrate surface with electrodes was coated with luminophor in the form of a suspension in ethanol (3–5 g/cm^3). Using this method of application allowed the material to be studied in the "pure" form, excluding the possible effects of binding agents on the electrical properties of samples. Simplicity of the application and removal of a luminophor layer made it possible to use the same substrate matrix with various luminophors, which provided better reproducibility of the other experimental conditions. Note that the studied systems are somewhat analogous to the metal–insulator-semiconductor structures formed on the surface of aluminum contacts as a result of insulating aluminum oxide layer formation upon oxidation in air.

Figure 1b shows an equivalent electrical scheme of the planar structure studied. According to this scheme, the capacitance of this structure is

$$C = C_s + \frac{C_d C_{l.eq}}{C_d + 2C_{l.eq}} \simeq C_s + C_{l.eq}, \qquad (1)$$

where $C_{l.eq}$, C_s, and C_d are the capacitances of the luminophor layer, sitall substrate, and dielectric (insulator)

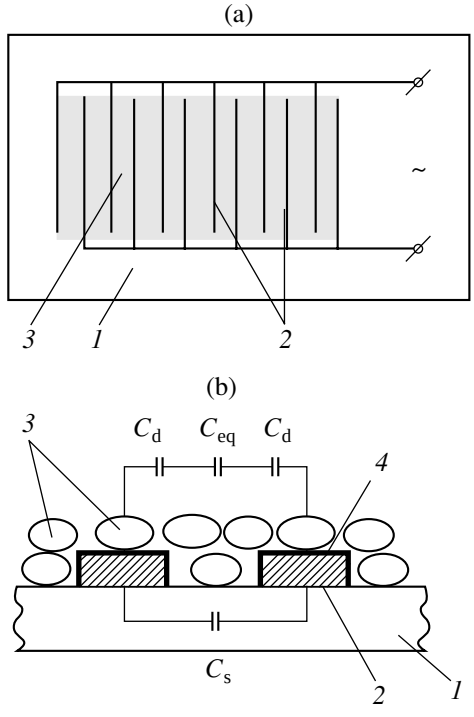

Fig. 1. Schematic diagrams of (a) a planar electroluminescent capacitor structure and (b) an equivalent electrical scheme: (*1*) glass-ceramic (sitall) substrate; (*2*) aluminum electrodes; (*3*) luminophor layer; (*4*) insulator layer.

1063-7850/00/2606-0470$20.00 © 2000 MAIK "Nauka/Interperiodica"

layers, respectively, and the approximation takes into account that $C_{l.eq} \ll C_d$. Since the luminophor is not continuous, the equivalent capacitance of this layer can be written, using the Odelevskiĭ relationship for the dielectric permittivity of a statistical two-component system (luminophor in air or vacuum) [5], in the following form:

$$C_{l.eq} = C_0\left(1 + \frac{x_2}{(1-x_2)/3 + x_2/(C_l/C_{0l} - 1)}\right), \quad (2)$$

where x_2 is the layer fraction occupied by luminophor, C_0 is the geometric capacitance of the region occupied by luminophor, C_l is the capacitance of a continuous luminophor layer of the same thickness, and C_{0l} is the voltage-independent capacitance of the luminophor layer (the dielectric permittivity of air is taken equal to unity). The value of C_l can be expressed as [4]

$$C_l = \frac{q(N_s + N_{scv} + N_{s0})}{U}, \quad (3)$$

where N_{s0} is the surface density of equilibrium free charge, N_{scv} is the bound surface charge density, and N_s is the surface density of the charge induced by external factors (temperature, illumination, etc.); in low-conductivity (high-resistivity) semiconductors, $N_{s0} \ll N_s$. Taking into account that $qN_{scv}/U = C_{0l}$, we obtain $C_l = C_{0l} = qN_{scv}/U$ and

$$C_{l.eq} = C_0\left(1 + \frac{x_2}{(1-x_2)/3 + x_2 C_{0l}U/qN_s}\right). \quad (4)$$

The induced surface charge density can be written as $N_s = n_s L_{eq}$ [4], where n_s is the concentration of nonequilibrium (minority) free charge carriers and L_{eq} is the size equivalent to the interelectrode gap. If the function $n_s = f(T)$ has a maximum, then the position of this maximum would coincide with that of the curve $C_{l.eq} = C_{l.eq}(T)$ in the temperature region where $\varepsilon_l(T) = \text{const}$ (since $dC_{l.eq}/dT = 0$ when $\partial n_s/\partial T = 0$). Therefore, upon determining the temperature of maximum for $C_{l.eq}(T)$, we may calculate the energies of levels corresponding to the trapping centers using the well-known relationships for the thermostimulated current. The TSC method outlined above can be applied to luminophors in which ionization of the emitting and trapping centers is accompanied by transitions to the conduction band.

For example, we will present the results of investigation of the trapping centers in a ZnS–In luminophor by TL and TSC method. The capacitance of the sample structure was measured by an MPP-300 total conductivity bridge. For small variations of the sample capacitance, the bridge unbalance is proportional to ΔC_{eq}. The out-of-balance signal, amplified by a lock-in U2-8 amplifier, entered to the *Y*-input of an N-307 *X*–*Y* recorder, and the thermocouple signal entered the *X*-input. The luminophor was excited and the TSC curve measured under the conditions conventional for the thermostimulated luminescence and current measurements.

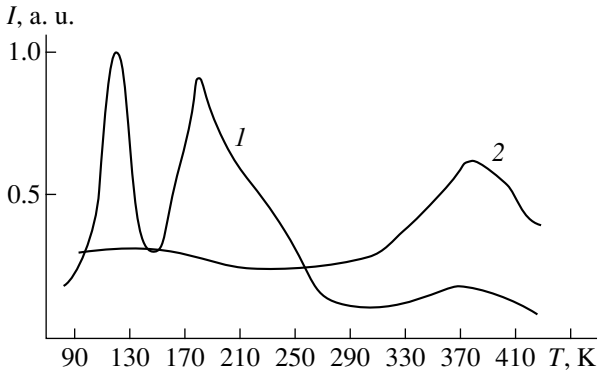

Fig. 2. Experimental curves of (*1*) thermoluminescence and (*2*) thermostimulated capacitance for a ZnS–In luminophor.

Figure 2 shows the TL and TSC curves measured for a ZnS–In luminophor. The TL curve exhibits three low-temperature peaks (T_1 = 123 K, T_2 = 183 K, and T_3 = 228 K) and one peak at elevated temperatures (T_4 = 383 K), which is significantly distorted as a result of the temperature-induced luminescence quenching. The corresponding trapping centers are characterized by the energies E_1 = 0.26 eV, E_2 = 0.395 eV, E_3 = 0.492 eV, and E_4 = 0.89 eV. A single peak observed in the TSC curve is situated at T = 383 K.

Using these experimental data, we may refine the energy band diagram of this luminophor. The TSC curve indicates that the thermal devastation of low-temperature traps is not accompanied by the appearance of free charge carriers. Therefore, excited states of the corresponding trapping centers occur in the forbidden band at a distance of E_1, E_2, and E_3 from the ground state. In the region of positive temperatures on the centigrade scale, the devastation of traps is accompanied by the production of free charge carriers which recombine via the conduction bands.

REFERENCES

1. V. N. Vertoprakhov and E. G. Sal'man, *Thermostimulated Currents in Inorganic Substances* (Nauka, Novosibirsk, 1979).
2. M. K. Samokhvalov, Pis'ma Zh. Tekh. Fiz. **23** (6), 1 (1997) [Tech. Phys. Lett. **23**, 210 (1997)].
3. N. F. Kovtonyuk, *Electronic Elements Based on Semiconductor–Insulator Structures* (Énergiya, Moscow, 1976).
4. Yu. D. Dumarevskiĭ, N. F. Kovtonyuk, and A. I. Savin, *Image Transformation in Semiconductor–Insulator Structures* (Nauka, Moscow, 1987).
5. N. P. Bogoroditskiĭ, Yu. M. Volokobinskiĭ, and A. A. Vorob'ev, *Theory of Insulators* (Énergiya, Moscow, 1965).

Translated by P. Pozdeev

Technical Physics Letters, Vol. 26, No. 6, 2000, pp. 472–474. Translated from Pis'ma v Zhurnal Tekhnicheskoĭ Fiziki, Vol. 26, No. 11, 2000, pp. 52–56.

Simulation of the Current Switching by a Metal–Insulator Transition

Yu. B. Kudasov and V. N. Pavlov

Institute of Experimental Physics, Russian Federal Nuclear Center, Sarov, 607200 Russia

Received December 15, 1999

Abstract—A one-dimensional simulation of the nonlinear diffusion of magnetic field through a shield made of the solid solution $(V_{1-X}Cr_X)_2O_3$ is carried out. Also simulated is the current switching from this shield to load when the former undergoes a metal–insulator transition. Pronounced steepening of a current pulse edge in the load circuit is demonstrated to be possible. © *2000 MAIK "Nauka/Interperiodica".*

This paper continues the study reported in [1], where a one-dimensional model has been suggested to describe the diffusion of magnetic field into a substance experiencing a metal–insulator transition under the Joule heating conditions, the solid solution $(V_{1-X}Cr_X)_2O_3$ being used as a model substance. The nonlinear diffusion could be exploited in high-current pulse switches [2]. The device in its simplest form is based on the magnetic diffusion through a shield situated between the cavity of a current source and that of a load circuit.

The analytical solutions presented in [1] were essentially derived for the stationary diffusion in infinite media. To make a further step toward practice, we consider the case of pulsed current (magnetic field) and a shield of finite thickness. It would be important to analyze the switching process in terms of the pulse shape and shield boundary conditions, although the analysis can be performed only numerically.

Let a current source and an *R–L* load circuit be connected by a strip line, as shown by Fig. 1. Initially, the load is shorted out by a rectangular shield made of the solid solution $(V_{1-X}Cr_X)_2O_3$. The solution composition is specially selected $X \approx 0.0055$ so that it undergoes a metal–insulator transition if heated by about 100 K above a starting temperature (room temperature). To roughly estimate the propagation of a current pulse, the shield may be considered as a transmission line with distributed inductance and conductance, the line conductivity being variable (Fig. 1).

We consider the current switching from shield to load as the one-dimensional nonlinear diffusion of the magnetic field **B** through the shield, neglecting the edge effects related to a finite strip width and to possible instabilities of the phase boundary [3]. The magnetic field is assumed to depend on the coordinate x and time t only. Following [1], we write a magnetic field diffusion equation as

$$\frac{\partial \mathbf{B}}{\partial t} = \mathrm{rot}(\mathbf{u} \times \mathbf{B}) - \mathrm{rot}(\nu_m \mathrm{rot}\,\mathbf{B}), \qquad (1)$$

where $\nu_m = c^2/4\pi\sigma$ is the magnetic viscosity and σ is the conductivity. It has been demonstrated previously that a typical pulse length, which lies in the microsecond range, corresponds to a small Reynolds number [1]. We may therefore omit the mass transfer term in the right-hand side of (1), arriving at

$$\frac{\partial B}{\partial t} = \frac{\partial}{\partial x}\left(\nu_m \frac{\partial}{\partial x} B\right). \qquad (2)$$

Equation (2) is written in a scalar form because **B** has a single component perpendicular to the plane of Fig. 1.

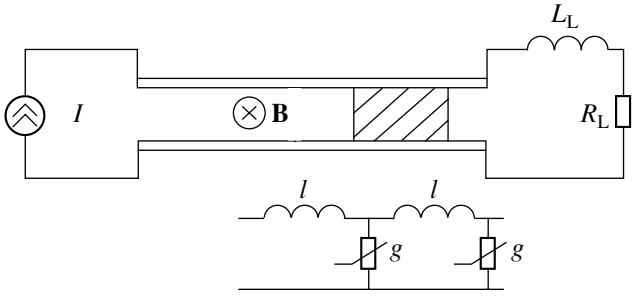

Fig. 1. One-dimensional model of the current switch (the shield being represented by the hatched box): I = current in the source, L_L = load inductance, R_L = load resistance, l = shield inductance per unit length, and g = shield conductance per unit length.

1063-7850/00/2606-0472$20.00 © 2000 MAIK "Nauka/Interperiodica"

Furthermore, the Joule heat absorbed in the shield obeys the equation

$$\frac{\partial Q}{\partial t} = \frac{\nu_m}{4\pi}(\nabla B)^2. \quad (3)$$

As the last step, we define a model dependence of σ on Q for $(V_{1-x}Cr_x)_2O_3$. If $Q < 350$ J/cm^3, then $\sigma = 10^3$ (Ω cm)$^{-1}$. When Q rises from 350 to 357 J/cm^3, then σ linearly decreases to 10 (Ω cm)$^{-1}$. At higher Q, the conductivity remains constant. The value 7 J/cm^3 corresponds to the latent heat of the phase transition. The other parameter values are as in [1]. Also recall that all types of heat transfer in the shield can be neglected, since the process takes a few tens of microseconds [1].

Equations (2) and (3) with the relation $\sigma(Q)$ constitute the system under study, describing the nonstationary magnetic field diffusion through the shield. The initial condition for (1) is $B(x) = 0$. The boundary condition for the front (source) side of the shield corresponds to the magnetic field (or current) created by the current source in the strip. The boundary condition for the rear (load) side of the shield is dictated by the load determining a relationship between the magnetic field strength and its derivatives with respect to x and t.

The main challenge facing the computation of the diffusion is the abrupt variation in σ within a narrow interval of Q. The current density in the shield changes sharply at the point of the phase transition giving rise to a singularity of the discontinuity type. Since ∇B is proportional to the current density, we may transform equation (3) to the integral form:

$$\int_0^Q \nu_m(q)dq = \frac{c^2}{4\pi}\int_0^t E^2 d\tau, \quad (4)$$

where $E = \frac{c^2}{4\pi\sigma}\nabla B$ is the electric field strength. Since $\nu_m(q)$ is the known function, the left-hand side of (4) is a known single-valued function $f(Q)$, so that one can compute the inverse function $g\{f[Q(x, t)]\} = \nu_m(x, t)$ prior to computing the diffusion. Thus, the time-dependent distribution of the magnetic viscosity is determined from

$$\nu_m(x, t) = g\left[\frac{c^2}{4\pi}\int_0^t E^2 d\tau\right]. \quad (5)$$

Note that, unlike the current density, the electric field is continuous in the vicinity of a metal–insulator interface. That is why equations (2) and (5) are easy to solve numerically.

We considered two types of the current (magnetic field) pulses. The first type is a sine wave taken over a quarter of the period, as exemplified by the discharge of a capacitor bank. The second type is characterized by the power growth $B \propto 1/(t - t_0)$, which is typical of an MK-2 magnetic-cumulation generator. In the latter case, we used a variable time step, because the derivative of the external magnetic field varies rapidly during a pulse. The pulse sharpening was nearly the same in both cases. Figure 2 presents the computed magnetic field as a function of time for different sections of the shield: the source side (curve *1*), the section at 1/3 of the shield thickness (curve *2*), the section at 2/3 of the shield thickness (curve *3*), and the load side (curve *4*). At the source and the load side, the magnetic field is proportional to the current through the source and the load, respectively. The dashed line shows the motion of the metal–insulator interface. Note that the load receives a current pulse with a materially steeper edge.

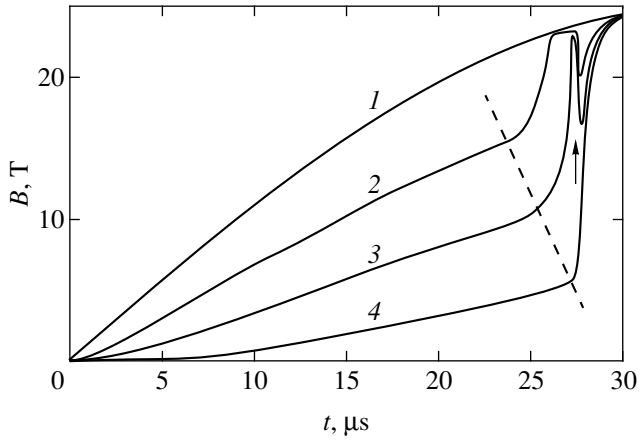

Fig. 2. Diffusion of magnetic field through the shield at L_L = 38 nH/cm and $R_L = 10^{-3}$ Ω cm (38 nH and 10^{-3} Ω for a strip width of 1 cm, respectively). The field is computed for (*1*) the source side of the shield, (*2*) the section at 1/3 of the shield thickness, (*3*) the section at 2/3 of the shield thickness, and (*4*) the load side of the shield.

The shape of current pulses in the load is governed by the load parameters. If R_L and L_L are small (the load being similar to a short circuit), then the load shunts the shield when a current wave reaches the load side of the shield. This results in slowing down the wave and smoothing the current pulse at the load. If R_L or L_L is large (Fig. 2), the voltage across the strip line rises sharply when a current wave reaches the load side of the shield. As a result, the current through the shield returns to a high level, although the shield has low conductivity now. A singularity is thus formed at this stage of the current wave propagation (indicated by the arrow in Fig. 2). The effect resembles the wave reflection in a linear network with distributed parameters. However, the network under study is essentially nonlinear.

In conclusion, we formulate an approximate condition for shield–load matching. A current wave moves through the shield, occupying a layer of thickness Δx around the metal–insulator interface. The thickness can easily be estimated from the speed of the interface [1].

We thus arrive at the following approximate equations for the optimum load parameters: $L_L = \Delta x l$ and $R_L = \Delta x/g$, where l and g are, respectively, the inductance and the conductance per unit length for the equivalent circuit of the shield (Fig. 1).

ACKNOWLEDGMENTS

This study was carried out under the auspices of the International Science and Technology Center, project no. 829.

We are grateful to Prof. J. Brooks, W. Lewis, and their colleagues for invaluable support.

REFERENCES

1. Yu. B. Kudasov, Zh. Tekh. Fiz. **68** (12), 43 (1998) [Tech. Phys. **43**, 1440 (1998)].
2. Yu. B. Kudasov, RF Patent no. 2121725; MPK 6H01F7/06, 6H01H36/00 (1998).
3. Yu. B. Kudasov and I. V. Makarov, in *Proceedings of the International Conference "Hydrodynamic Instabilities and Turbulent Mixing of Compressible Media," St. Petersburg, July 2–7, 1999*, p. 61.

Translated by A. Sharshakov

Technical Physics Letters, Vol. 26, No. 6, 2000, pp. 475–477. Translated from Pis'ma v Zhurnal Tekhnicheskoĭ Fiziki, Vol. 26, No. 11, 2000, pp. 57–61.

Luminescence Kinetics in Proton-Irradiated Quartz Glasses

P. V. Demenkov, O. A. Plaksin, V. A. Stepanov, P. A. Stepanov, and V. M. Chernov

Institute of Physics and Power Engineering, State Scientific Center of the Russian Federation, Obninsk, Kaluga oblast, 249020 Russia

Received January 10, 2000

Abstract—It is experimentally demonstrated that the intensity of the radiation-induced luminescence (RIL) of KU-1 and KI quartz glasses at 450 nm increases more than ten times upon the proton irradiation (proton energy, 8 MeV; dose rate, 5×10^3 Gy/s; dose, up to 1.2×10^7 Gy) to a dose of 10^6 Gy. At a dose exceeding 10^6 Gy, the spectral efficiency of the ionizing radiation energy conversion reached ~10^{-6} nm^{-1} in the maximum of the RIL band at 450 nm for all types of glasses. After preliminary low-rate γ-irradiation (below 0.5 Gy/s), the RIL intensity in the beginning of the proton irradiation and its variation with the proton dose depend on the concentration of impurities in the quartz glass. The RIL intensity buildup depends on the formation of positively and negatively charged microscopic regions in glasses. © *2000 MAIK "Nauka/Interperiodica".*

Radiation action upon wide-bandgap dielectrics causes recharging of their electron–hole centers by the radiation-induced charge carriers. This process is accompanied, as a rule, by the radiation-induced luminescence (RIL) [1, 2]. By studying the variation of the absolute and relative intensity of bands in the RIL spectra with increasing radiation dose, it is possible to assess the mechanisms and kinetics of formation of the optically active centers in materials. In this work, we have studied the room-temperature RIL kinetics in quartz glasses upon proton irradiation (proton energy, 8 MeV; dose rate, 5×10^3 Gy/s).

The RIL spectra of quartz glasses consist of three broad bands peaked at approximately 300, 450, and 645 nm [3]. The luminescence bands at 450 and 645 nm are usually related to an oxygen-deficit center (≡Si–Si≡) and a hole center at the non-bridging oxygen (≡Si–O), respectively [1, 3, 4]. We detected the RIL intensity variation in the course of proton irradiation in the maximum of the strongest luminescence band at 450 nm. The chemical compositions of KU-1 and two types of KI quartz glasses studied in this work are shown in the table.

As the radiation dose increases, the RIL intensity in KU-1 and KI (1) glasses grows to approximately the same level with a characteristic time of 500–1000 s (Fig. 1). By the end of the irradiation (at a total dose of about 10^7 Gy), the RIL intensity increases by a factor of approximately 20 for KU-1 and 10 for KI (1) relative to the initial level. At a dose exceeding 10^6 Gy, the RIL spectra of glasses corresponded to the published data [3].

The concentration of the noninteracting electron–hole traps filled in the course of irradiation, N_{tf}, is given by the formula:

$$N_{tf} = \frac{\rho \dot{D} \tau}{E_{e-h}},$$

where $\dot{D}$ is the dose rate (5×10^3 Gy/s), ρ is the density of the material (2.23 g/cm^2), E_{e-h} is the energy of an electron–hole pair formation (about 2–2.5 E_g), E_g is the band gap (about 9 eV) [1]. Let us assume that the characteristic time of RIL intensity buildup (about 10^3 s) is equal to the characteristic time τ of trap recharging. Then, we arrive at the value $N_{tf} \sim 10^{21}$–10^{22} cm^{-3} which appears to be physically unrealistic.

It is more probable that RIL variations are related to the process redistribution of the filled electron–hole traps in the bulk of the glass. Using Al_2O_3-based materials, Plaksin *et al.* [5] demonstrated that the RIL characteristics of wide-bandgap dielectrics are related to the formation of charged microscopic regions in the bulk of the material, which influence the charge state of the optically active centers. In particular, the increase of the RIL intensity in the band of the *F*-centers (415 nm) is determined by the formation of negatively charged

Chemical composition of glasses

Glass	Metal admixtures, at. %	OH groups, at. %
KU-1	Al, Fe, Na (<0.001)	4×10^{-2}
KI (1)	Co, Fe, Mn (<0.1)	$2–4 \times 10^{-4}$
KI (2)	Zr(0.49), Sr(0.021), As(0.005), Mo(0.06), Ba(0.9)	$2–4 \times 10^{-4}$

1063-7850/00/2606-0475$20.00 © 2000 MAIK "Nauka/Interperiodica"

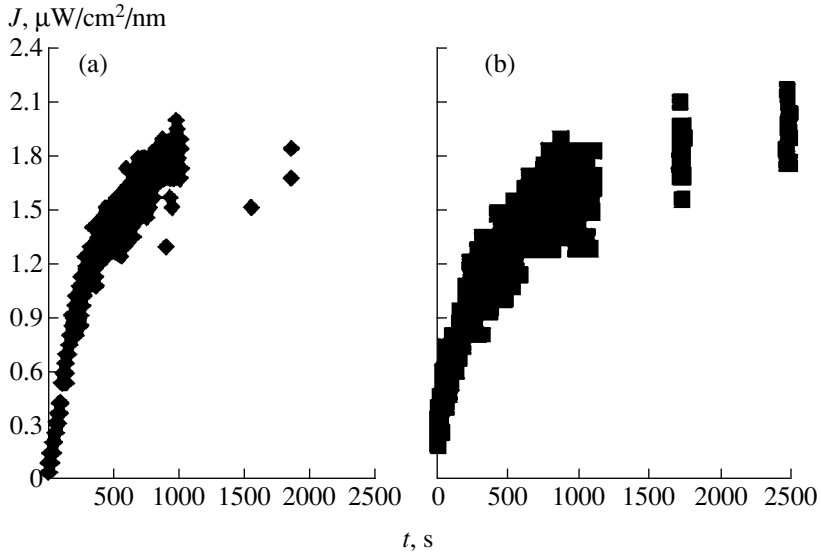

Fig. 1. Plots of the RIL intensity (λ = 450 nm) versus time for proton-irradiated quartz glasses: (a) KU-1, (b) KI (1).

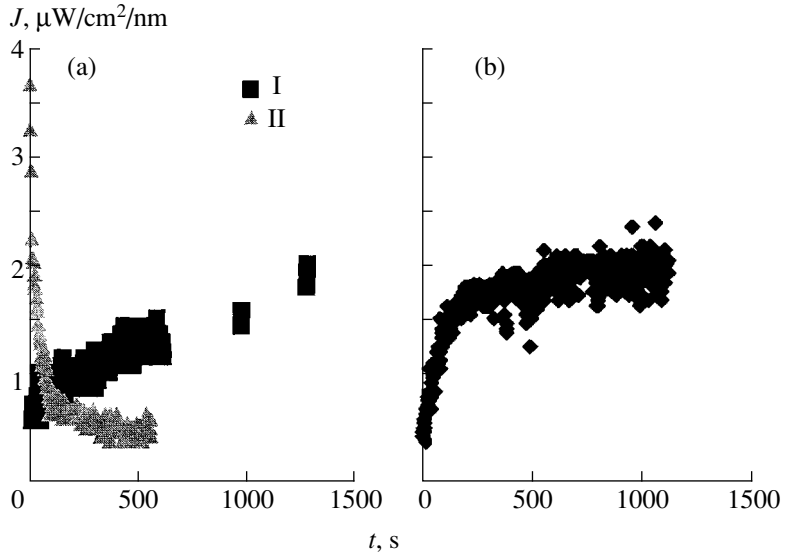

Fig. 2. Plots of the RIL intensity (λ = 450 nm) versus time for proton-irradiated quartz glasses upon preliminary γ-irradiation: (a) KI (1) (squares) and KI (2) (triangles), (b) KU-1.

regions (containing an excess of the negatively charged traps) in Al_2O_3 single crystals upon the proton irradiation (proton energy, 8 MeV; dose rate, 5×10^3 Gy/s). The negative charging of boundaries relative to the bulk of grains in $Al_2O_3 : Cr^{3+}$ ceramics was manifested by an increase in intensity of the RIL band of chromium ions (690 nm). We believe that the increase of the RIL intensity in quartz glasses is also determined by the formation of negatively and positively charged microscopic region in the bulk of the materials. Apparently, such a nonuniform distribution of the electric charge in glasses may be retained for a long time after irradiation. Repeated RLL measurements (after two weeks) in an irradiated sample showed intensive RIL in the beginning of the irradiation, followed by a slow increase with the same characteristic time (500–1000 s) as before.

Under low-intensity irradiation, the volume distribution of the charged electron–hole traps depends significantly on the concentration of the impurities in glasses. The KI (1) glass (in contrast to KI (2) and KU-1 glasses) exhibits an optically inhomogeneous state with visually detectable flaky dark areas with a typical size of 1 mm upon γ-irradiation at a dose of 10^4 Gy (Co^{60} source with a dose rate of 0.5 Gy/s).

Preliminary γ-irradiation of quartz glasses leads to a high-intensity RIL in the beginning of the proton irradiation (Fig. 2). The KU-1 and KI (1, 2) glasses were γ-irradiated to the doses of 10^8 and 10^4 Gy and stored at

room temperature for one and four years, respectively. The RIL intensity of the γ-irradiated KU-1 and KI (1) glasses (10^8 Gy and 10^4 Gy, respectively) increases with increasing dose of the proton irradiation up to the level of RIL intensity typical of the glasses that were not exposed to γ-irradiation. The γ-irradiated KU-1 glass exhibits a substantially smaller characteristic time of the RIL intensity variation in comparison with the value for the unexposed glass. On the contrary, an approximately eightfold drop of the RIL intensity with the characteristic time of about 100 s takes place in the γ-irradiated KI (2) glass (10^4 Gy). Therefore, preliminary low-rate γ-irradiation (below 0.5 Gy/s) reveals dependence of the RIL intensity and kinetics on the concentration of impurities in glasses.

REFERENCES

1. D. L. Criscom, J. Ceram. Soc. Jpn. **99**, 923 (1991).
2. V. M. Chernov *et al.*, J. Nucl. Mater. **253**, 175 (1998).
3. V. Kalantar'yan *et al.*, in *Proceedings of the International Conference on the Radiation Materials Science, Institute of Physics and Technology, Kharkov, 1991*, Vol. 9, p. 142.
4. R. Tohmon *et al.*, Phys. Rev. Lett. **62**, 1388 (1989).
5. O. A. Plaksin *et al.*, J. Nucl. Mater. **271**–**272**, 496 (1999).

Translated by A. Chikishev

Technical Physics Letters, Vol. 26, No. 6, 2000, pp. 478–480. Translated from Pis'ma v Zhurnal Tekhnicheskoĭ Fiziki, Vol. 26, No. 11, 2000, pp. 62–67.

Electrical Switching in Metal–Insulator–Metal Structures Based on Hydrated Vanadium Pentoxide

G. B. Stefanovich, A. L. Pergament, and E. L. Kazakova

Petrozavodsk State University, Petrozavodsk, 185640 Karelia, Russia

Received December 14, 1999

Abstract—The phenomenon of switching in sandwich structures based on a V_2O_5 gel was studied. The switching effect with an S-shaped *I–V* characteristic is explained by a metal–insulator transition taking place in a vanadium dioxide phase formed in the initial gel film in the course of electroforming. The switching parameters (including the threshold voltage) were studied as functions of the temperature and pressure. It is shown that these switching devices can be used as highly effective microtransducers. © *2000 MAIK "Nauka/Interperiodica".*

In recent years, there is an increasing interest of researchers toward the investigation of thin-film noncrystalline semiconductors. This is explained to a considerable extent by the development of the solid-state electronics actively implementing amorphous, glassy, and polymeric materials in various elements and functional devices. The materials are frequently obtained, in particular, by methods of "sol–gel" technology.

Hydrated compounds of vanadium, such as a vanadium pentoxide gel ($V_2O_5 \cdot nH_2O$), are of considerable interest from the standpoint of practical applications [1]. For example, planar structures based on the V_2O_5 gel were reported to exhibit a switching effect with an S-shaped current–voltage (*I–V*) characteristic [1, 2].

The phenomenon of negative differential resistance offers potential prospects for the creation of various electronic devices such as switches, generators, sensors, etc. In many cases, more convenient technical solutions are provided by sandwich structures of the metal–insulator–metal (MIM) type, rather than by the conventional planar systems, which is explained, in particular, by the general tendency toward miniaturization of the equipment [3]. This trend is related to the requirements of increasing degree of integration, reducing consumed (and dissipated) power, and growing speed of operation. However, no data were reported on the switching effect in sandwich structures based on the hydrated vanadium pentoxide. The purpose of our work was to study the phenomenon of switching in the M/V_2O_5 gel/M system and the effect of external factors (temperature and pressure) on the switching parameters.

In our work, vanadium oxide was obtained by a variant of the sol–gel method with certain modifications. A powder of vanadium pentoxide was melted in an alundum crucible in a muffle furnace (T_m = 670°C). The melt was heated to T = 900°C, homogenized at this temperature for 1 h, and rapidly quenched by pouring into water at room temperature. This results in the formation of a homogeneous gel-like solution capable of wetting substrates and spreading over a substrate surface to form a film of relatively uniform thickness. Upon drying of the solution, this film transforms into a xerogel (a gel with partly removed water). The air-dried xerogel films represent a virtually X-ray amorphous phase with a water content of n = 1.6–1.8 [1]. These films exhibit a quasi-one-dimensional layered structure with the V_2O_5 layers composed of involved fibers linked by water molecules. The thickness of V_2O_5 xerogel films may vary within broad limits, ranging from ~100 nm (for the films obtained by spin-coating) to several tens of microns.

The MIM structures were prepared by applying ~1-μm-thick gel films onto metal underlayers deposited in vacuum onto glass substrates. The upper electrodes represented a gold-coated wire pressed to the gel surface (Fig. 1a). It was found that an important factor consists in selecting a metal for the underlayer (bottom electrode). Indeed, the planar switches using Al and Cr contacts exhibited degradation in the course of operation [2]. We have used Al and Au layers, obtained by thermal evaporation and deposition in vacuum, or V layers prepared by magnetron sputtering. Aluminum and vanadium entered into chemical reactions with V_2O_5 immediately upon the gel film application, as was evidenced by alteration of the film color and etching of the metal underlayer, although the switching effect in these systems was still observed. Gold underlayers have proved to be most inert and were used in the experiments described below.

The resistance of initial sandwich structures was of the order of ~10 MΩ. Upon electroforming, the *I–V* curves of the samples became S-shaped (Fig. 1b), while the resistance of the low-conductivity (off) state decreased to $R_{off} \sim 0.5$ MΩ. The process of electroforming was qualitatively similar to that reported for the amorphous semiconductors [4], sandwich structures

1063-7850/00/2606-0478$20.00

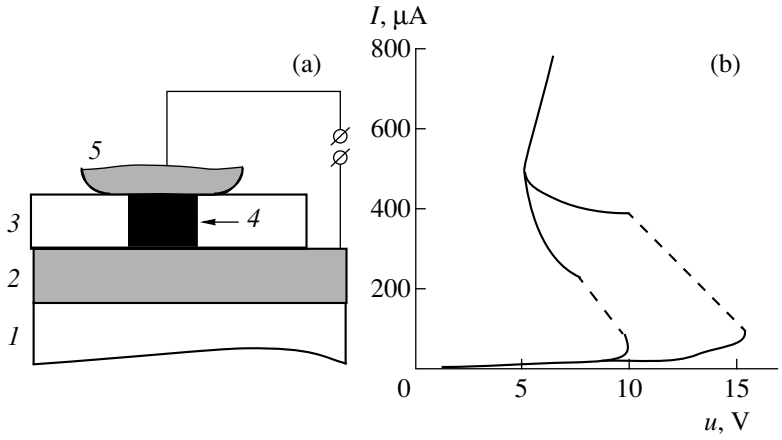

Fig. 1. (a) Schematic diagram of the MIM structure studied: (*1*) glass substrate; (*2*) gold underlayer; (*3*) V_2O_5 gel film; (*4*) vanadium dioxide switching channel; (5) pressed Au contact. (b) *I–V* curves of the MIM structure upon electroforming (T = 293 K).

based on the anodic VO_2 films [5], and planar structures based on the V_2O_5 gel [1]. The switching threshold voltage was V_{th} = 10–20 V at room temperature and decreased with increasing temperature. Figure 2 (curve *1*) shows the plot of $V_{th}(T)$, from which it is seen that $V_{th} \longrightarrow 0$ as the temperature increases to $T \approx$ 330–340°C. This value almost coincides with the temperature of the metal–insulator transition in VO_2 (T_t = 341 K) [6]. Thus, we may conclude that switching in the V_2O_5 gel based MIM structures is related to the metal–insulator transition in a vanadium dioxide phase. The $V_{th}(T)$ curve is satisfactorily described within the framework of the critical temperature model [6] typically applied to the materials featuring a metal–insulator transition.

A switching channel composed (completely or partly) of VO_2 (Fig. 1a) appears in the initial film in the course of electroforming [1, 2, 5]. In contrast to purely stoichiometric VO_2 single crystals, in which the resistance jump upon the metal–insulator transition reaches up to five orders of magnitude [6], the resistance of our samples increased only by a one–two orders of magnitude. This fact may indicate that the switching channel is composed not entirely of VO_2. The vanadium dioxide phase developed in the course of electroforming may have the shape of filaments or inclusions. In addition, the transition may be suppressed by deviation from the VO_2 stoichiometry in the channel. Note that the electroforming process may be replaced by the laser treatment [7], whereby certain areas of the film are exposed to a laser beam, which may provide for the obtaining of more stable and reproducible switching parameters.

We have studied the effect of uniaxial compression on the switching parameters. The pressure was developed by applying a load F immediately to the gold contact (upper electrode). The results of these measurements are presented by the V_{th} versus F plot in Fig. 2 (curve *2*). As the pressure p increases, the threshold voltage drops similarly to the behavior observed in amorphous semiconductors [4]. The R_{off} value decreased with increasing F as well. It was difficult to evaluate the pressure p in our experiments, since the area of contact was undetermined. A rough estimate, based on the print diameter D measured on the sample film surface observed in a microscope, for a load of F = 0.34 kgf yields $D \approx 50$ μm and $p_{max} = 4Fg/\pi D^2 \approx 2 \times 10^9$ Pa = 20 kbar (g = 9.8 m/s^2).

It should be noted that the metal–insulator transition temperature T_{tr} of VO_2 increases with the pressure p [6], which must lead in the general case to an increase in V_{th}; however, the switching parameters V_{th}, R_{off}, etc., depend not only on the T_{tr} value but on the switching channel dimensions as well, the latter being also modified by the applied pressure. Note also that, as demonstrated in [8], a uniaxial (in contrast to hydrostatic)

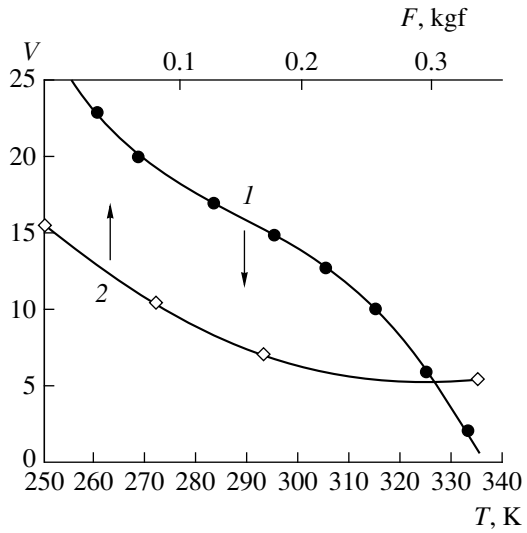

Fig. 2. The plots of threshold voltage V_{th} versus (*1*) temperature and (*2*) pressure (load) at T = 293 K.

compression may produce a decrease (rather than increase) in the transition temperature. Finally, the resistance of the semiconducting VO_2 phase may also strongly depend on the level of mechanical stresses [9].

In concluding, we would like to comment on the application aspect of the results presented above. Elements with an S-shaped *I–V* characteristic are promising from the standpoint of creating sensors for various physical parameters. Moreover, the possible generation of relaxation oscillations in systems containing these elements makes it possible to design the frequency-sensitive transducers [5], since the frequency of oscillations in the system depends on V_{th} and, hence, on the external factors. The method of frequency conversion offers obvious advantages, including high resolution, stable parameters, convenient output signal processing and computer interfacing, possibility of remote monitoring, high protection level against interference during the data transfer.

The temperature and pressure dependence of the threshold parameters of the switching devices based on vanadium pentoxide sandwich structures suggests their possible application in thin- film microtransducers sensitive to temperature and mechanical factors related to pressure (force, shift, etc.). It should be emphasized that the "vertical" sandwich MIM configuration is more convenient for the pressure transducers as compared to the planar variant, where the signal registration requires bending of the substrate [8. 9]. The task of finding new materials for microtransducers has became very urgent (see, e.g., a special issue of the *Sensor Review* journal [10] specially devoted to this subject). Important aspects of this problem are compatibility with the present-day integrated-circuit technology, the possibility of creating distributed networks (matrices) of transducers, and a number of other requirements specific for each particular type of sensors [3, 10]. We believe that the compounds featuring the metal–insulator transition (especially vanadium oxides) and switching devices based on these materials offer a promising base for the creation of such transducers.

REFERENCES

1. V. Bondarenko, V. Volkov, and A. Pleshanovis, Fiz. Tverd. Tela (St. Petersburg) **35**, 3189 (1993) [Phys. Solid State **35**, 1567 (1993)].
2. J. G. Zhang and P. C. Eklund, J. Appl. Phys. **64**, 729 (1988).
3. H. Pagnia, Int. J. Electron. **73**, 819 (1992).
4. P. J. Walsh, J. E. Hall, R. Nicolaides, *et al.*, J. Non-Cryst. Solids **2**, 107 (1970).
5. A. L. Pergament, G. B. Stefanovich, and F. A. Chudnovskiĭ, Pis'ma Zh. Tekh. Fiz. **19** (20), 69 (1993) [Tech. Phys. Lett. **19**, 663 (1993)].
6. F. A. Chudnovskiĭ, Zh. Tekh. Fiz. **45**, 1561 (1975) [Sov. Phys. Tech. Phys. **20**, 999 (1975)]; A. A. Bugaev, B. P. Zakharchenya, and F. A. Chudnovskiĭ, *The Metal–Semiconductor Phase Transition and Its Applications* (Nauka, Leningrad, 1979).
7. F. A. Chudnovskiĭ, D. O. Kikalov, A. L. Pergament, *et al.*, Phys. Status Solidi A **172**, 391 (1999).
8. K.-D. Ufert, Phys. Status Solidi A **34**, K83 (1976).
9. R. M. Bowman and J. M. Gregg, J. Mater. Sci. **9**, 187 (1998).
10. Sensor Rev., Vol. 19, Issue 1 (1999).

Translated by P. Pozdeev

Technical Physics Letters, Vol. 26, No. 6, 2000, pp. 481–484. Translated from Pis'ma v Zhurnal Tekhnicheskoĭ Fiziki, Vol. 26, No. 11, 2000, pp. 68–74.

Stationary States of a Low-Pressure Inductively Coupled RF Discharge Near the Quenching Threshold

A. V. Zykov and K. I. Polozhiĭ

Kharkov State University, Kharkov, Ukraine

Received November 4, 1999

Abstract—A refined self-consistent volume-averaged model of a low-pressure inductively coupled RF discharge is proposed. It is demonstrated that taking into account finite dimensions of the near-electrode space-charge region leads to a double-valued dependence of the equilibrium electron temperature on the discharge pressure and power. There is a critical power level, dependent on the pressure and working chamber geometry, below which no stationary inductively coupled discharge can exist in the system. The theoretical results show good agreement with experiment. © *2000 MAIK "Nauka/Interperiodica".*

Low-pressure inductively coupled RF (ICRF) discharge, obtained at a working gas pressure such that the mean free path of gas particles exceeds the gas-discharge chamber (GDC) dimensions, is widely employed in vacuum-plasma etching and deposition technologies as an effective source of low-energy ions. Advantages of using ICRF discharge in the ion-plasma etching reactors and ion sources include a high plasma density (up to 10^{12} cm^{-3}), low ion energy scatter ($\Delta\varepsilon_1 \leq$ 5 eV), relatively low working pressures (p = 10^{-4}–10^{-3} Torr), high efficiency (energy lost per ion creation $\eta \sim$ 30–80 eV), the absence of incandescent parts, a large working life with reactive gases, and the possibility of independently controlling the ion energy and density. For these reasons, the number of works devoted to the experimental and theoretical investigation of the nature and features of the low-pressure ICRF discharge has been rapidly increasing in the past years.

Lee *et al.* [1–4] have developed a self-consistent, volume-averaged model describing the stationary states of the ICRF discharge, which made it possible to calculate the plasma parameters, including the electron temperature (T_e), ion (n_i) and electron (n_e) number densities, ion (j_i) and electron (j_e) current densities, discharge impedance, etc., as functions of the external factors (GDC size and geometry, working gas type and pressure, power P absorbed in the RF discharge, etc.). Note that a similar approach to determination of the plasma parameters in the ICRF discharge was previously suggested by Bondarenko *et al.* [5].

The above model assumes that the discharge is bounded by an equipotential surface of GDC (where $j_i = j_e$) and comprises a quasineutral plasma region ($n_e \approx n_i$), characterized by an isotropic Maxwell electron energy distribution function (EEDF) and featuring ionization and excitation of the working gas molecules, and a collisionless near-wall space-charge region ($n_i \gg n_e$) where the main plasma–wall potential drop takes place with an allowance for the simplifications made in the model; the laws of conservation of the number of particles and energy in the integral form for a stationary ICRF discharge can be written as

$$\begin{aligned} n_a \nu^i(T_e) \int_V n_e dV &= v_B \oint_S n_i dS, \\ P &= e\varepsilon_c(T_e) n_a \nu^i(T_e) \int_V n_e dV + e\varepsilon_T(T_e) v_B \oint_S n_i dS, \end{aligned} \tag{1}$$

where the integration is performed over the plasma volume V and surface S. Here, e is the electron charge, ν^i is the frequency of ionizing electron–atom collisions, ε_c are the mean electron energy loss due to inelastic collisions [2], $\varepsilon_T = T_e(2 + 0.5\ln(M_i/m_e))$ is the kinetic energy transferred to the GDC wall by an electron–ion pair (calculated for the Maxwell EEDF), M_i and m_e are the masses of ion and electron, $v_B = (2T_e/M_i)^{1/2}$ is the ion velocity at the plasma–deposit interface corresponding to the Bohm criterion (Bohm velocity).

By averaging of the electron and ion number densities over the plasma volume and surface and using a linear approximation of the ionization cross section as function of the energy [6], equations (1) can be reduced to the following form:

$$\begin{aligned} n_a d &= \frac{\bar{n}_i}{\bar{n}_e} \frac{v_B}{\nu^i}; \\ \nu^i(T_e) &= C_i(U_i + 2T_e)\sqrt{\frac{8T_e}{\pi m_e}} \exp\left(-\frac{U_i}{T_e}\right); \end{aligned} \tag{2}$$

$$P_S = j_i \eta(T_e); \quad \eta = \varepsilon_c + \varepsilon_T; \quad j_i = e\bar{n}_i v_B,$$

where C_i is the constant describing the ionization cross-section, U_i is the ionization potential, $d = V/S$ is the geometric parameter, $\bar{n}_e$ is the electron number density averaged over the volume V, $\bar{n}_i$ is the ion number density averaged over the surface S, $P_S = P/S$ is the specific power, η is the energy lost per ion creation. The set of equations (2) yields a solution for which T_e is independent of P and is uniquely determined by the similarity parameter $n_a d$ or pd ($p = n_a kT_g$, $T_g = 300$ K), by analogy with the well-known result for a glow discharge column [6], while n_e, n_i, and j_i are directly proportional to P at a constant value of pd.

These results, albeit well agreeing with experiment [7, 8] in a broad range of external conditions, cannot explain the quenching of an ICRF discharge upon decrease in the working gas pressure and discharge power. Therefore, it was of interest to develop this model so as to determine the region of existence of the

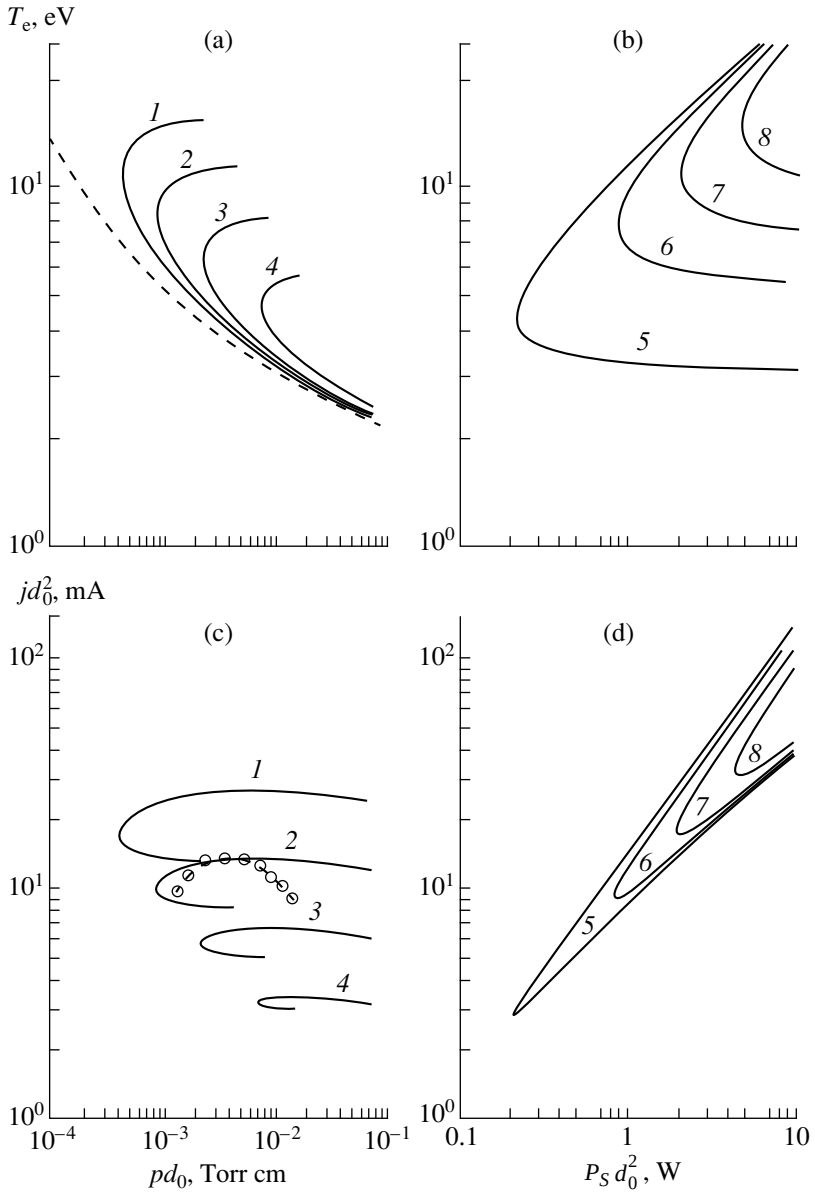

Fig. 1. Numerical solutions of the system of equations (4) for a low-pressure ICRF discharge characteristics T_e and jd_0^2 as functions of the external parameters pd_0 and $P_S d_0^2$: (*1*) 2; (*2*) 1; (*3*) 0.5; (*4*) 0.125 ($P_S d_0^2$, W); (*5*) 10^{-2}; (*6*) 10^{-3}; (*7*) 4×10^{-4}; (*8*) 2×10^{-4} (pd_0, Torr cm). Dashed curves represent the classical behavior in the limit $\xi \equiv 0$. Points in fig. 1c correspond to the experimental data for $P_S d_0^2 = 1$ W.

stationary states of an ICRF discharge at extremely low working gas pressures and small specific powers.

In order to solve this task, it is necessary to refine the meaning of the geometric parameter $d = V/S$ and, accordingly, the similarity parameter pd that uniquely determines the T_e value. For the sake of simplicity and illustration, we will consider a model of infinite flat plasma capacitor with an interelectrode spacing $2d_0$ (the results obtained below are readily generalized to include the case of cylindrical or spherical geometry). At large concentrations of charged particles, the thickness of the near-electrode space-charge region is $h \ll d_0$ and the plasma volume virtually coincides with GDC, while the geometric parameters is $d \approx d_0$. However, in the limiting cases of low pressure and small power (and, hence, small plasma density), the value of h becomes comparable with the interelectrode distance and can no longer be neglected. In these cases, the size d determines a halfwidth of a region in the plasma where $d = d_0 - h$.

According to the model under consideration, the near-wall regions are characterized by $n_i \gg n_e$. An equation relating the plasma parameters to the thickness h is provided by the Child–Langmuir "3/2 law" for a current of positive ions with the initial velocity v_B in a flat layer [6]:

$$h = (9\pi\sqrt{M_i/2e})^{-1/2} \times [(M_i v_B^2/2e + \varphi_{sh})^{3/4} - (M_i v_B^2/2e)^{3/4}] j_i^{-1/2}, \quad (3)$$
$$\varphi_{sh} = \varphi_{pl} - 2T_e,$$

where φ_{sh} is the potential drop in the near-wall region, $\varphi_{pl} = 0.5T_e \ln(M_i/m_e)$ is the plasma–wall potential drop [6], and $2T_e$ is the potential drop across the plasma. Taking into account that $d = d_0(1 - \xi)$, where $\xi = h/d_0$ is a dimensionless layer thickness, we may write equations (2) in the following form:

$$n_a d_0 = \frac{\bar{n}_i}{\bar{n}_e} v_B \frac{1}{\nu^i} \frac{1}{1-\xi}, \quad P_S = j_i \eta(T_e),$$
$$\xi = (9\pi\sqrt{M_i/2e})^{-1/2}[(T_e + \varphi_{sh})^{3/4} - T_e^{3/4}] \sqrt{\frac{\eta(T_e)}{P_S d_0^2}}. \quad (4)$$

Figure 1a illustrates the solutions to equations (4) by a family of T_e versus pd_0 plots for various vales of the parameter $P_S d_0^2$, and Fig. 1b presets a family of T_e versus $P_S d_0^2$ for various pd_0 (working gas, argon; $\bar{n}_e/\bar{n}_i \approx 0.3$; gas constants C_i, U_i taken from [6]; function $\varepsilon_c(T_e)$ taken from [9]). As seen from Fig. 1a, taking into account the size of the near-electrode regions leads to a new, double-valued function $T_e(pd_0)$ determining the threshold values of pressure for the region of existence of the stationary states of plasma at various values of the parameter $P_S d_0^2$. For the comparison, a dashed curve in Fig. 1a shows a solution of system (2) for the $T_e(pd_0)$ in the limiting case of system (4) for $\xi \longrightarrow 0$.

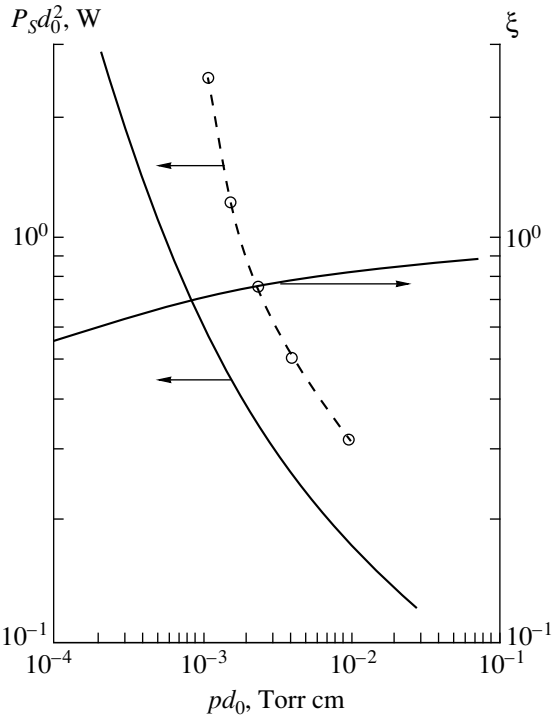

Fig. 2. The plots of critical power (ICRF discharge quenching) and dimensionless layer thickness ξ (for the critical power of discharge quenching) versus gas (argon) pressure. Open circles represent the experimental $P_S d_0^2$ values.

The parameter $P_S d_0^2$, depending both on the power absorbed by the discharge and on the GDC geometry, represents essentially an additional similarity parameter for a low-pressure ICRF discharge. For a fixed GDC size, a decrease in the working gas pressure leads to an increase in the minimum value of $P_S d_0^2$ at which the plasma may occur in a stationary state. Figure 2 shows a plot of $(P_S d_0^2)_{cr}$ versus $(pd_0)_{cr}$. Using equations (4), possessing a universal character, it is possible to calculate the plasma concentration and the charged particle current density for an ICRF discharge in a given GDC and study these values as functions of the external parameters. Figures 1c and 1d present the curves of $j_i d_0^2 (pd_0)$ and $j_i d_0^2 (P_S d_0^2)$.

In order to verify the above theoretical results, we have performed a series of experiments on a vacuum setup with a cylindrical metal GDC (diameter, 250 mm; length, 60 mm) [7] equipped with an ICRF discharge ion source [10] corresponding in the first approximation to a flat capacitor model. The experimental data on the current density and the discharge quenching threshold in this ion source were processed in terms of the

model and are plotted in Figs. 1c and 2. As seen, the theory and experiment exhibit good qualitative agreement near the ICRF discharge quenching threshold for $pd_0 < 10^{-2}$ Torr cm. According to our estimates, the overstated (by a factor of 2–3) threshold values of $(P_S d_0^2)_{cr}$ are related to considerable (tens to hundreds of Watts) resistive losses of power in the inductor and in the generator coupling device and to the RF induced heating of GDC elements (which is especially pronounced, as noted in [11], in the region of low gas pressures where the inductor potential reaches several kV). For the more precise measurements, special calibration investigations of the RF circuit have to be performed according to the methods described in [11]. Note also that the experimental system employed did not reveal a high-temperature branch of equilibrium plasma states predicted by the theory.

Thus, the further investigations require both the experimental approach to be improved and the ICRF discharge model to be refined by introducing corrections for the boundary conditions, realistic EEDF [8], and the energy dependence of the inelastic interaction cross sections.

REFERENCES

1. C. Lee, D. B. Graves, M. A. Lieberman, and D. W. Hess, J. Electrochem. Soc. **141**, 1546 (1994).
2. C. Lee and M. A. Lieberman, J. Vac. Sci. Technol. A **13**, 368 (1995).
3. M. A. Lieberman and R. A. Gottscho, in *Physics of Thin Films,* Ed. by M. Francombe and J. Vossen (Academic Press, New York, 1994), Vol. 18.
4. J. T. Gudmundson and M. A. Lieberman, Plasma Sources Sci. Technol. **7**, 83 (1998).
5. V. G. Bondarenko, V. P. Denisov, B. G. Eremin, *et al.*, Fiz. Plazmy **17**, 756 (1991) [Sov. J. Plasma Phys. **17**, 442 (1991)].
6. Yu. P. Raĭzer, *The Physics of Gas Discharge* (Nauka, Moscow, 1987).
7. S. V. Dudin, A. V. Zykov, K. I. Polozhiĭ, and V. I. Farenik, Pis'ma Zh. Tekh. Fiz. **24** (22), 58 (1998) [Tech. Phys. Lett. **24**, 881 (1998)].
8. V. A. Godyak, R. B. Piejak, and B. M. Alexandrovich, Plasma Sources Sci. Technol. **4**, 332 (1995).
9. M. A. Lieberman and S. Ashida, Plasma Sources Sci. Technol. **5**, 145 (1996).
10. A. M. Budyanskiĭ, A. V. Zykov, and V. I. Farenik, *High-Frequency Ion Source*, Ukrainian Patent No. 2426; RF Patent No. 1570549 (28 June 1993).
11. K. Suzuki *et al.*, Plasma Sources Sci. Technol. **7**, 13 (1998).

Translated by P. Pozdeev

Technical Physics Letters, Vol. 26, No. 6, 2000, pp. 485–487. Translated from Pis'ma v Zhurnal Tekhnicheskoĭ Fiziki, Vol. 26, No. 11, 2000, pp. 75–79.

Electric Field Induced Anomalous Relaxation in a Liquid Not Contacting with Potential Electrodes

N. N. Krasikov and O. V. Shuvaeva

Kovrov State Technological Academy, Kovrov, Russia

Received January 31, 2000

Abstract—It is experimentally demonstrated that a contactless exposure of alcohols to a high-strength electric field gives rise to an optical anisotropy varying with time both during the exposure and upon switching off the electric field. The effect is related to a field-induced structurization of the liquid and the formation of quasielectret layers with anomalous relaxation properties. *© 2000 MAIK "Nauka/Interperiodica".*

Anomalous physical phenomena are usually observed in structurizable media capable of storing energy and possessing spatially inhomogeneous physical properties [1]. An interesting phenomenon of this type, related to the accumulation of electric energy, is the behavior of liquids during contactless exposure to an electric field of high strength (when the electric current is small and caused entirely by leakage conductivity).

We have studied the effect of electric field on the properties of liquid media. The field was generated by a source of dc voltage U = 15–20 kV. The upper electrode was separated from the liquid by an air gap, while the lower electrode was separated from liquid by the cell bottom [2]. The insulating transparent cell with a sample of liquid was placed into a KFK-2 photoelectrocolorimeter. The optical scheme of the instrument was modified by installing an additional polaroid for the light beam at the output of the illuminator channel. The sensitivity was improved by using a Shch-300 millivoltmeter and taking all the measures necessary to exclude the electric breakdown and eliminate leakage currents. The optical absorption was determined as percentage of the value corresponding to a neutral state (with the field switched off). The system response was measured either upon switching on the high-voltage source or immediately after switching off the field.

Figure 1 shows the results of experiments with aqueous glycerol solutions. The duration of exposure to the electric field was 5 min. During this period of time, the optical transmission coefficient η virtually attains a plateau (saturation); after switching off the field, η gradually restores 100% of the initial level observed in the liquid before exposure. The η value exhibited no variations in pure (doubly distilled) water and varied only slightly in chemically pure glycerol. Similar results were obtained for the monoatomic alcohols not reported in this work.

The experimental results are indicative of the anisotropy, which arises in the alcohol studied and its aqueous solutions upon exposure to the field and varies after switching off the applied voltage, showing anomalous relaxation behavior over a time period of several minutes. The anomalous relaxation deviates from the Maxwell relaxation $\tau_0 = \varepsilon\varepsilon_0/\gamma$ reflecting microscopic polarization processes depending on γ and ε–conductivity and permittivity of the medium, respectively (ε_0 is the dielectric constant). The anomalous relaxation behavior is apparently caused by the microscopic process of space-charge polarization, whereby the charge carriers and dipole molecules are initially linked together into associates and clusters. A directed motion in the electric field must be preceded by the detachment of charge carriers from these formations characterized by the binding energy U. Then, the relaxation time τ is evaluated by Frenkel [3]: $\tau = \tau_0 \exp(U/kT)$, where k is the

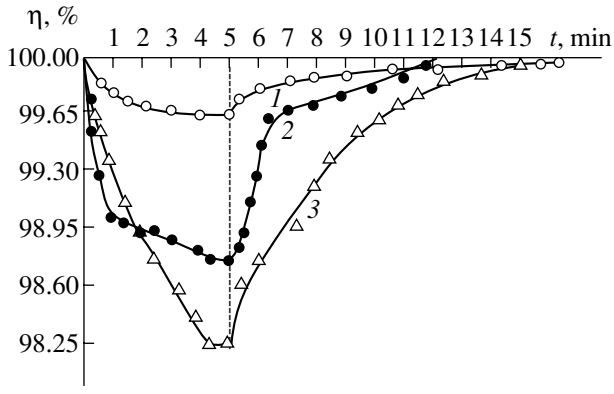

Fig. 1. Time variation of the transmission coefficient η of a polarized light with λ = 750 nm upon switching on (t = 0) and off (t = 5 min) a high voltage applied to (*1*) pure glycerol (reagent grade) and aqueous glycerol solutions containing (*2*) 25 and (*3*) 50 vol % H_2O.

1063-7850/00/2606-0485$20.00 © 2000 MAIK "Nauka/Interperiodica"

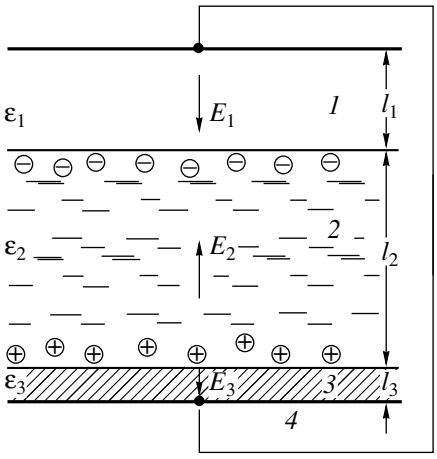

Fig. 2. Schematic diagram of a three-layer capacitor modeling the residual polarization of liquid: (*1*) air gap; (*2*) liquid; (*3*) insulating layer; (*4*) potential electrode.

Boltzmann constant and T is the temperature of the medium.

Previously [4], a similar variation of the potential difference across a liquid upon switching the field on and off was observed with the aid of an electric probe oriented in the field direction. However, this method cannot reliably characterize the true relaxation time because the results depend on the input resistance of the measuring instrument and its amplifier scheme.

We have observed a difference between the relaxation processes accompanying the field action and afteraction, the relaxation time constant τ being usually greater in the latter process than in the former. This difference is evidence that the electric field favors the formation of new stable structures in the liquid studied, possessing electret properties and having large U values [5]. The oppositely charged quasielectret layers of heterocharges can form in the surface layers of liquids acquiring an ordered structure under the action of electrostatic forces and hydrogen bonds [6].

Let us consider features of the formation of these quasielectret layers in the system studied. Switching on the electric field leads to deformation and orientation polarizations in the medium, which are virtually instantaneously set on the experimental time scale. This is followed by the space-charge polarization [7] characterized by an anomalous relaxation time of the order of seconds or minutes. Although the process of the quasielectret layer formation may involve several stages (withdrawal of charge carriers from potential wells, directed charge transfer, near-surface layer formation), the possible stages cannot be resolved on the integral pattern of variation of the optical response signal (Fig. 1). The resulting quasielectret field may compensate for the initial field determined by the surface charge density σ and permittivity of the liquid ε_2 ($E_2 = \sigma/\varepsilon_2\varepsilon_0$). We will assume that the limiting quasielectret layers compensate for the applied field in both magnitude and direction.

This system can be modeled by a three-layer capacitor comprising an air gap l_1, a liquid layer l_2, and an insulating layer (glass) l_3 the corresponding permittivities ε_1, ε_2, ε_3 and the electric field strengths E_1, E_2, E_3 (Fig. 2). Our task reduces to evaluating the field strength E_2 in a liquid with quasielectret layers.

Applying the Gauss theorem and the second Kirchhoff law to the interfaces between layers [7] in a model system with short-circuited electrodes, we obtain the following system of equations:

$$\begin{aligned} \varepsilon_1 E_1 &= -\varepsilon_2 E_2 + \frac{\sigma}{\varepsilon_2 \varepsilon_a}, \\ \varepsilon_3 E_3 &= -\varepsilon_2 E_2 + \frac{\sigma}{\varepsilon_2 \varepsilon_a}, \\ -E_1 l_1 + E_2 l_2 - E_3 l_3 &= 0. \end{aligned} \tag{1}$$

Upon solving this system, we obtain the residual field strength E_2 in a liquid with quasielectret layers:

$$E_2 = \frac{\sigma}{\varepsilon_2 \varepsilon_0} \frac{\dfrac{l_1}{\varepsilon_1} + \dfrac{l_3}{\varepsilon_3}}{l_2 + \dfrac{\varepsilon_2}{\varepsilon_1} l_1 + \dfrac{\varepsilon_2}{\varepsilon_3} l_3}. \tag{2}$$

In the system studied in our experiments, this field strength may amount to the value $E_2 \approx 4.5 \times 10^3$ V/m characteristic of the moment of switching off the applied field. The residual field decays in the process of anomalous relaxation (see the right-hand branch in Fig. 1 for $t > 5$ min), depending on the conductivity of liquid and on the charge carrier binding energy in the quasielectret layers determining anisotropy of the system.

Apparently, the E_2 value characterizes relaxation of the polarized light intensity in the liquid before and after application of the high voltage. The afteraction results in restoration of the initial equilibrium state of 100% light transmission characteristic of the isotropic liquid.

Thus, a high-strength electric field acting upon a liquid not contacting with the potential electrodes favors structurization in the liquid composed of asymmetric (in particular, polar) molecules. The electric field energy concentrates in the layers possessing residual space-charge polarization typical of the electret state of the substance, which is confirmed by the results of

measurements of the intensity of transmitted linearly polarized light.

REFERENCES

1. G. E. Skvortsov, Pis'ma Zh. Tekh. Fiz. **25** (7), 57 (1999) [Tech. Phys. Lett. **25**, 274 (1999)].
2. N. N. Krasikov, Élektrotekhnika **4**, 57 (1996); N. N. Krasikov, Pis'ma Zh. Tekh. Fiz. (in press) [Tech. Phys. Lett. (in press)].
3. Ya. I. Frenkel', *Kinetic Theory of Fluids* (Nauka, Moscow, 1974).
4. N. N. Krasikov, Biofizika **43**, 989 (1998).
5. A. N. Gubkin, *Electrets* (Nauka, Moscow, 1978).
6. V. Ya. Antonchenko, A. S. Davydov, and V. V. Il'in, *Principles of the Physics of Water* (Naukova Dumka, Kiev, 1991).
7. K. M. Polivanov, *Theory of Electromagnetic Field* (Énergiya, Moscow, 1969).

Translated by P. Pozdeev

Technical Physics Letters, Vol. 26, No. 6, 2000, pp. 488–489. Translated from Pis'ma v Zhurnal Tekhnicheskoĭ Fiziki, Vol. 26, No. 11, 2000, pp. 80–83.

Two-Channel Helical Arc Formation between Graphite Electrodes at a Reduced Pressure

V. D. Shimanovich, I. P. Smyaglikov, A. I. Zolotovskiĭ, S. M. Pankovets, N. I. Chubrik, and S. V. Goncharik

Institute of Molecular and Atomic Physics, Belarussian Academy of Sciences, Minsk, 220072 Belarus

Received December 30, 1999

Abstract—Experiments showed that an electric arc in helium between graphite electrodes (I = 60–120 A; L = 3–6 mm; P_{He} = 1–500 Torr) may exist in two different spatial-temporal modes: (i) a stationary mode with axisymmetric current channel and (ii) a nonstationary mode with two helical channels emerging from an anode spot and rotating at 10–20 kHz around the side surfaces of cylindrical electrodes. © *2000 MAIK "Nauka/Interperiodica".*

Our investigations of the process of fullerene synthesis [1] showed that an arc discharge generated in a buffer gas at low pressure may exist in two modes spontaneously switching irrespective of the discharge parameters. The first mode represented a stationary axisymmetric arc and the second appeared as a nonstationary plasma column with periodic brightness pulsations. The ratio of times of discharge operation in two modes, as well as the structure and frequency of pulsations in the nonstationary stage, depended on the buffer gas type and pressure P and the arc current I. At P_{He} = 100 Torr, the arc occurs for approximately equal time in both modes, while at a pressure below a few Torr only the nonstationary mode exists. It was suggested [1] that the nonstationary mode formation may be related to an overheating instability in the gas phase.

In order to elucidate the structure of the nonstationary arc mode, we have investigated the arc in a wide range of discharge parameters using the method of high-speed photography in a shot-by-shot mode and in a continuous scan mode, whereby the arc image in various cross sections was monitored at a time resolution of up to 10^{-6} s.

Figure 1 shows a sequence of arc images (I = 80 A; P_{He} = 10 Torr) obtained at a frequency of 50 pictures/s and an exposure time of 10^{-6} s (these conditions excluded distortion of the arc image as a result of instability) [1]. As seen, the arc channel is curved and continuously changes its orientation in space. In addition, the arc images indicate that no any longitudinal motion of bright objects takes place in the discharge gap.

An analysis of the instantaneous arc images (Fig. 1) and their variation in the longitudinal and transverse sweep mode (Figs. 2a and 2b) showed that the arc formed under the indicated conditions comprises two helical channels rotating around the side surfaces of cylindrical electrodes. The differential brightness of channels observed in the longitudinal sweep is probably explained by attenuation of the channel remote from the point of observation as a result of light absorption and scattering in the central region of the arc.

Figure 2 shows a schematic diagram of the rotating arc (central inset) and the continuous sweep patterns obtained by method of computer simulation (Figs. 2c and 2d), corresponding to the experimental observations. The principal agreement between experiment and calculations indicates that the proposed model can be used to describe the behavior of rotating arc in the range of discharge parameters studied.

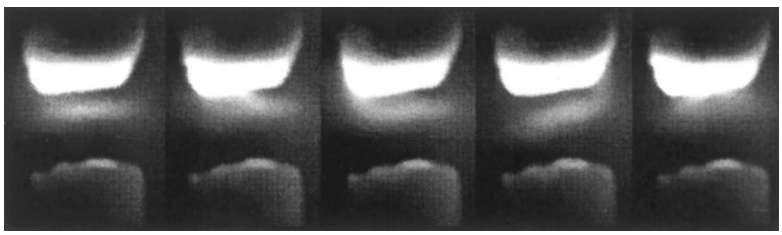

Fig. 1. Sequential photographs of the arc (I = 80 A; P_{He} = 10 Torr) obtained at a frequency of 50 pictures/s and an exposure time of 10^{-6} s.

1063-7850/00/2606-0488$20.00 © 2000 MAIK "Nauka/Interperiodica"

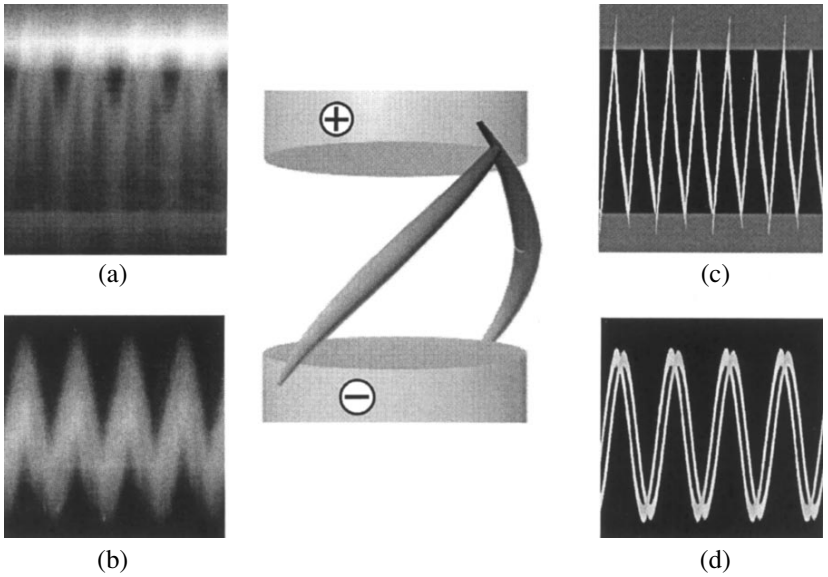

Fig. 2. A model of two-channel helical rotating arc formed between graphite electrodes at a reduced pressure (central inset) and the continuous sweep images of the (a, c) longitudinal and (b, d) transverse cross sections of the arc.

A nonstationary character of the arc can be explained by competition of the physical processes involved in the supply of vapors and carbon from anode to discharge gap and their removal from the discharge zone. A decrease in the gas pressure may give rise to overheating instability in the arc plasma with distributed anode localization because of insufficient heat removal from the arc. Under certain discharge conditions, this leads to a rapid (~10^{-5} s) transformation of the arc from stationary to nonstationary mode with the formation of electrode spots and contracted current channels. These spots and channels are pushed by the magnetic field to the side surface of cylindrical electrodes and rotate around the system axis.

Stability of a helical channel rotating at high speed increases upon its splitting into two symmetric helical columns emerged from a common anode spot. The formation of two current channels increasing stability of a plasma formation was previously reported in [2].

The appearance of the anode spot results in increasing erosion and growing partial pressure of carbon in the discharge gap. This, in turn, facilitates heat removal from the discharge plasma by way of both radiative and convective thermal conductivity. As a result, the overheating instability decays and the stationary axisymmetric arc mode restores. The transition from stationary to nonstationary mode and back is repeated during the entire lifetime of the arc discharge.

The above pattern is indirectly confirmed by the observed dependence of the arc structure on the buffer gas pressure. Indeed, only the two-channel rotating helical arc exists in the system at a gas pressure below a few Torr. This fact indicates that the energy removed from the discharge plasma at such a low pressure is insufficient to suppress the overheating instability. A decrease in the radiative and convective thermal conductivity with decreasing gas pressure is consistent with the commonly accepted notions about transfer processes in gases and plasmas.

We believe that an investigation of a relationship between the regions of fullerene formation in an arc-discharge reactor and the alternating axisymmetric and rotating helical arc modes may provide important information on the mechanisms of formation of the third allotropic state of carbon.

The authors are grateful to G.A. Dyuzhev for fruitful discussions.

This work was supported by the Belarus Republic Foundation for Basic Research, project no. F96-261.

REFERENCES

1. V. D. Shimanovich, I. P. Smyaglikov, and A. I. Zolotovskiĭ, Inzh.-Fiz. Zh. **71**, 669 (1998).
2. V. V. Azharonok, V. A. Gubkevich, A. I. Zolotovskiĭ, *et al.*, Inzh.-Fiz. Zh. **50**, 669 (1986).

Translated by P. Pozdeev

Technical Physics Letters, Vol. 26, No. 6, 2000, pp. 490–492. Translated from Pis'ma v Zhurnal Tekhnicheskoĭ Fiziki, Vol. 26, No. 11, 2000, pp. 84–89.

Laser-Induced Graphite Superhardness and Transformation into Amorphous Carbon in a Near-Surface Layer of Cast Iron

G. I. Kozlov

Institute for Problems of Mechanics, Russian Academy of Sciences, Moscow, 117526 Russia

Received January 21, 2000

Abstract—An analysis of the microstructure and Raman spectra shows that the formation of superhard structures in a near-surface layer of cast iron, observed upon a special laser treatment of the gray iron surface covered by a thin layer of inductor (copper), is related to the transformation of graphite (present in the cast iron) into amorphous carbon. A possible mechanism of this process is proposed, which includes the stages of graphite transition into a liquid phase, supercooling of the liquid carbon, and its transformation into a condensed amorphous phase. *© 2000 MAIK "Nauka/Interperiodica".*

In the previous work [1], we demonstrated an interesting phenomenon of the induced formation of superhard structures in cast iron upon laser processing of the gray iron surface covered by a thin layer of an inductor (copper).

The induction phenomenon consists in a control action of the inductor crystal structure on the development of laser-induced phase transformations in the near-surface layers of metals and alloys contacting with the inductor in the course of their cooling. We have demonstrated [1] that the induction effect of copper on gray iron leads, first, to a substantial saturation of the surface layer of cast iron with carbon and, second, to the austenite stabilization. The latter results in a significant decrease of the austenite transformation temperature and, due to this, in a substantial grain size reduction in the structures (including carbides and pearlite) formed in the course of the cast iron cooling, an analysis of the phase composition did not allow us to determine the main structural components responsible for the high microhardness. However, this analysis showed the formation of martensite in small amounts insufficient for the laser-induced hardening of the gray iron surface covered by an inductor. The only "prompt" enabling us to explain high values of the microhardness was provided by the results of the microstructure analysis, which revealed the presence of a significant amount of carbon in a globular form in the zone of melting.

In this work, we made an attempt at determining whether these carbon inclusions can be classified as graphite or represent some other carbon structure. For this purpose, we measured and analyzed the Raman spectra of carbon inclusions from the zone of laser action at the first step (i.e., from a depth of 0.5 mm) [1]. Figure 1 compares the Raman spectrum of inclusions with the spectra of pyrographite and diamond [2]. The latter spectra exhibit characteristic narrow peaks at 1580 and 1332 cm^{-1}, respectively.

Note that the Raman spectrum of the globular carbon inclusions exhibits a characteristic two-hump band that occupies virtually the entire spectral range from pyrographite to diamond. This can be considered as evidence of a significant disordering of the graphite structure in a near-surface layer of cast iron resulting from laser processing of a gray iron surface covered by a thin layer of copper. This disordering leads to an almost complete loss of a long-range order typical of ordered crystalline structures, size reduction, and randomization of the molecular structures of carbon, that is, to the amorphization of carbon. Judging by the width of the Raman peaks, the carbon particle size is as small as 50–80 nm, which is typical of nanocarbon.

It is interesting to compare the Raman spectrum of these carbon inclusions with the Raman spectrum of amorphous carbon synthesized from hydrocarbons by, for example, CVD method [3] (Figs. 1c and 1d). It is amazing, but the spectra of these two carbon structures formed under absolutely different conditions appear to be almost identical, which proves our assumption that the globular carbon formed by laser processing of gray iron with a thin layer of inductor (copper) deposited on its surface is essentially an amorphous carbon (glass-carbon).

A question naturally arises as to what is the mechanism of graphite transformation into amorphous carbon under laser irradiation of the cast iron surface covered by a copper layer? Note, first of all, that graphite present in the cast iron and phase-separated in the course of crystallization from melt grows from one center and branches in various directions to form a flaky structure with strongly curved lobes. For this reason, a microsection of the cast iron (Fig. 2a) exhibits linear

1063-7850/00/2606-0490$20.00 © 2000 MAIK "Nauka/Interperiodica"

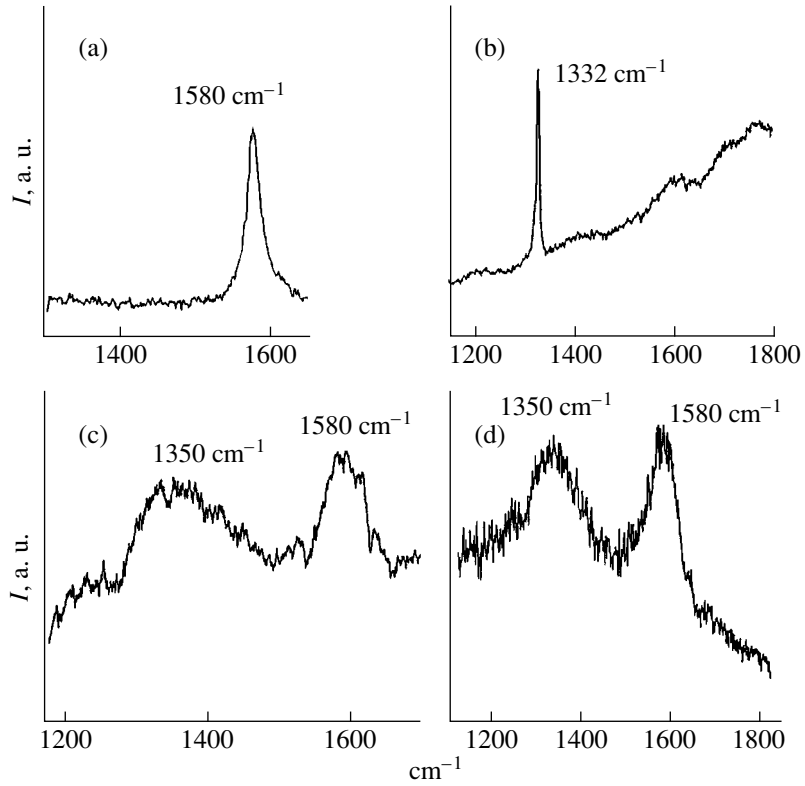

Fig. 1. Raman spectra of (a) pyrographite, (b) polycrystalline diamond film, (c) carbon inclusions in the zone of laser action, and (d) amorphous carbon.

and curved graphite plate lets corresponding to various cross sections of the graphite flakes.

Figure 2b shows that significant changes of the carbon structure take place in a near-surface layer of cast iron upon the laser treatment of its surface. It is seen that the laser action leads to transformation of the initial carbon plate lets of various shapes into globules, some of these possessing an almost perfect spherical shape. This process can take pace in a near-surface layer of cast iron, provided that carbon occurs in a liquid state at a certain time moment after the laser action. This assumption, based on the analysis of the cast iron microstructure after the laser action, explains both the coalescence of carbon into drops (globules) and the subsequent formation of amorphous carbon. The latter can be considered as a result of transition of a strongly overcooled liquid phase into a condensed state. It is known that fast cooling of some melts is accompanied by the formation of an amorphous condensed state rather than of an ordered crystal lattice.

However, it is likely that, under the conditions of laser treatment, the liquid phase of carbon can form and exist only under high pressure. That is why a question arises if there is a basic possibility of realization of high pressures in our experiments.

The calculation of thermal and phase stresses in a near-surface layer caused by laser irradiation of the surface of cast iron covered by a copper layer is a complex

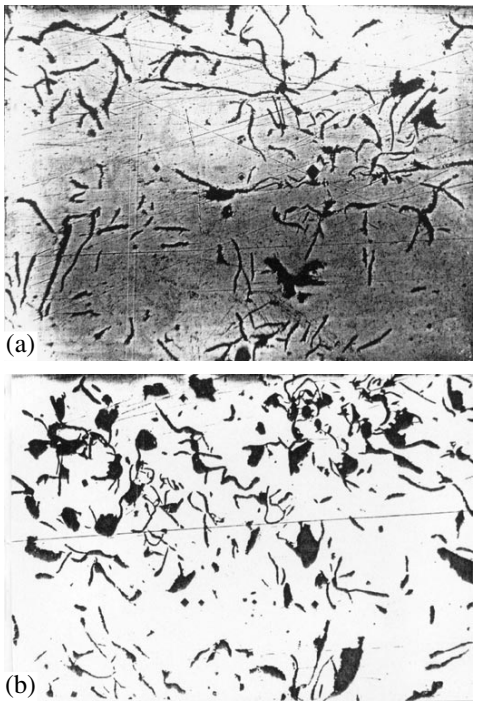

Fig. 2. Photographs of gray iron microstructure (magnification, ×80) showing (a) the structure of graphite plates in the microsection plane prior to laser treatment and (b) the structure of amorphous carbon in a near-surface layer of cast iron after the laser irradiation.

problem that needs special consideration. Analysis of the existing data and estimates of the possible stresses within the framework of a simplified one-dimensional model indicated that the laser action and the subsequent crystallization of cast iron and copper from melt in the course of cooling can cause stresses amounting to 4×10^8 Pa due to a substantial difference of the thermal coefficients of linear expansion. Such high stresses can facilitate the transition of graphite into liquid carbon.

Thus, the mechanism of amorphous carbon formation in a near-surface layer of cast iron upon laser irradiation of the surface covered by copper is probably related to several interesting processes, in particular, the development of significant thermal stresses in the course of laser action and subsequent cooling of cast iron and copper and the transformation of graphite into the liquid state followed by overcooling of liquid carbon and its transformation into an amorphous state.

Note finally the general character of the described phenomena. Laser action on various combinations of metals and alloys makes it possible to realize extremal conditions allowing one to control phase transformations. This method can be used for directed modification of a material surface aimed at improving its physicomechanical characteristics and for the creation of novel materials exhibiting unique properties.

The author is grateful to Prof. V. I. Konov and I. Vlasov for fruitful discussions and assistance.

REFERENCES

1. G. I. Kozlov, Pis'ma Zh. Tekh. Fiz. **26** (24), 61 (1999) [Tech. Phys. Lett. **25**, 997 (1999)].
2. V. I. Konov and S. A. Uglov, Kvantovaya Élektron. (Moscow) **25**, 291 (1998).
3. K. J. Hüttinger, Chem. Vap. Deposition **4**, 151 (1998).

Translated by A. Chikishev

Technical Physics Letters, Vol. 26, No. 6, 2000, pp. 493–495. Translated from Pis'ma v Zhurnal Tekhnicheskoĭ Fiziki, Vol. 26, No. 11, 2000, pp. 90–95.

Structural Features and Energy of Small Water Clusters

S. V. Drozdov and A. A. Vostrikov

Institute of Thermal Physics, Siberian Division, Russian Academy of Sciences, Novosibirsk, 630090 Russia

Received January 31, 2000

Abstract—Collisions between water clusters $(H_2O)_n$, $n = 27$, with relative velocities $V = 1$, 3, or 10 km/s and various initial temperatures, were studied by the molecular dynamics method within the framework of a polarization model. It was found that the clusters may either stick together (at $V = 1$ km/s), break into fragments ($V = 3$ km/s), or form compressed (excited) molecules ($V = 10$ km/s) dissociating into H^+ and OH^-. Inside the cluster, the charge is transferred by the H^+ hopping mechanism. Upon fragmentation, the clusters separate into $H^+(H_2O)_i$ and $OH^-(H_2O)_j$ ions. © *2000 MAIK "Nauka/Interperiodica".*

Processes involved in the collisions between weakly bound molecular clusters play an important role in the gas dynamics and the physics of atmosphere. Our interest in studying these collisions was inspired by the experiments [1–5] which revealed the phenomenon of polar dissociation of the H_2O molecules into H^+ and OH^- in $(H_2O)_n$ clusters, followed by the spatial separation of charges upon collision of these $(H_2O)_n$ clusters with solid surfaces. Note that the polar fragmentation of clusters composed of polar molecules can be a channel of charged particle production in the atmosphere, an important factor in the gaso- and aerodynamic investigations, and a possible reason of the aircraft sensor electrization [6].

Unfortunately, the kinetics of intracluster polar dissociation cannot be studied in a direct laboratory experiment because the characteristic time of this process is of the order of a period of intramolecular vibrations. In order to solve the problem, we have employed the method of molecular dynamics (MD), formed $(H_2O)_{27}$ clusters, and studied collisions between these clusters moving with a relative velocity of $V = 1$, 3, or 10 km/s. The results of the MD simulations revealed significantly nonequilibrium character of the excitation of water molecules in clusters. At $V = 10$ km/s, this excitation led to a polar dissociation of H_2O molecules with charge separation inside the clusters. The calculated probability of separation into ions is small, which is explained by the small size of clusters. In experiment, the probability of separation for a water cluster with $n = 300$ was estimated at $\sim 10^{-7}$ [2]. In model calculations, a significant increase in n is hardly possible, since a rather complicated character of the model of water molecule leads to a nonlinear ($\sim n^3$) increase in the computation time.

Computation model. It was necessary to select a model of water molecule so as to provide for the possibility of studying the polar dissociation of H_2O. For this reason, we have employed a polarization model of Stillinger and Davis [7, 8]. According to the model adopted, the H_2O molecule consists of two protons (H^+) and a negatively charged oxygen ion (O^{2-}) possessing a scalar polarizability. The total interaction potential comprises a sum of two terms. The first term is additive and represents a sum of pairwise interaction potentials for each pair of atoms in the system. These are the central potentials, their particular forms depending on the interacting atoms. At large interatomic distances, these functions behave like usual Coulomb potentials of interaction between charged particles. At small spacings, the character of interaction dramatically changes. The second term represents a nonadditive potential taking into account a polarization energy related to the dipole moments induced in oxygen atoms in the field of other charges and dipoles in the $(H_2O)_n$ cluster. The motions of atoms were modeled by numerically integrating the system of Newton equations. The integration time step was 0.1 fs, which is markedly smaller compared to the period of atomic vibrations in H_2O. All calculations were performed without truncation of the potentials.

The collisions were modeled by setting the initial directions of motion of the whole cluster, whereby the same velocity vectors were added to all atoms. The velocity vectors of colliding clusters were parallel and oppositely directed. The calculations were performed in the clusters center-of-mass frame of reference. Because of a significantly nonequilibrium character of processes involved in the collision, the cluster temperature T was calculated as a measure of the kinetic energy taking into account only the internal (rotational and vibrational) degrees of freedom of each molecule.

In order to describe the formation of $H^+(H_2O)_i$ and $OH^-(H_2O)_j$ ions in the clusters, we have employed a "geometric" criterion. According to this, the "molecular" bond between H^+ and O^{2-} was considered as broken if the distance between proton and oxygen exceeded 1.3 Å. On display, this was clearly manifested

1063-7850/00/2606-0493$20.00

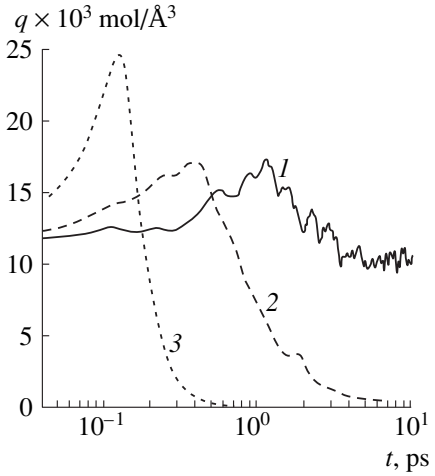

Fig. 1. Time variation of the number density of molecules in water clusters colliding at T = 100 K with various relative velocities V = 1 (*1*); 3 (*2*); 10 km/s (*3*).

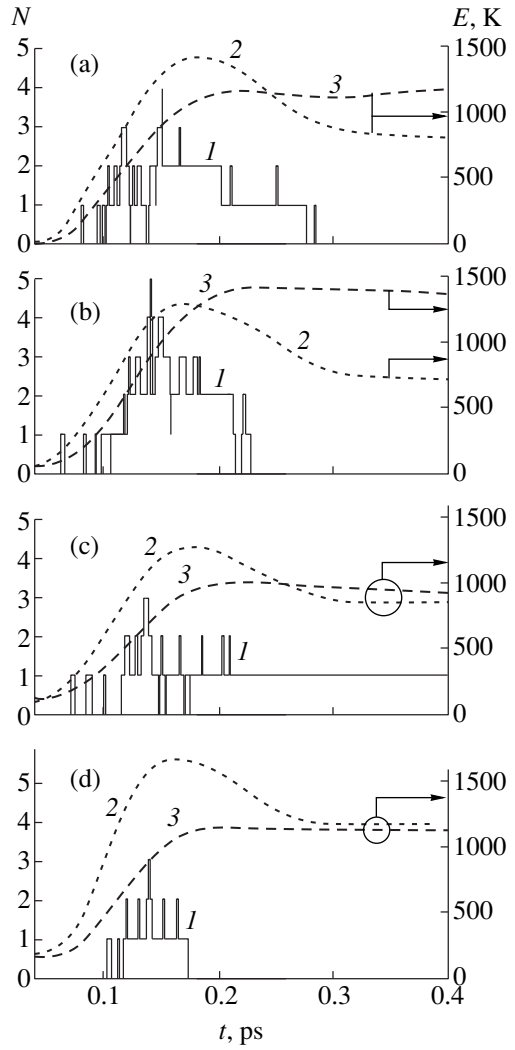

Fig. 2. Time variation of (*1*) the number of ion pairs N, (*2*) the rotational energy, and (*3*) the vibrational energy of molecules in water clusters colliding at a relative velocity of V = 10 km/s and various temperatures T = 20 (a); 70 (b); 130 (c); 200 K (d).

by the proton and oxygen no longer belonging to the same molecule: the proton, spaced by a considerable distance from the "mother" oxygen and could be "trapped" by a different oxygen atom.

Calculation results. The collisions between $(H_2O)_{27}$ clusters were simulated under the following conditions: temperature T = 20, 70, 100, 130, and 200°C; relative velocity V = 1, 3, and 10 km/s.

Figure 1 shows the plots of the number density of molecules q in the system of colliding clusters versus the time upon collision t for various relative velocities. As seen, q attains a constant level for $t > 4$ ps in the system of clusters colliding at V = 1 km/s, which indicates that the two clusters merged together to form a common system. Note that the time of attaining the level q = const was longer as compared to that required for fragmentation of the clusters colliding at V = 3 or 10 km/s. This implies that the fragmentation takes place before the collision energy would be distributed among all molecules in the system.

The formation of charged particles was observed only for V = 10 km/s. It should be noted that the kinetic energy of clusters colliding at V = 10 km/s is 2.33 eV per molecule, which is approximately 1/7 of the energy of polar dissociation of the isolated H_2O molecule (~17 eV), but about four times the threshold energy of the polar dissociation (autoprotolysis) in water (0.58 eV—a significant decrease in the energy of polar dissociation in water is explained by solvation of the H^+ and OH^- ions [9]).

Figure 2 shows the time variation of the number of ion pairs N and the rotational vibrational energy of molecules in water clusters colliding at a relative velocity V = 10 km/s. As seen, despite the continuous (classical) energy distribution over the vibrational degrees of freedom in the model adopted, the collision process exhibits a nonequilibrium character. The internal degrees of freedom have different relaxation times. The maximum number of ion pairs is observed for t = 0.11–0.13 ps, while their lifetime is maximum at T = 130 K.

On display, the pattern of ion pair formation was as follows. At the time instant of maximum compression, compressed (excited) groups of molecules appeared with the OH bond lengths below 1.3 Å. In these molecules, the OH bonds exhibited breakage with the formation of H^+ and OH^- ions. The proton could rapidly move to the other part of the cluster. The cluster fragmentation resulted in separation of the molecular groups containing H^+ and OH^-. After a certain period of time, the oppositely charged ions approached each other due to the Coulomb attraction and recombined. Note that electric fields and charges always present in real systems may hinder the recombination of H^+ and OH^-.

Since the formation of H^+ and OH^- ions, their solvation, cluster fragmentation, and charge recombination proceed within comparable tie intervals, the cluster size

affects not only the kinetic energy of collision, but the probability of the solvated shell formation and the degree of fragmentation as well. It was naturally suggested that the ion pair formation in colliding clusters of greater size would begin at lower relative velocities *V*. This assumption was confirmed by the results of our calculations of the collision of $(H_2O)_{64}$ with a solid surface [10].

This work was supported by the Russian Foundation for Basic Research (project nos. 98-02-17804 and 98-02-17845).

REFERENCES

1. A. A. Vostrikov, D. Yu. Dubov, and M. R. Predtechenskiy, Chem. Phys. Lett. **139**, 124 (1987).
2. A. A. Vostrikov and D. Yu. Dubov, Z. Phys. D **20**, 61 (1991).
3. A. A. Vostrikov and D. Yu. Dubov, Pis'ma Zh. Tekh. Fiz. **16** (1), 61 (1990) [Sov. Tech. Phys. Lett. **16**, 27 (1990)].
4. P. U. Andersson and J. B. C. Petterson, J. Phys. Chem. B **102**, 7428 (1998).
5. C. R. Gebhardt, Schroder, and K.-L. Kompa, Nature **400**, 544 (1999).
6. A. M. Zadorozhny, A. A. Vostrikov, *et al.*, Geophys. Res. Lett. **24**, 841 (1997).
7. F. H. Stillinger and C. W. David, J. Chem. Phys. **69**, 1473 (1978).
8. F. H. Stillinger, J. Chem. Phys. **71**, 1647 (1979).
9. B. Knight, D. M. Goodall, and R. C. Greenhow, J. Chem. Soc., Faraday Trans. **75**, 841 (1975).
10. A. A. Vostrikov *et al.*, Z. Phys. D **40**, 542 (1997).

Translated by P. Pozdeev

Technical Physics Letters, Vol. 26, No. 6, 2000, pp. 496–498. Translated from Pis'ma v Zhurnal Tekhnicheskoĭ Fiziki, Vol. 26, No. 12, 2000, pp. 1–7.

Transformation of GR1 Defects in Annealed Natural Type IIa Diamonds

A. G. Alekseev, V. N. Amosov, A. V. Krasil'nikov, S. N. Tugarinov, V. V. Frunze, and A. Yu. Tsutskikh

Troitsk Institute for Innovation and Thermonuclear Research, Troitsk, Moscow oblast, 142092 Russia

Received December 28, 1999

Abstract—A sample of the natural type IIa diamond was pre-irradiated in a nuclear reactor and then annealed under isothermal conditions at 550°C. The experimental data were used to calculate a decrease in concentration of the neutral vacancy defect called GR1, corresponding to a phononless band (PLB) at 741 nm, and an increase in concentration of the derivative defect H3 with PLB at 503.2 nm for a broad range of annealing times (0–300 h) and temperatures (100–900°C). Calculations performed using a single activation energy E_m = 2.43 eV for both fast and slow components of the GR1 defect transformation process indicate that the annealing of GR1 and the production of H3 are really observable above 450°C (400°C being the threshold temperature). At 700–900°C, the fast component contributes over the annealing time interval 0.002–0.251 h, after which the annealing of GR1 is determined by the slow component alone. *© 2000 MAIK "Nauka/Interperiodica".*

The purpose of this work was to assess the possibility of restoring the electrical properties of neutron-irradiated diamonds by means of annealing. Changes in the material structure were monitored by measuring the optical absorption spectra containing bands assigned to the radiation defects. We assumed that the electrical properties of diamond are related to the content and behavior of structural defects.

We have studied the dynamics of annealing of the GR1 defect and production of the derivative defect H3 in the course of isothermal annealing of a neutron-irradiated diamond sample in a broad range of temperatures. These data will be used in subsequent analysis, which falls outside the framework of this experimental investigation.

A sample of the natural diamond pre-irradiated in an IR-8 reactor contained a great number of defects, including GR1. During the exposure, the fluence of fast neutrons reached 1.5×10^{17} cm^{-2} for $E > 3$ MeV and 1.3×10^{18} cm^{-2} for $E > 100$ keV, the fluence of thermal neutrons was 1.97×10^{18} cm^{-2}, and γ-radiation dose was 3 Grad.

The GR1 defect studied in this work represents a neutral vacancy [1] (that is, a zero-dimension defect according to Schottky), which is most simple from the standpoint of defect monitoring and data interpretation. On heating the crystal, mobility of this defect increases to a very large extent. As a result, the GR1 defects migrate over the sample and emerges at one-, two-, and three-dimensional defects (e.g., exhibiting annihilation or emerging under the dislocation extraplane, at the crystal boundary, or on any other plane). Therefore, annealing leads to the loss of GR1 defects with the formation of stable complexes with other defects (of both intrinsic and impurity type). In particular, collision with an A-type center (a diatomic nitrogen impurity defect) leads to the GR1 transformation into H3 [3].

As is known, annealing of the GR1 vacancy defects in a material is proportional to the temperature. Transformation of the corresponding absorption bands are readily observed at 550°C even for a comparatively short annealing times, while the treatment at 600°C may lead to decay of this defect [3]. For this reason, the experiment on isothermal annealing was performed at 550°C during a time reaching several tens of hours, at a 10-h step. The treatment was effected in a vacuum of 6×10^{-3} Torr. The measurements and calculations were performed both for the annealing of GR1 and the production of H3, the derivative defect.

The presence of defects and their concentration were determined from the optical absorption spectrum measured in the visible range. In order to suppress the phonon vibrations of the crystal lattice, the measurements were performed at the liquid nitrogen temperature. The defect concentration A_{GR1} was determined as the area under the corresponding absorption band in the spectrum.

Variation of the GR1 defect concentration A_{GR1} (normalized to unity) with time during the isothermal annealing can be described by a sum of two exponents [4], which reflects the two-component mechanism of this process:

$$A_{GR1} = (a_1/(a_1 + a_2))\exp(-t/\tau_{fast}) + (a_2/(a_1 + a_2))\exp(-t/\tau_{slow}). \quad (1)$$

1063-7850/00/2606-0496$20.00 © 2000 MAIK "Nauka/Interperiodica"

By plotting the experimental data in semilogarithmic coordinates (Fig. 1), it is possible to separate the slow and fast components and determine the parameters of equation (1). Then, variation of the normalized concentration of GR1 defects during annealing of the natural type IIa diamond at 550°C can be presented as function of the annealing time t (h):

$$A_{GR1} = 0.74\exp(-t/12.34) + 0.26\exp(-t/94.98), \quad (2)$$

where the fast component is characterized by the time constant τ_{fast} = 12.34 h and the slow component, by τ_{slow} = 94.98 h.

Using the experimental data obtained for the isothermal annealing at 550°C, we may calculate the time constants τ_{fast} and τ_{slow} for the annealing at any other temperature T, assuming that the GR1 defect transformation in type IIa diamonds retains its two-component character:

$$\tau_{fast} = \tau_{0,\,fast}\exp(E_m/(k_BT)) = 1.623\times10^{-14}\exp(28200/T), \quad (3)$$

$$\tau_{slow} = \tau_{0,\,slow}\exp(E_m(k_BT)) = 1.249\times10^{-13}\exp(28200/T), \quad (4)$$

where E_m = 2.43 eV [5] is the activation energy for the vacancy migration and $k_B = 8.617\times10^{-5}$ eV/K is the Boltzmann constant.

Using the above data, we have calculated the A_{GR1} values in the temperature interval 100–900°C using formula (1) with the preexponential coefficients 0.74 and 0.26 taken from formula (2). The results of these calculations are presented in Fig. 2. As is seen, annealing at a temperature above 800°C results in vanishing of the GR1 band intensity within one hour or less, in agreement with the published data [5]. The drop of A_{GR1} at T = 700–900°C takes place within a time interval 0–3 h and is described by a single straight line, which implies that only one component (slow) contributes to the process. The action of fast component, markedly affecting the total loss of GR1, is restricted to annealing times of the order $t \cong 4\tau_{fast}$. For the temperatures T = 900, 800, and 700°C, the corresponding annealing times are 6.5 s, 61.2 s, and 15.1 min, respectively. Note that isothermal annealing over this short time interval may be difficult to perform and study because of thermal inertia and some features of the furnace design.

At the temperatures T = 650 and 550°C, contribution of the fast component (Fig. 1) can be followed up to a time of $t \cong 4\tau_{fast} \cong 1.2$ and 50 h, respectively, after which only the slow component is determining the loss of GR1. For this reason, the curves describing a decrease in the defect concentration at $t > 1.5$ and 60 h (for T = 650 and 550°C, respectively) can be approximated by straight lines in the semilogarithmic scale employed. For the annealing at T = 450–500°C, both

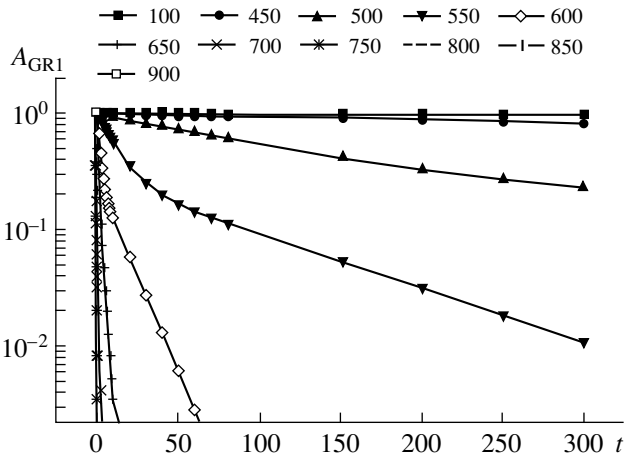

Fig. 1. Annealing of GR1 defects in a pre-irradiated type IIa diamond sample at various temperatures (°C) over a time period of 0–300 h.

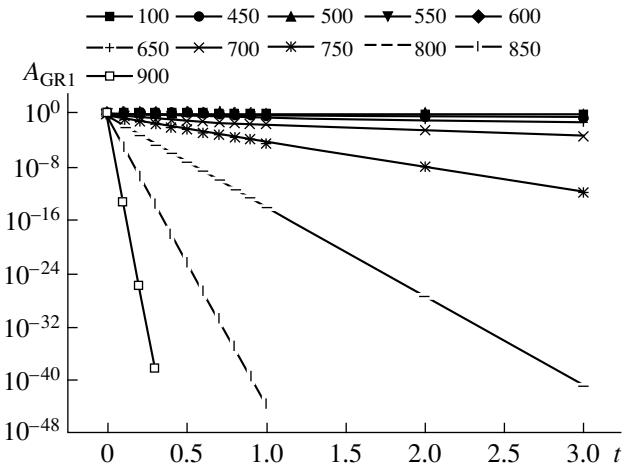

Fig. 2. Annealing of GR1 defects in a pre-irradiated type IIa diamond sample at various temperatures (°C) over a time period of 0–3 h.

fast and slow stages can be traced over the entire interval of annealing times (0–300 h) studied, since the characteristic time $t \cong 4\tau_{fast}$ for these temperatures (452.8 and 5644 h, respectively) exceeds 300 h.

In the temperature range from 100 to 400°C (Fig. 1), defects of the GR1 type in the natural type IIa diamond are virtually not annealed. Thus, the temperature T = 400°C can be considered as a threshold for the GR1 type defect transformation. Using a lower activation energy E_m^f = 1.68 eV [5] for the fast component and retaining E_m = 2.43 eV for the slow component, we obtain a slower annealing of GR1, since the time constant of the former process would increase to $\tau_{fast} = 6.356\times10^{-10}\exp(19500/T)$. For example, at T = 973 K (700°C) and E_m^f = 1.68 eV, we obtain τ_{fast} = 0.3200 h

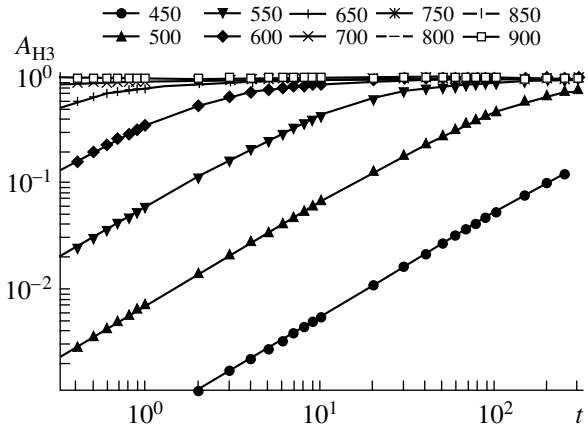

Fig. 3. Accumulation of H3 defects in a pre-irradiated type IIa diamond sample at various temperatures (°C) over a time period of 0–300 h.

(instead of 0.0627 h with E_m = 2.43 eV). This approximately equals to $\tau_{fast}(E_m = 2.43\ \text{eV}) = 0.3013$ h observed for the annealing temperature T = 923 K (650°C), which implies a 50-K shift in the annealing temperature. The existence of two values of the activation energy (E_m and E_m^f) is still unexplained [5], but produces little effect upon the calculation results.

Accumulation of the H3 defects is described by the following formula derived using the experimental data obtained 550°C and assuming the time constants τ_{fast} and τ_{slow} determined for GR1 to be valid for H3 as well:

$$A_{H3} = 1 - 0.74\exp(-t/12.34) - 0.26\exp(-t/94.98), \quad (5)$$

where the defect concentration A_{H3} is normalized to unity. Figure 3 shows the curves of the H3 defect production calculated by the equation

$$A_{H3} = 1 - 0.74\exp(-t/\tau_{fast}) - 0.26\exp(-t/\tau_{slow}) \quad (6)$$

and plotted in logarithmic coordinates. As seen, the curves are well approximated by straight lines of the type $f(t) = \text{const} \cdot t$ for the annealing times decreasing from 300 h at 450°C to, e.g., 1 h at 600°C. Then the curves attain a plateau (A_{H3} = 1). The proportionality to the annealing time is quite understood. Indeed, expanding the small exponents into series and restricting the expansion to two terms, we obtain from equation (6) the following approximate expression valid for any temperature of annealing of the natural type IIa diamond:

$$A_{H3} = (0.74\tau_{slow} + 0.26\tau_{fast})t/(\tau_{fast}\tau_{slow}). \quad (7)$$

For example, the accumulation of H3 at 550°C (Fig. 3) for $t \le 3$ h is approximately described by formula (7) as $A_{H3} = 6.270 \times 10^{-2}t$, with the maximum error (at t = 3 h) reaching 12%.

Note that, taking into account that defects of the H3 [1] type are annealed at $T > 1073$ K (800°C), no corrections for the loss of these defects was introduced into our calculations.

The total amount of the H3 defects accumulated in the sample (for $t \longrightarrow \infty$) is $A_{H3}^{\infty} = 0.644$ nm mm^{-1}, which corresponds to about 17% of the initial concentration of GR1 ($A_{GR1}^{0} = 3.841$ nm mm^{-1}).

The above results indicate that data on the isothermal annealing of the pre-irradiated natural type IIa diamond at 550°C can be used to calculate concentrations of the GR1 and H3 defects in a broad range of temperatures (100–900°C). Naturally, the results for 550°C are independent of the activation energies for the vacancy migration, because these parameters are implicitly represented by the values τ_{fast} = 12.34 h and τ_{slow} = 94.98 h obtained from experiment.

A significant decrease in the concentration of GR1 takes place upon the annealing for $t \cong 4\tau$ (by analogy with, e.g., the radioactive decay, which is natural since the two processes are described using identical mathematical formalism). Thus, should the fast component dominate (700–900°C), the annealing time can be restricted to $t \cong 4\tau_{fast}$, otherwise the annealing must proceed for $t \cong 4\tau_{slow}$.

The authors are grateful to the personnel of the IR-8 reactor (Kurchatov Institute of Atomic Energy, State Scientific Center of the Russian Federation) for their help in sample preparation and to Yu.A. Kashchuk for the dosimetric control of irradiated diamonds.

The work was supported by the International Science and Technology Center (project no. 447).

REFERENCES

1. *Natural Diamonds of Russia*, Ed. by V. B. Kvaskov (Polyaron, Moscow, 1997).
2. G. Davies and M. H. Nazare, J. Phys. C: Solid State Phys. **13**, 4127 (1980).
3. G. Davies, S. C. Lawson, A. T. Collins, *et al.*, Phys. Rev. B **46**, 13157 (1992).
4. G. Davies and A. T. Collins, Diamond Relat. Mater., No. 2, 80 (1993).
5. L. Allers, A. T. Collins, and J. Hiscock, Diamond Relat. Mater., No. 7, 228 (1998).

Translated by P. Pozdeev

Technical Physics Letters, Vol. 26, No. 6, 2000, pp. 499–501. Translated from Pis'ma v Zhurnal Tekhnicheskoĭ Fiziki, Vol. 26, No. 12, 2000, pp. 8–14.

Cascade Multiplication of a 26-GeV Electron Shower in a Lead Plate–Emulsion Sandwich Chamber

K. V. Aleksandrov, Yu. D. Aleshin, O. K. Egorov, V. V. Kolesnikov, G. I. Merzon, E. A. Pozharova, V. A. Ryabov, V. I. Silaev, V. A. Smirnitskiĭ, N. I. Starkov, I. S. Trostin, and V. A. Tsarev

Lebedev Physics Institute, Russian Academy of Sciences, Moscow, 117924 Russia

Institute of Theoretical and Experimental Physics, State Scientific Center of the Russian Federation, Moscow, 117259 Russia

Received November 17, 1999

Abstract—The electron–photon shower development in a lead plate–emulsion sandwich chamber with a total effective lead thickness of 3.5 radiation units was studied for an electron energy of 26 GeV. The experimental electron multiplication coefficient ($P^{\text{exp}} = 19.4 \pm 1.4$) agrees with a theoretical value ($P^{\text{calcd}} = 20.4$) calculated with corrections for the particle scattering and absorption. © *2000 MAIK "Nauka/Interperiodica".*

Recently, a series of experiments, involving the method of "far neutrinos" and detectors with large masses (≈100 tons), have been suggested to reveal the phenomenon of neutrino oscillations. Direct observation of the $\nu_\mu \longrightarrow \nu_\tau$ oscillations in the MINOS [1] and OPERA [2] projects is expected using lead plate–emulsion sandwich detectors weighing about 1000 tons. Nuclear photoemulsions offer good possibilities for identifying electrons in the $\nu_e + N \longrightarrow e^- + X$ reaction and, hence, the $\nu_\mu \longrightarrow \nu_e$ oscillations as well. In the photoemulsion experiment, the system sensitivity with respect to this mode is limited only by the ν_e admixture in the ν_μ beam.

Using nuclear photoemulsions provides a good quality of the primary electron beam rejection from an admixture of the π^0 meson decay products. These products are separated as having two or four tracks due to charged particles, in contrast to a single electron produced in the $\nu_e + N \longrightarrow e^- + X$ reaction. In order to assess the possibility of electron energy determination in a hybrid photoemulsion experiments, we have studied the electron–photon shower development in a lead plate–emulsion sandwich chamber.

Experimental design. The emulsion chamber comprised 22 layers of an R-2T nuclear photoemulsion spaced by 1-mm-thick lead plates. The total thickness of lead was 20 mm, the radiation pathlength in lead being 5.6 mm. The 50×50 mm^2 emulsion plates represented a sandwich of 180-μm-thick cellulose triacetate films coated from both sides with a 50-μm-thick cast emulsion layers. In order to exclude the contact of lead with the nuclear photoemulsion, the emulsion layers were coated with protective gelatin coatings having a thickness of a few microns.

The assembled chamber was exposed to a beam of 26-GeV electrons extracted from the accelerator of the Institute of High-Energy Physics. The exposure time was controlled so as to provide a total spill of 10^4 electrons. The layers of exposed emulsion reveal the pattern of the electromagnetic shower development upon passage through the lead plates.

The tracks in emulsion were visualized and analyzed on a MAS-1 setup [3], where the emulsion layers were scanned in depth and the tracks corresponding the high-energy electrons incident normally to the emulsion surface were unambiguously distinguished. The normal-incidence emulsion chamber ensures determination of the electron track direction with good precision. The chamber design provides for the matched passage from one emulsion layer to another, with the coordinate system being rigidly fixed with respect to the cut plate sides in the chamber. The accuracy of matching was 10 μm.

Experimental results and discussion. The visualization of tracks began from the first emulsion layer along the beam propagation direction. Here, the tracks with directions close to the normal to the emulsion plane (within a ±15° angle) were determined. A total examination of this layer revealed the integral pattern of the emulsion chamber filling by the tracks of electrons from the primary beam. Figure 1 illustrates this integral pattern by a projection of the track distribution onto one of the coordinate axes lying in the plane of emulsion. Here, points show the results of track counting over an 0.1×32 mm^2 band region (0.1 mm is the size of the objective visual field in one direction, and 32 mm is the scan length over the emulsion layer in the perpendicular direction). The solid curve in Fig. 1 pre-

1063-7850/00/2606-0499$20.00

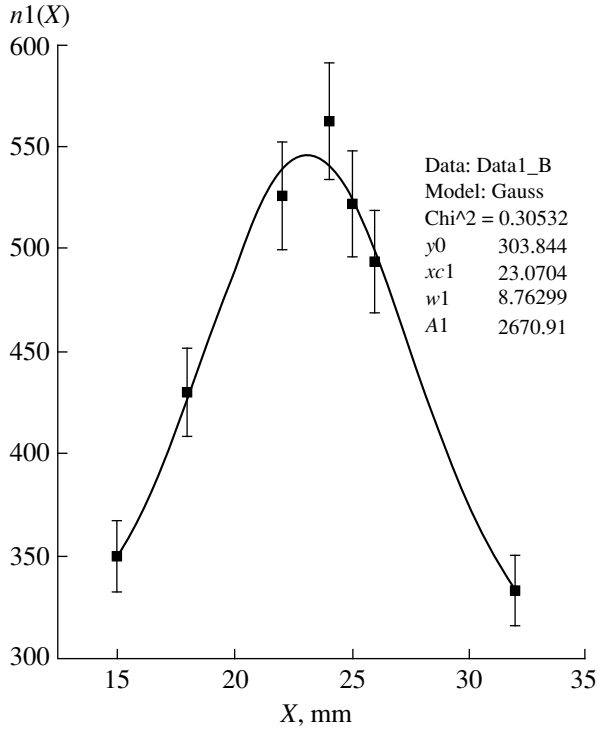

Fig. 1. Electron track distribution measured in the first emulsion plate along one of the coordinate axes lying in the plane of emulsion. Total number of tracks, calculated using the approximating Gaussian curve, is 3830.

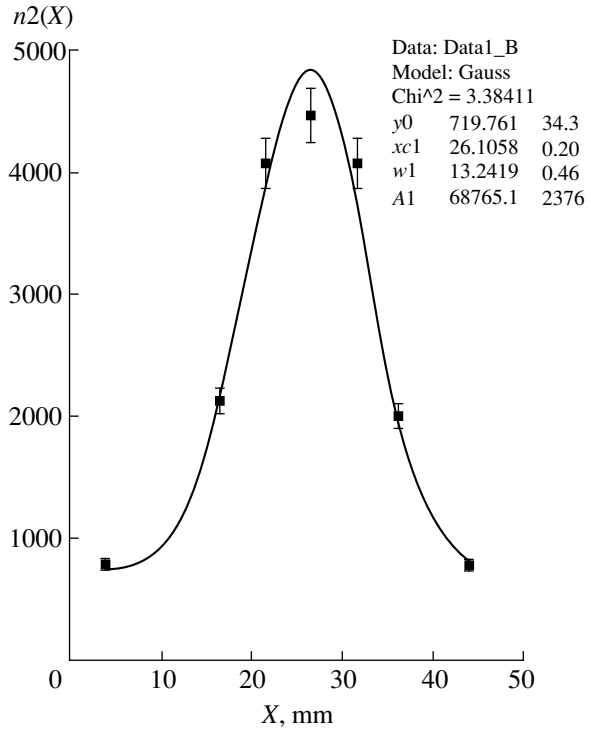

Fig. 2. Electron distribution measured in the penultimate emulsion plate along one of the coordinate axes lying in the plane of emulsion. Total number of tracks, calculated using the approximating Gaussian curve, is 74300.

sents approximation of the experimental data by the expression

$$Y = \frac{A}{\sigma\sqrt{\pi}} e^{-\left(\frac{x - x_c}{\sigma}\right)^2} + Y_0,$$

where $x_c = 23.1 \pm 0.4$ mm, $\sigma = 8.6$, and $Y_0 = 301$. As is seen, there is a pronounced background pedestal under the Gaussian curve. Apparently, this background is explained by the presence of electrons with different energies, entering as an admixture into the primary beam.

In order to study the electromagnetic cascade development in the emulsion upon passage through the lead plates, we have performed analogous integral examination of the penultimate emulsion layer in the emulsion chamber. Figure 2 shows the corresponding experimental data and the result of their approximation by a Gaussian function. The total multiplicity of particles upon the electron beam passage through the lead–emulsion sandwich is determined by the area under this curve.

In order to obtain a correct value of the coefficient of cascade multiplication in the shower, the experimental data have to be corrected. This is related primarily to the background subtraction from the distributions depicted in Figs. 1 and 2. Since the shower development in a cascade essentially reflects variation of the number of particles with the energy, we may expect that particles in the beam and in the background are characterized by different multiplication coefficients. In order to calculate the multiplication coefficient for electrons in the beam, we must analyze processes involved in their electromagnetic interaction with the substance [4, 5], including (1) internal bremsstrahlung radiation, (2) pair production, (3) Compton effect, and (4) ionization losses.

The total number of electrons in the cascade with an energy above E is given by the formula [5]:

$$N(E_0, E, t) = \sum_{n=0}^{\infty} nP(E_0, E, n, t),$$

where $P(E_0, E, n, t)$ is the probability to find n electrons with energies above E at an absorbing substance depth t for the primary electron beam energy E_0.

Using the reference data from [6], we obtain the following distribution of the absorption losses ΔE_{abs} (MeV) as function of the total lead thickness X (mm):

$$\Delta E_{\text{abs}}(X) = 14.7 - 5.4X + 0.7X^2.$$

The function of the electron multiplication upon the beam traveling through a distance t (in radiation units) in lead can be presented as

$$n(t) = -4.4 + 11.9t - 2.4t^2.$$

In our case, taking into account the absorption of cascade electrons in lead, the electron multiplication coefficient can be presented in the following form:

$$P_P = \int_{0.5}^{3.7} n(t)dt,$$

where the upper integration limit is determined by the number of radiation units in lead and the lower, by the effect of electron absorption and multiple scattering in lead.

A fraction of the cascade electrons is lost, besides absorption, as a result of their multiple scattering by large angles during passage through the lead plates. The multiplication coefficient calculated for the cascade electrons with an allowance for their absorption and multiple scattering in lead is $P^{\text{calcd}} = 20.4$.

The experimental value of the electron multiplication coefficient P^{exp} was determined using the formula

$$P^{\text{exp}} = \frac{\int G_2(x)dx}{\int G_1(x)dx} = 19.4 \pm 1.4,$$

where $\int G_2(x)dx$ is the total number of tracks in the penultimate emulsion plate (described by the Gaussian function without background) and $\int G_1(x)dx$ is the integral distribution of tracks in the first plate of the emulsion chamber (background subtracted). The integration limits are indicated in Figs. 1 and 2. The experimental value of the electron multiplication coefficient in lead and the result of calculation with the absorption and scattering corrections coincide to within the experimental error.

This work was supported by the Russian Foundation for Basic Research, project nos. 99-02-16195 and 98-02-17428.

REFERENCES

1. The MINOS Collab., The Hybrid Emulsion Detector for MINOS R&D Proposal, NuMI-L-473 (April 1999).
2. The OPERA Collab., A Long Baseline *ν*, Appearance Experiment in the CNGS Beam from CERN to Gran Sasso (Progress Report), CERN/SPSC. 99-20, SPSC/M635, LNGS-LOI 19/99 (August 27, 1999).
3. Yu. D. Aleshin, V. V. Kolesnikov, and V. I. Silaev, Prib. Tekh. Éksp., No. 2, 43 (1997).
4. S. Z. Belen'kiĭ and I. V. Ivanenko, Usp. Fiz. Nauk **69**, 591 (1959) [Sov. Phys. Usp. **2**, 912 (1959)].
5. J. Butcher and H. Messel, Nucl. Phys. **20**, 15 (1960).
6. Committee on Nuclear Science, *Studies in Penetration of Charged Particles in Matter*, Report No. 39 (Washington, 1964).

Translated by P. Pozdeev

Technical Physics Letters, Vol. 26, No. 6, 2000, pp. 502–504. Translated from Pis'ma v Zhurnal Tekhnicheskoĭ Fiziki, Vol. 26, No. 12, 2000, pp. 15–22.

Simulation of the Stepped Surface of a High-Resolution X-ray Diffractor

M. I. Mazuritsky, E. M. Latush, A. V. Soldatov, G. A. Ugol'nitskiĭ, V. L. Lyashenko, and A. Marcelli

Rostov State University, Rostov, Russia

Received January 18, 2000

Abstract—Three possible schemes of a high-resolution stepped X-ray diffractor have been analyzed, including those based on the steps of equal angular widths, the steps of equal heights (i.e., distances from the step edge to the beginning of the next step), and the symmetric steps (where a distance from the step edge to the focusing circumference is equal to the distance from the focusing circumference to the edge of the next step). It is shown that the first and the third schemes provide most stable characteristics. *© 2000 MAIK "Nauka/Interperiodica".*

An X-ray radiation spectrum with simultaneous beam focusing can be obtained with the aid of a cylindrically or spherically bent perfect crystals [1–3]. The methods using cylindrically bent crystals were first considered long ago [4–8]. The methods used for focusing the radiation generated in a small volume (i.e., by a point source) provide a rather high spectral resolution. The resolving power is usually understood as a dimensionless ratio $E/\Delta E$ or $\lambda/\Delta\lambda$, where E is the energy of an X-ray quantum and λ is the radiation wavelength. Denoting the angle formed by the incident beam and the reflecting atomic plane of the crystal by θ, we obtain from the Bragg law that the admissible deviation from the exact Bragg angle, $\Delta\theta$, determines the resolution, $\lambda/\Delta\lambda = \tan\theta/\Delta\theta$, and depends on the crystal mosaicity, the method used for obtaining the X-ray spectrum, and the area of the reflecting Bragg surface of the crystal or the so-called diffractor. The zone of the Bragg (diffraction) reflection is understood as a set of points on the crystallographic surface for which, within the given wavelength range ($\lambda - \Delta\lambda \le \lambda \le \lambda + \Delta\lambda$), the Bragg angle falls within $\theta - \Delta\theta \le \theta \le \theta + \Delta\theta$.

The larger the value of $\Delta\theta$, the greater the diffraction zone area and, as a consequence, the aperture and the intensity of the spectrum obtained. However, the attainment of a high spectrum intensity is not the only requirement; it is also necessary to reach a high spectral resolution (usually associated with a small reflecting area of the crystal). Both conditions can simultaneously be met by using not one but several crystals. The principle of a stepped diffractor, each step of which is an individual bent crystal, was considered in a number of works [9–11]. A variant of the high-transmission pseudospherical stepped X-ray diffractor meeting the condition of a high spectral resolution was first suggested in [10], where high spectral resolution was attained due to a constant angular width of each step ($\Delta\varphi$ = const). Previously [12, 13], we developed an algorithm for the computer simulation of diffraction zones for crystals with various surface curvatures (cylindrical, ellipsoidal, toroidal, etc.). Below, we will systematically analyze three possible models of stepped X-ray diffractors providing a high spectral resolution and the relationship between the maximum possible aperture and the resolving power of a diffractor.

Figure 1a shows a pseudospherical stepped diffractor similar to that considered earlier [10, 11] and the optical scheme of the corresponding focusing spectrometer. Figure 1b schematically shows a section of this diffractor by the plane of the focusing circle with the center at the point O'. The focusing circumference located in the horizontal plane passes through the point S of location of a point radiation source, the upper diffractor point A_0 (the middle of the central step), and, finally, the point I of the detector location. The section of each step by the focusing circle plane is an arc of the circumference of the radius $R_i = OA_i (R_i = R_{-i})$, with $A_iB_i = A_iD_i$, where $i = -N, -(N-1), \ldots 0, \ldots, (N-1), N$. Now, introduce the following notation:

$$\alpha_i = \angle A_0OA_i, \quad \beta_i = \angle A_0OB_i, \quad \Delta\varphi_i = |\beta_i - \alpha_i|, \quad \Delta\theta_i = \angle A_iSB_i, \quad \omega = \angle B_{-N}OB_N. \tag{1}$$

The angles α_i $|\beta_i - \alpha_i|$, and ω determine the location of the center, the angular halfwidth of the ith step on the focusing circumference, and the total angular width of the diffractor, respectively.

Obviously, the radiation incident onto the centers of each step forms the same angle with the tangent. It is this angle that is called the Bragg angle θ. Denote the range of the Bragg angle variation (caused by the finite angular halfwidth $\pm\Delta\theta_i$ of the ith step) by $\Delta\theta_i$. In spectroscopy, the $\Delta\varphi_i$ value does not exceed 10^{-2} rad. Then,

the approximate formula relating these quantities can be written as

$$\Delta\varphi_i \approx \frac{\tan\theta + \tan\alpha_i}{\tan\theta}\Delta\theta_i = \left[1 + \frac{\tan\alpha_i}{\tan\theta}\right]\Delta\theta_i. \quad (2)$$

The maximum $\Delta\theta_i$ value sets the spectral resolution of a diffractor. Now, we will consider three different models of a stepped diffractor and compare their limiting apertures and spectral resolving power.

The first model suggested in our earlier study [10] is characterized by the steps having equal angular widths, i.e., $\Delta\varphi_i = \text{const}(i)$. The angle ω with the vertex at the point O is divided into $2N + 1$ equal angles (Fig. 1b). Then, the halfwidth of each step is determined as

$$\Delta\varphi_i = \frac{\omega}{2(2N+1)}. \quad (3)$$

The total aperture of such a diffractor (and, therefore, also the integrated radiation yield) equals the sum of the apertures of individual steps. In the polar coordinates with origin at the point O, the middle point of each step lying on the focusing circumference is determined by the angle α_i and the radius R_i:

$$\alpha_i = \frac{\omega \times i}{2N+1}, \quad R_i = R_0\cos\alpha_i. \quad (4)$$

The angle θ is determined by the position of the point S on the circumference. The corresponding maximum angular width ω of a stepped diffractor cannot exceed 2θ. Now, denote the diffractor height along the Z-axis by H, then $L_i = D_iB_i$. The aperture of each step can be written as

$$\Omega_i = \frac{H \times L_i}{SA_i^2}\sin\theta. \quad (5)$$

Then the total aperture of a diffractor consisting of $(2N + 1)$ steps is given by the following equation:

$$\Omega = \frac{\omega \times H\sin\theta}{R_0(2N+1)}\sum_{i=-N}^{i=N}\frac{\cos\alpha_i}{\sin^2(\theta+\alpha_i)}. \quad (6)$$

In the limit (at $E/\Delta E \longrightarrow \infty$), we arrive at the following integral:

$$\Omega = \frac{H\sin\theta}{R_0}\int_{-\omega/2}^{\omega/2}\frac{\cos\alpha}{\sin^2(\theta+\alpha)}d\alpha \quad (7)$$

$$= \frac{H\sin\theta}{R_0}\left[\frac{\cos\theta}{\sin(\theta+\alpha)} + \frac{\sin\theta}{2}\ln\left(\frac{1+\cos(\theta+\alpha)}{1-\cos(\theta+\alpha)}\right)\right]_{\omega/2}^{-\omega/2}.$$

The apertures calculated by formulas (6) and (7) coincide.

The second model of diffractor suggested in [9] is characterized by the constant interstep spacing, $st = R_i - R_{i+1}$. Using the above notation, we arrive at the following expressions for the angles at $i > 0$:

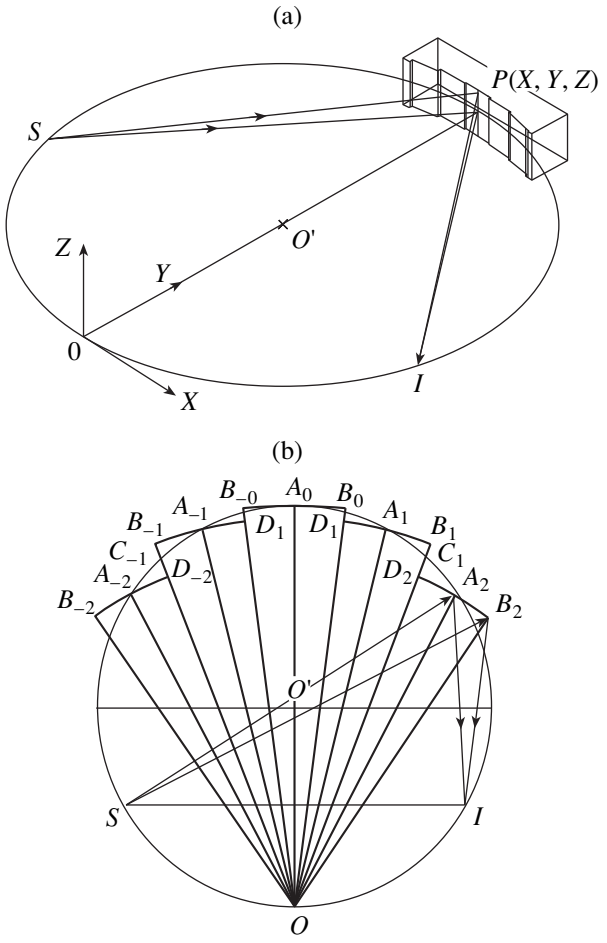

Fig. 1. Optical scheme for obtaining an X-ray spectrum and beam focusing. The *XYZ* are the reference systems; *O*' and *O* are centers of the focusing circle and the step curvatures, respectively; *S* and *I* are the points of location of the radiation source and its image, respectively.

$$\alpha_i = \arccos(1 - i(st/R_0)), \quad (8)$$

$$\Delta\varphi_i = \arccos(1 - i(st/R_0)) - 2\sum_{k=1}^{k=i-1}(-1)^k\arccos(1 - k(st/R_0)) + (-1)^i\beta_0. \quad (9)$$

At some values of the parameters st and β_0, the quantity $\Delta\varphi_i$ can acquire a negative value at the ith stage of the construction procedure. However, as is seen from Fig. 1b, such a solution is impossible. The geometric considerations show that $\Delta\varphi = \beta_i - \alpha_i$ and $\beta_i > \alpha_i$. Thus, within the framework of this model, it is impossible to design a diffractor with arbitrary resolving power because the latter is determined by the parameter β_0.

Finally, consider the third ("symmetric") variant of a stepped diffractor based on the following principle.

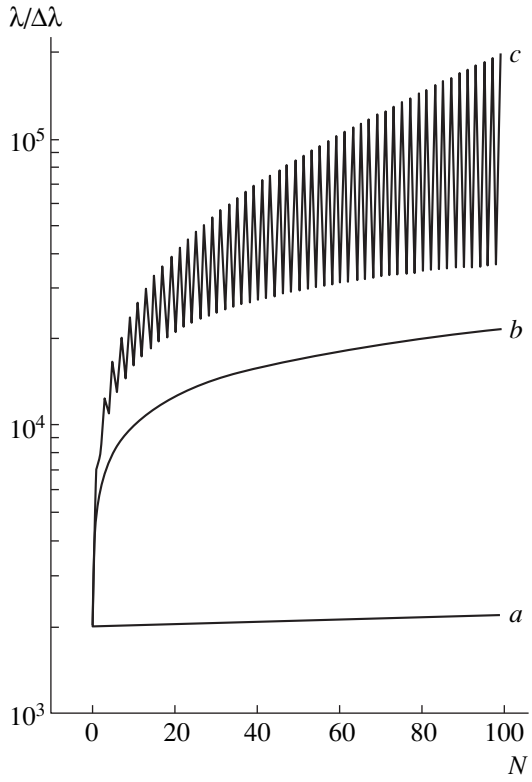

Fig. 2. Resolving power $\lambda/\Delta\lambda$ as function of the number of steps, *N*, for three models of the X-ray diffractor: (*a*) the model with $\Delta\varphi$ = const, (*b*) the symmetric model, and (*c*) the model with *st* = const.

The halfwidth of the zeroth step is limited, $\Delta\varphi_0 \le \Delta\theta = (\Delta\lambda/\lambda)\tan\theta$. The initial angles are $\alpha_0 = 0$ and $\beta_0 = \Delta\varphi_0$. It is necessary that the following equations would be fulfilled: $B_iC_i = C_iD_{i+1}$ and, therefore, also $D_iA_i = A_iB_i$. The angles are related as

$$\cos\alpha_{i+1} = 2\cos\beta_i - \cos\alpha_i, \quad \beta_{i+1} = 2\alpha_{i+1} - \beta_i. \quad (10)$$

One can readily show that, in this variant of diffractor, $\Delta\varphi_{i+1} < \Delta\varphi_i$ (in other words, the spectral resolution of each step it higher than the resolution of the preceding one). Therefore, the total resolution of the diffractor is determined by the resolution of the central step alone and does not decrease with increasing number of steps. Thus, in this model, an increase in the number of steps provides a higher spectral yield without any deterioration of the resolution. Thus, the condition $\Delta\varphi_i < \Delta\theta$ is fulfilled, which provides the necessary resolution of the diffractor. The total number of steps is determined by the condition $|\beta_N| \le \omega/2$. The diffractor aperture is obtained as

$$\Omega = \frac{H\sin\theta}{R_0}\left[\Delta\varphi_0 + 2\sum_{i=1}^{i=N}\frac{(\beta_i - \alpha_i)\cos\alpha_i}{\sin^2(\theta + \alpha_i)}\right]. \quad (11)$$

Figure 2 illustrates the resolving power for each diffractor step. Irrespective of the diffractor model used, the total diffractor resolution equals the minimum value of all the step resolutions. We calculated the diffractor resolution at R_0 = 320 mm and $\theta = 60°$. Obviously, for a real diffractor containing three to five steps, differences between the above models are insignificant. However, the first ($\Delta\varphi$ = const) and the third (symmetrical) models allow one to use any arbitrarily large number of steps close to its limiting value determined by the spectral properties (the rocking curve) in order to attain the maximum possible aperture. However, this is not always possible for the second model, where *st* = const. The point is that, at a fixed value of the parameter β_0, the value of *st* must fall within an interval equal to 1% of its absolute value, which provides fulfillment of the inequality $\Delta\varphi_i > 0$. Outside this range, the construction is inevitably restricted to the first several steps only. Thus, the first and the third models provide more stable characteristics.

REFERENCES

1. C. Bonnelle and C. Mande, *Advances in X-ray Spectroscopy* (Pergamon, New York, 1982).
2. A. K. Freund, *X-ray Optics* (ESRF, Grenoble, 1987).
3. A. G. Michette, *Optical System for Soft X-ray* (Plenum, New York, 1986).
4. J. W. M. DuMond and A. Kirpatrick, Rev. Sci. Instrum. **1**, 88 (1930).
5. H. H. Johann, Z. Phys. **69**, 185 (1931).
6. Y. Cauchois, J. Phys. Radium **3**, 320 (1932).
7. I. Von Hamos, Naturwissenschaften **20**, 705 (1932).
8. T. Johannson, Z. Phys. **82**, 507 (1933).
9. D. B. Wittry and S. J. Sun, Appl. Phys. **69**, 3886 (1991).
10. A. Marcelli, A. V. Soldatov, and M. I. Mazuritsky, European Patent No. 97830282.6–2208, deposited by INFN on 06/11/97, published on 12/16/98.
11. A. Marcelli, M. I. Mazuritsky, and A. V. Soldatov, Proc. SPIE **3448**, 210 (1998).
12. M. I. Mazuritsky, A. V. Soldatov, E. M. Latush, *et al.*, Pis'ma Zh. Tekh. Fiz. **25** (19), 11 (1999) [Tech. Phys. Lett. **25**, 763 (1999)].
13. Working variant of the program written in the DELPHI medium can be found at: http://www.projectx. aaanet.ru.

Translated by L. Man

Technical Physics Letters, Vol. 26, No. 6, 2000, pp. 505–507. Translated from Pis'ma v Zhurnal Tekhnicheskoĭ Fiziki, Vol. 26, No. 12, 2000, pp. 23–27.

A Multichannel Correlation Filter Based on a Photorefractive Crystal for the Processing of Varying Speckle Fields

Yu. N. Kulchin, R. V. Romashko, E. N. Piskunov, and A. A. Kamshilin

Far East State Technical University, Pushkinskaya ul. 10, Vladivostok, 690600 Russia
University of Joensuu, P.O. Box 111, SF-80101, Joensuu, Finland

Received January 10, 2000

Abstract—A method for the simultaneous processing of speckle fields generated by several single-fiber multimode interferometers is developed. The method uses a multichannel correlation filter based on a single photorefractive crystal. Mutual influence of the neighboring channels is analyzed, and it is shown that the simultaneous processing of several channels can be performed with the help of a single photorefractive crystal, provided that the interchannel spacing is not smaller than half of the size of the optical field pattern formed in the crystal plane. © *2000 MAIK "Nauka/Interperiodica".*

Holographic correlation filters are promising structures for the processing of speckle patterns formed by radiation fields of single-fiber multimode interferometers (SFMI) [1, 2]. In particular, such a filter can be based on a dynamic diffraction grating recorded in a photorefractive crystal (PRC) [2]. An important advantage of these correlation filters is their adaptability, that is, the ability of the dynamic grating recorded in the crystal to adjust itself to uncontrolled low-frequency variations in the environment. This feature opens a great field for the practical application of fiber optic measuring networks.

However, the processing of signals from multidimensional data transmitting and measuring networks, consisting of a large number of fiber optic measuring lines (channels), would require a large number of photorefractive crystals. This substantially complicates the processing system and makes it more expensive. A possible solution for this problem consists apparently in using a single photorefractive crystal for the simultaneous processing of signals from several measuring lines.

In this regard, the purpose of our work was to investigate the mutual influence of incoherent dynamic speckle fields of several SFMI during the processing of these fields with the help of a multichannel correlation filter based on a single PRC.

The principle of operation of a PRC correlation filter is as follows. When a coherent optical radiation enters the PRC, a set of chaotically oriented phased gratings, resulting from interference of the primary wave with a large number of secondary waves scattered by crystalline defects, is formed within the crystal [2]. Such a complicated diffraction grating gives rise to the fanning effect, whereby the power is transferred from the incident wave to the scattered waves due to diffraction of the former wave on the chaotic set of gratings. Intensity of the fanning waves depends on the contrast m of the interference pattern formed by interference of the incident and scattered beams.

When another radiation (incoherent to the primary one) enters the crystal, one more set of chaotically oriented diffraction gratings will be recorded in the bulk and one more fanning wave will be excited. Based on the theory [3, 4], one can demonstrate that, for the case of overlapping domains of mutually incoherent optical fields, the contrast of the resulting interference pattern can be expressed as

$$m = \frac{m_0}{1 + k\sigma(\zeta)}, \tag{1}$$

where m_0 is the initial contrast of the interference pattern, $\sigma(\zeta)$ is the parameter describing overlap of the incoherent field domains in the crystal, and k is the constant describing the degree of spatial nonuniformity of the incoherent field.

Using methods developed in [5], we can show that, when cross-sections of the optical fields have approximately circular shapes, the overlap parameter can be expressed as

$$\sigma(\zeta) = \begin{cases} \frac{1}{\pi}(2\arccos\zeta - 2\zeta\sqrt{1-\zeta^2}), & \zeta \le 1, \\ 0, & \zeta > 1 \end{cases} \tag{2}$$

where $\zeta = x/d$, x is the spacing between the centers of the fiber guide end images formed in the crystal plane, and d is the linear dimension of the fiber end image.

Formulas (1) and (2) show that, in the case of partially or totally overlapping optical fields from different

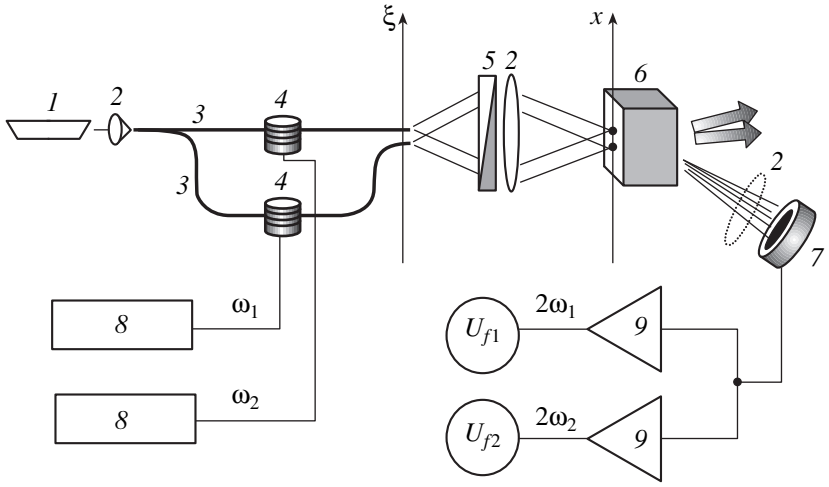

Fig. 1. Schematic diagram of the experimental setup: (*1*) He–Ne laser; (*2*) objective lens; (*3*) single-fiber multimode interferometer; (*4*) piezoelectric ceramic element; (*5*) polarizer; (*6*) $Bi_{12}TiO_{20}$ crystal; (*7*) photodetector; (*8*) low-frequency oscillator; (*9*) lock-in amplifier.

sources ($\zeta < 1$), the homogeneity of the field in the overlap region increases and the contrast m decreases, which results in the mutual lowering of intensities of the fanning waves in both channels.

The mutual influence of channels in a two-channel adaptive filter was investigated experimentally. Mutually incoherent radiations of two SFMI (Fig. 1), which were sinusoidally modulated at frequencies ω_1 and ω_2 with the help of piezoelectric ceramic elements, passed through a polarizer and were focused within the PRC with an objective lens. The fanning signal was collected by a photodetector and fed to the lock-in amplifiers tuned, according to [2], to $2\omega_1$ and $2\omega_2$. This ensured extraction of the contributions from each channel.

Figure 2 shows the amplitudes of fanning signals measured in each channel as functions of the interchannel spacing. When radiations of different SFMI passing through the crystal are sufficiently separated from each other, the level of the fanning signal in each channel remains almost constant. In the case of substantially overlapping images of the fiber guide ends, formed in the crystal input plane ($x \sim d/2$), we observed substantial lowering (by 3 dB) of the fanning signal in both channels.

In order to experimentally investigate crosstalk noises arising at small separations in both channels, we placed an objective lens between the crystal and the photoreceiver (Fig. 1). As a result, the two channels were spatially separated in the far field. The signal from the photoreceiver placed in the fanning field of the second channel entered a selective amplifier tuned to the operating frequency of the first channel ($2\omega_1$). This allowed us to determine the degree of mutual influence between the channels determined by the interaction of their optical fields within the crystal. Figure 2 presents the spectral component of fanning signal in the second channel, corresponding to the operating frequency of the first channel, as function of the interchannel spacing in the crystal. It was found that the level of this signal is independent of the interchannel spacing and does not exceed the level of intrinsic noise in the second channel (11 dB). This result indicates that there is almost no interpenetration of the information component between the channels.

Thus, the results of investigations allow us to infer that it is possible to process two or more signals of fiber optic measuring lines (channels) with the help of a sin-

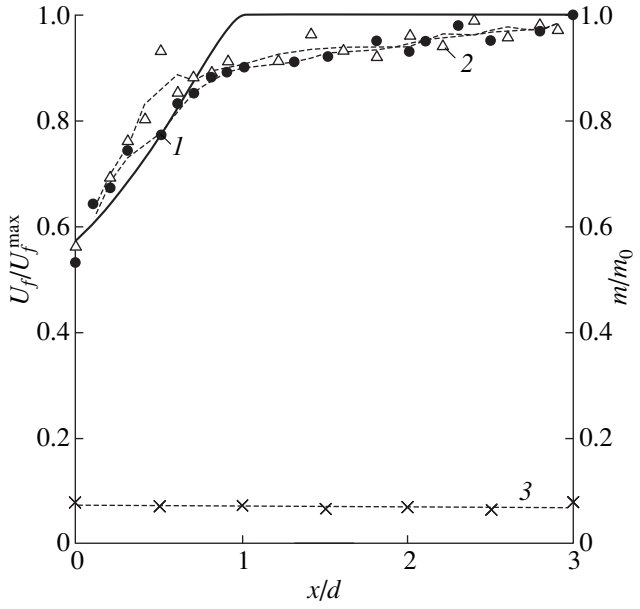

Fig. 2. Fanning signals in different channels (dashed lines) and the interference pattern contrast (solid line) vs. relative interchannel spacing: (*1*) channel no. 1 (ω_1); (*2*) channel no. 2 (ω_2); and (*3*) channel no. 1 (ω_2).

gle photorefractive crystal, provided that the distance between images of optical fields of each channel in the crystal plane is not smaller than half of the image formed by one channel.

REFERENCES

1. Yu. A. Bykovskiĭ, Yu. N. Kulchin, O. B. Vitrik, *et al.*, Kvantovaya Élektron. (Moscow) **17**, 95 (1990).
2. A. A. Kamshilin, T. Jaaskelainen, and Yu. N. Kulchin, Appl. Phys. Lett. **73** (6) (1998).
3. A. Yariv, in *Optical Electronics* (Saunders College Publ., Philadelphia, 1991, 4th ed.), Chap. 18, pp. 673–669.
4. M. Born and É. Wolf, *Principles of Optics* (Pergamon Press, Oxford, 1969, 4th ed.; Nauka, Moscow, 1973).
5. G. A. Korn and T. M. Korn, *Mathematical Handbook for Scientists and Engineers* (McGraw-Hill, New York, 1968; Nauka, Moscow, 1978).

Translated by A. Kondrat'ev

Technical Physics Letters, Vol. 26, No. 6, 2000, pp. 508–509. Translated from Pis'ma v Zhurnal Tekhnicheskoĭ Fiziki, Vol. 26, No. 12, 2000, pp. 28–30.

Order Parameter of Oxygen Atoms and Superconductivity of $YBa_2Cu_3O_{7-\delta}$ Compound

E. M. Gololobov

Institute of Solid State and Semiconductor Physics, Belarussian Academy of Sciences, Minsk, 220072 Belarus

Received December 28, 1999

Abstract—The orthorhombic structure of compounds of the $YBa_2Cu_3O_{7-\delta}$ compositions was studied and the long-range order parameter of oxygen atoms in the basal plane of the crystal lattice was determined. It is established that the critical temperature T_c is more sensitive to changes in the order parameter than in the $(7 - \delta)$ value. *© 2000 MAIK "Nauka/Interperiodica".*

One of the most important tasks of the studies of high temperature superconductors (HTSC) is to improve the superconducting characteristics of materials. The value of the critical temperature of transition to the superconducting state (T_c) in $YBa_2Cu_3O_{7-\delta}$ superconductors is determined mainly by the amount of oxygen atoms $(7 - \delta)$ and their ordering during the formation of an orthorhombic crystal lattice. The superconducting properties of the $YBa_2Cu_3O_{7-\delta}$ compounds are usually characterized by the parameter $(7 - \delta)$. Numerous theoretical and experimental studies show that the critical temperature T_c also depends on the order of oxygen atoms in the …–Cu–O–Cu–… chains running along the *b*-axis in the basal (110) plane. However, the long-range order parameter and its value are almost never considered in the structural studies of HTSC materials.

The present study is aimed to determine the long-range order parameter η for oxygen atoms located in the basal (110) plane and introduce this parameter into the practice of X-ray diffraction studies of the $YBa_2Cu_3O_{7-\delta}$ compound.

The theoretical study [1] showed that orthorhombicity (Δ) of the $YBa_2Cu_3O_{7-\delta}$ compounds is determined not only by the difference in the *a* and *b* lattice parameters, but is also a linear function of the long-range order parameter of oxygen atoms located in the basal (110) plane. In other words, $\Delta(\eta) = b - a = \gamma\eta$, whence it follows that $\eta = \Delta/\gamma$, where γ is the coefficient that can be determined experimentally from the maximum value of $\Delta_{max} = (b - a)_{max} = 0.0780$ Å for the stoichiometric compound $YBa_2Cu_3O_7$. In the latter compound, 50% of oxygen vacancies in the basal plane are occupied by oxygen atoms and $\eta_{max} = 0.5$, which corresponds to the complete order (all the vacancies along the *b*-axis are occupied by oxygens). Thus, we obtain $\gamma = \Delta_{max}/\eta_{max} = 0.156$.

We performed experimental studies on $YBa_2Cu_3O_{7-\delta}$ single crystals grown by the method of spontaneous crystallization from solution, followed by isothermal annealing for time *t* in the oxygen atmosphere at a fixed pressure and quenching to room temperature in the same atmosphere.

The temperature of the transition to the superconducting state was measured by the magnetic method within an accuracy of ±0.1 K.

X-ray diffraction studies of the grown crystals were made on a DRON-3 diffractometer (CuK_α radiation). The samples contained no additional phases. The *a*-, *b*-, and *c*-parameters were determined in the asymmetric geometry using the 10.11, 01.11, and 00.11 reflections with an accuracy of ±0.0005 Å. The oxygen con-

Table

t, h	T_c, K	$7 - \delta$	*C*, Å	Δ, Å	η	*I*(00.11)
0	88.7	6.88	11.6985	0.0680	0.436	300
20	90.4	6.90	11.6930	0.0685	0.439	320
63	91.5	6.92	11.6900	0.0690	0.442	333
110	92.1	6.93	11.6845	0.0700	0.449	340
170	92.3	6.94	11.6780	0.0745	0.477	348
300	92.5	6.94	11.6755	0.0750	0.481	354

1063-7850/00/2606-0508$20.00 © 2000 MAIK "Nauka/Interperiodica"

tent $(7 - \delta)$ in the $YBa_2Cu_3O_{7-\delta}$ lattice was determined by interpolating the dependences of the lattice parameter c on $(7 - \delta)$ and T_c on $(7 - \delta)$ taken from [2]. The relative integral intensities of the 00.11 reflection, $I(00.11)$, were determined for all samples.

Table shows the results of the structural study of single crystal $YBa_2Cu_3O_{7-\delta}$ samples.

It is seen that, while approaching the lattice saturation with oxygen, the critical temperature T_c of $YBa_2Cu_3O_{7-\delta}$ becomes more sensitive to changes in the long-range order parameter than in the oxygen content in the unit cell. The integral intensity of the 00.11 reflection increases with η, which indicates a certain dependence of the integrated intensity of X-ray reflections on the long-range order parameter of oxygen atoms in the $YBa_2Cu_3O_{7-\delta}$ lattice.

ACKNOWLEDGMENTS

The author is grateful to N.A. Kalande for providing samples for X-ray studies.

REFERENCES

1. A. G. Khachaturyan and J. W. Morris, Phys. Rev. Lett. **59**, 2776 (1987).
2. R. J. Cava, B. Batlogg, C. H. Chen, *et al.*, Phys. Rev. B **36**, 5719 (1987).

Translated by L. Man

Technical Physics Letters, Vol. 26, No. 6, 2000, pp. 510–513. Translated from Pis'ma v Zhurnal Tekhnicheskoĭ Fiziki, Vol. 26, No. 12, 2000, pp. 31–39.

The Formation and Properties of Surface Phosphide on (100)W

N. R. Gall[1], E. V. Rut'kov, and A. Ya. Tontegode

Ioffe Physicotechnical Institute, Russian Academy of Sciences, St. Petersburg, 194021 Russia

Received January 28, 2000

Abstract—Adsorption of PCl_3 molecules on the (100)W surface has been studied over a wide temperature range from 300 to 2000 K. It is shown that adsorption at $T > 1100$ K results in the formation of a surface tungsten phosphide with the WP composition and a surface concentration of phosphorus atoms of $(1 \pm 0.15) \times 10^{15}$ cm^{-2}. Adsorption of silicon atoms on the surface phosphide at 1300 K results in the displacement of phosphorus atoms from the surface and their replacement by silicon atoms. © *2000 MAIK "Nauka/Interperiodica".*

Elements of group V of the Periodic Table, and, first of all, nitrogen and phosphorus, are usually considered as harmful (poisoning) impurities in materials science [1, 2]. Phosphorus is the element intermediate between the interstitial and the substitutional elements, but, in the character of interactions with metal lattices, it is closer to silicon and sulfur than to nitrogen [3]. At the same time, in the chemical interactions, phosphorus often behaves as an analog of carbon [4]. Similarly to carbides and nitrides, bulk metal phosphides have high melting points and are characterized by very strong metal–nonmetal bonding.

However, unlike silicon, carbon, and chalcogens, the interactions of group V elements with the surfaces of refractory metals are studied insufficiently. The only exception is presented by numerous articles on the adsorption of nitrogen, ammonia, and nitrogen oxides on platinum [5, 6] and transition metal [7] surfaces, which were dictated by the practical needs of the heterogeneous catalysis (i.e., the task of studying the mechanisms of nitrogen binding). In this context, phosphorus is the least studied element: to our knowledge, no works were devoted to the adsorption of phosphorus on the surfaces of refractory metals and the related processes.

1. EXPERIMENTAL

The study was performed on a high-resolution Auger spectrometer in an ultrahigh vacuum ($p \sim 10^{-10}$ Torr) [8]. The specimen was a $1 \times 0.02 \times 40$ mm polycrystal line tungsten ribbon heated by alternating current. The ribbon surface was cleaned by cycles of annealing in ultrahigh vacuum and in an oxygen atmosphere ($p_{O_2} \sim 10^{-6}$ Torr) at 2500 K. The clean ribbon surface showed only the Auger peaks of tungsten. During cleaning, the ribbon acquired a textured structure, with a (100)W face emerging at the surface and a work function typical of this face, $e\varphi = 4.65$ eV [9]. X-ray diffraction study showed a high degree of the crystal face orientation with respect to the surface (99.9%). The ribbon temperature was measured by a micropyrometer. In the nonpyrometric range, it was obtained by a linear extrapolation of the temperature–current curve.

The surface coverage of phosphorus adatoms was obtained by adsorption of PCl_3 molecules. In some experiments, we also used silicon, which was uniformly sputtered over the whole ribbon surface from a $1 \times 1 \times 40$ mm strip parallel to the ribbon surface. We measured the Auger peaks of phosphorus with $E = 121$ eV, silicon with $E = 92$ eV, chlorine with $E = 186$ eV, and also a tungsten triplet with $E = 162$–177 eV.

2. RESULTS AND DISCUSSION

2.1. Interaction of Phosphorus Trichloride with the (110)W Surface

Adsorption of PCl_3 molecules at room temperature led to the appearance of Auger peaks with the energies $E = 121$ and 186 eV corresponding to the LVV Auger transitions in adsorbed phosphorus and chlorine atoms [10]. Then the surface was heated with simultaneous recording of the transformations occurring in the Auger spectrum.

Variation of the Auger signals of chlorine and phosphorus during PCl_3 adsorption on the tungsten surface until saturation at 300 K followed by heating is illustrated by Fig. 1. It was found that heating up to $T \sim 700$–1100 K led to gradual removal of chlorine from the metal surface and to a slight increase in the Auger signal of phosphorus, probably because of its reduced screening by chlorine atoms. At $T > 1100$ K, no Auger signal of chlorine was observed at all, which could be caused by its desorption in the form of Cl_2 molecules. The above temperature interval is close to that used in

[1] *e-mail:* gall@ms.ioffe.rssi.ru

the vapor phase epitaxy of A_3B_5 semiconductors [11], where PCl_3 molecules are used as an effective agent for the phosphorus transfer to the surface of a growing crystal, whereas chlorine plays the part of an undesirable impurity that can readily be removed from the surface.

2.2. The Formation and Properties of Surface Tungsten Phosphide

The adsorption of phosphorus trichloride molecules on (100)W for 2–3 min at $P_{PCl_3} = 10^{-6}$ Torr and T = 1100 K resulted in the formation of a surface coating of phosphorus atoms. The Auger signal of phosphorus attains saturation and coincides with its maximum value reached upon annealing of the adlayer of PCl_3 molecules formed at room temperature. In this case, $l_P/l_W^0 = (3.0 \pm 0.3)$, whereas the intensity of the Auger signal of tungsten decreases by a factor of ~1.1. Very weak screening, which is characteristic of the surface rather than of the bulk chemical compounds, led us to a conclusion that, in this case, we deal with the adsorption of P atoms on the surface rather than with the formation of bulk tungsten phosphide.

We also established that the surface concentration of phosphorus in this coating was independent of the deposition temperature in the range 300–1200 K, which was also indicative of the surface rather than of the bulk nature of the adsorption state formed. It was logical to call this state surface tungsten phosphide. Under these conditions, no chlorine was detected on the surface at all.

2.3. Thermal Stability of Surface Tungsten Phosphide

As is seen from Fig. 1, the removal of phosphorus from the surface of tungsten phosphide occurs over a wide temperature range (1350–2000 K). The mechanism of this process (via dissolution in the bulk and thermal desorption) is still unclear. However, very high temperatures lead to an assumption that phosphorus is removed due to thermal desorption, at least at small coverages. Assuming that desorption is the first-order process, the adatom lifetime with respect to desorption obeys the Arrhenius relationship with the preexponent factor $C = 10^{13}$ s^{-1} [6]. Thus, one can estimate the desorption energy at $\theta \longrightarrow 0$ as $E_{des} \sim 5.7$ eV.

2.4. Absolute Phosphorus Concentration in Surface Tungsten Phosphide

In order to clarify the physical nature of the above phenomenon, we have to measure the absolute phosphorus concentration in the surface phosphide. Unfortunately, no standard phosphorus-containing substrates with independently measured phosphorus concentration are available, and, therefore, we had to use the standard substrates with other adsorbates (C, Si, S) as was done earlier for the S/(100)W system [12]. To calculate the relative elemental sensitivity coefficient for phosphorus and the above elements, k_P/k_A, we used the standard spectra given in [10].

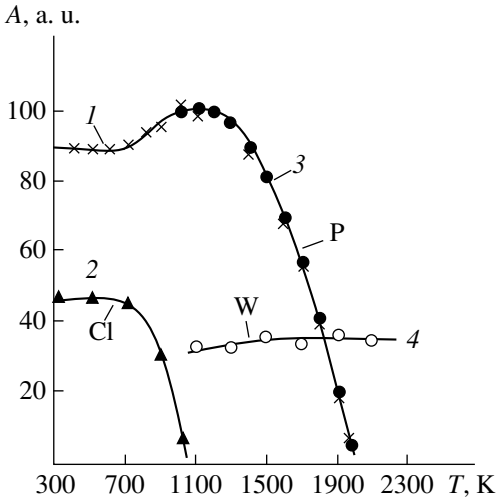

Fig. 1. Variation of the Auger signal of phosphorus (curve *1*, crosses) and chlorine (curve *2*) during the adsorption of PCl_3 molecules on the (100)W face up to saturation at 300 K, followed by 10-s annealings at a 100 K step; the change in the Auger signals of phosphorus (curve *3*, dots) and tungsten (curve *4*) during adsorption of PCl_3 molecules on the (100)W surface up to saturation at 1100 K, followed by 10-s annealings at a 100 K step.

As is known, the intensity of the Auger signal from a homogeneous sample, containing a given component with the bulk concentration n_i, can be calculated by the formula

$$l_i = k_i n_i \lambda_i T, \tag{1}$$

where l_i is the Auger signal intensity of the component to be determined, k_i is the elemental sensitivity coefficient, λ_i is the free path of Auger electrons of the ith component, and T is the transmission function of the spectrometer. Ignoring all possible effects of the chemical states of the elements on the intensities of Auger transitions and the possible enrichment of the standard sample surface with one of the components, we calculated the k_P/k_A ratio using the known data. With this aim, we applied formula (1) to each of the spectra from [10] and then divided one formula by another. Upon simple transformations, we arrive at

$$k_P/k_A = (l_P^0/l_A^0)(n_A\lambda_A)/(n_P\lambda_P), \tag{2}$$

where l_P^0/l_A^0 is the ratio of amplitudes of the Auger peaks of phosphorus and one of the above nonmetals taken from handbook [10].

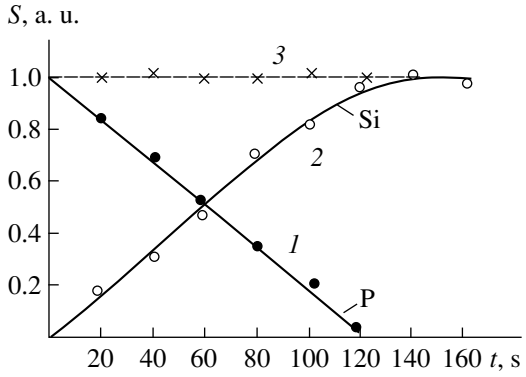

Fig. 2. Time variation in the surface coverage with (*1*) phosphorus and (*2*) silicon during sputtering of Si atoms onto surface tungsten phosphide WP at 1300 K and (*3*) the calculated total concentration of adatoms of both adsorbates. In both cases $\theta = 1$ corresponds to a concentration of 1×10^{15} cm^{-2} equal to the concentration of W atoms on the (100) face. Silicon flux density is 8.6×10^{12} cm^{-2} s^{-1}.

The surface concentration of adsorbate A and its Auger signal [8] for surface chemical compounds are related as

$$l_A = N_A k_A T. \quad (3)$$

In this formula, we use the same notation as in (1). Substituting the calculated k_P/k_A values into (3) and taking into account that the surface silicon, sulfur, and carbon concentrations in the corresponding surface compounds on the (100)W face are the same and equal to $(1 \pm 0.15) \times 10^{15}$ cm^{-2}, we obtain the average value $N_P = (1 \pm 0.6) \times 10^{15}$ cm^{-2}. In other words, the compound formed on the tungsten surface has the approximate composition WP. Our calculations showed a considerable scatter inevitable in determination of the surface concentrations from the corresponding bulk values.

2.5. Simultaneous Silicon and Phosphorus Adsorption on the (100)W Face

Experiments on the simultaneous silicon and phosphorus adsorption on the (100)W face allowed us to refine the stoichiometry of tungsten phosphide formed and confirmed its essentially surface nature.

Our previous studies showed that if nonmetal atoms of various nature are simultaneously present on the surface of a refractory metal at temperatures characteristic of the formation of surface chemical compounds, several competing processes can occur on the surface [12]. In some cases, these processes can result in simultaneous desorption of atoms (S + Si/W, Mo, Re; O + Si/W, Re) [13–15] and in other cases, in the displacement of some atoms from the surface to the metal bulk with the formation of solid solutions (C + Si/W, Re, Mo; S + C/W, Mo) [8, 15]. These competing processes were observed only for the surface but not for the bulk carbides, sulfides, silicides, and oxides [12]. This phenomenon was used in our previous studies as a diagnostic criterion for distinguishing the surface and the bulk carbides on Mo substrates.

It was established that silicon deposited onto the (100)W face at $T = 1300$–1400 K displaces phosphorus from this face, with the rate of the silicon accumulation on the surface remaining the same as in the absence of phosphorus. At a silicon dose equal to $N_{Si} = 1 \times 10^{15}$ cm^{-2}, phosphorus is completely removed from the surface, and the surface silicide is formed. The Auger signals of both adsorbates obey the linear law (Fig. 2) and, therefore, it is logical to assume that phosphorus is displaced from the surface by silicon in the one-to-one ratio. Obviously, Si and P atoms compete for the same adsorption centers on the metal surface. The total concentrations of both nonmetals calculated under this assumption remain constant during the whole process (Fig. 2). This fact allows us to refine the phosphorus concentration in surface phosphide estimated above, which is equal to the silicon concentration in the surface silicide and amounts to $(1 \pm 0.15) \times 10^{15}$ cm^{-2}. The displacement effect has never been observed during the formation of bulk carbides, silicides, or sulfides for any of the adsorbates studied. This seems also to be true for phosphorus, indicating that phosphorus is in the essentially surface and not the bulk state.

CONCLUSION

Adsorption of phosphorus trichloride on the (100)W face at 1100–1300 K results in the formation of surface phosphide with the WP composition (relative to the surface metal atoms) and the adsorbate concentration $(1 \pm 0.15) \times 10^{15}$ cm^{-2}. Similarly to other nonmetals in the surface chemical compounds, phosphorus atoms in surface phosphide participate in the competing processes occurring on the surface and, as a result, are displaced from the surface by silicon atoms at the temperatures 1300–1400 K.

ACKNOWLEDGMENTS

This study was supported by the State Program "Surface Atomic Structures" of the Ministry of Science and Technologies of the Russian Federation, project no. 4.9.99.

REFERENCES

1. E. Fromm and E. Gebhardt, *Gase und Kohlenstoffin Metallen* (Springer-Verlag, Berlin, 1976; Metallurgiya, Moscow, 1980).
2. M. Guttmann and D. McLean, in *Interfacial Segregation*, Ed. by W. C. Johnson and J. M. Blakely (American Society for Metals, Metal Park, Ohio, 1979), pp. 261–347.
3. *Physical Metallurgy*, Ed. by R. W. Cahn (North-Holland, Amsterdam, 1965; Mir, Moscow, 1968), Vol. 2.

4. F. A. Cotton and G. Wilkinson, *Advanced Inorganic Chemistry* (Wiley, New York, 1966, 2nd ed.; Mir, Moscow, 1969), Vol. 2.
5. C. N. R. Rao and G. Ranga Rao, Surf. Sci. Rep. **13** (7), 221 (1991).
6. M. W. Roberts and C. S. McKee, in *Chemistry of the Metal-Gas Interface* (Clarendon Press, Oxford, 1978), pp. 300–331.
7. L. R. Clavenna and L. D. Schmidt, Surf. Sci. **22**, 365 (1970).
8. N. R. Gall, E. V. Rut'kov, and A. Ya. Tontegode, Thin Solid Films **266**, 229 (1995).
9. V. S. Fomenko, *Emissive Properties of Materials. A Handbook* (Naukova Dumka, Kiev, 1981).
10. L. E. Davice, N. C. McDonald, P. W. Palmberg, *et al.*, *Handbook of Auger Electron Spectroscopy* (Physical Electronics Ind., Eden Prerie, 1976).
11. T. Bechstedt and R. Enderlein, *Semiconductor Surfaces and Interfaces. Their Atomic and Electronic Structures* (Academie-Verlag, Berlin, 1988; Mir, Moscow, 1990).
12. N. R. Gall, E. V. Rut'kov, A. Ya. Tontegode, and M. M. Usufov, Phys. Low-Dimens. Semicond. Struct. **3**–**4**, 27 (1999).
13. N. R. Gall', E. V. Rut'kov, A. Ya. Tontegode, and M. M. Usufov, Pis'ma Zh. Tekh. Fiz. **20** (18), 65 (1994) [Tech. Phys. Lett. **20**, 752 (1994)].
14. N. R. Gall', E. V. Rut'kov, and A. Ya. Tontegode, Fiz. Tverd. Tela (St. Petersburg) **42**, 186 (2000) [Phys. Solid State **42**, 377 (2000)].
15. N. R. Gall', E. V. Rut'kov, A. Ya. Tontegode, and M. M. Usufov, Fiz. Tverd. Tela (St. Petersburg) **38**, 2541 (1996) [Phys. Solid State **38**, 1394 (1996)].
16. V. N. Ageev, E. Yu. Afanas'eva, N. R. Gall', *et al.*, Pis'ma Zh. Tekh. Fiz. **12**, 565 (1986) [Sov. Tech. Phys. Lett. **12**, 231 (1986)].

Translated by L. Man

Technical Physics Letters, Vol. 26, No. 6, 2000, pp. 514–516. Translated from Pis'ma v Zhurnal Tekhnicheskoĭ Fiziki, Vol. 26, No. 12, 2000, pp. 40–45.

The Energy of Fracture of a Film of Carbon Monoxide Adsorbed on a Tungsten Single Crystal Surface

O. L. Golubev and V. N. Shrednik

Ioffe Physicotechnical Institute, Russian Academy of Sciences, St. Petersburg, 194021 Russia

Received February 7, 2000

Abstract—The adsorption and desorption of carbon monoxide were studied on a tungsten single crystal in a field electron microscope. The most interesting effects were observed for the CO desorption from the crystal surface regions containing the {100}W cubic faces. In the course of desorption from these regions, the adsorbed electropositive film, retaining sharp boundaries, shrank toward the <100> poles. The desorption energy value (3.4 ± 0.1 eV), determined using the Arrhenius plots for the boundary velocity, is indicative of a considerable strength of the adsorbed CO film. Behavior of the CO phase desorbing from the {100}W regions can be consistently explained by assuming that this phase comprises a network of adsorbed CO dipoles oriented perpendicularly to the crystal surface, with the carbon atoms facing vacuum. © *2000 MAIK "Nauka/Interperiodica".*

In this work, we have used the method of field electron microscopy (FEM) to study the process of carbon monoxide adsorption and desorption on a tungsten single crystal. The interest of researchers in such experiments is explained by the possibility of observing the dynamics of desorption with high spatial resolution. Using FEM techniques, it is possible to study various two-dimensional phases formed on the surface of a rounded single crystal point, differing by the type of interatomic (lateral) interactions inside the phase. The attraction between adatoms is typical of some metal adsorbates studied in the systems Zr–W [1], Hf–W [2], Hf–Mo [3], etc., whereas alkali metals with strongly polarized atoms are characterized by repulsion in the adsorbed phase, as reported for Cs on W [4], Na on W [5], etc.

The purpose of this work was to continue with these investigations for the adsorbed films of gases where, in principle, the lateral interactions of both types are possible. It was of special interest to assess the thermal stability of adsorbed films.

The initial adsorbed layer was formed by a 1-h exposure to residual gases in a sealed glass device at room temperature. For a residual vacuum of $\sim 5 \times 10^{-10}$ Torr, this exposure provided an adsorption coating somewhat greater than monolayer coverage. The room-temperature emission pattern did not significantly differ from that observed for a clean tungsten surface (Fig. 1a). Weak heating of this sample (to T = 500 K) results in a typical pattern (Fig. 1b) with a dark oblique cross along the ⟨111⟩ band lines containing faces of the {110}, {112}, and {123} types. According to Wang and Gomer [6], heating an adlayer of CO on W in the temperature interval T = 300–400 K leads to desorption of physically adsorbed CO molecules, leaving only chemisorbed CO on the substrate surface. Similar patterns, accompanied by a significant increase in the work function φ, are typical of the adsorption of many simple gases, including H_2, N_2, CO, H_2O, O_2 [7–11]. However, evolution of the emission patterns during thermostimulated desorption in these systems exhibits individual features. Behavior observed in our case (Figs. 1c–1e) indicates that the adlayer contains CO with an admixture of H_2.

Upon further heating the system from the state depicted in Fig. 1b to T = 640–900 K, the dark cross along the ⟨111⟩ band lines vanishes and a pattern of pseudoclean tungsten surface arises (Fig. 1c). According to Gomer [12], heating to these comparatively low temperatures only leads to the complete desorption of molecular hydrogen from the surface. The Arrhenius plot for this desorption process (Fig. 2a) yields the desorption activation energy $Q_d = 0.49 \pm 0.06$ eV and the preexponential factor $\tau_0 = 8 \times 10^{-2}$ s. The activation energy for molecular hydrogen reported in [12] was $Q_d \approx 1$ eV for coverages in the interval θ = 0.15–0.45 (in monolayer units) and dropped sharply with increasing coverage to reach Q_d = 0.15–0.2 eV for $\theta \geq 0.6$. Thus, in our case the surface coverage of hydrogen can be estimated at $\theta \sim 0.5$.

The further growth of the temperature (T = 1200–1400 K) leads to CO desorption, which is accompanied by a characteristic motion of the film front toward regions around the {001}W cubic faces (Figs. 1d and 1e). Upon reaching the state shown in Fig. 1e, the front ceases to move and the CO adlayer desorbs, which is accompanied by the gradual loss of contrast in the emission pattern. The Arrhenius plot for the CO desorption (Fig. 2b) yields $Q_d = 3.43 \pm 0.05$ eV and $\tau_0 = 4 \times 10^{-12}$ s.

As is well known, CO molecules are mostly adsorbed on the surface of tungsten without dissociation and are desorbed in the same mode. Otherwise,

1063-7850/00/2606-0514$20.00 © 2000 MAIK "Nauka/Interperiodica"

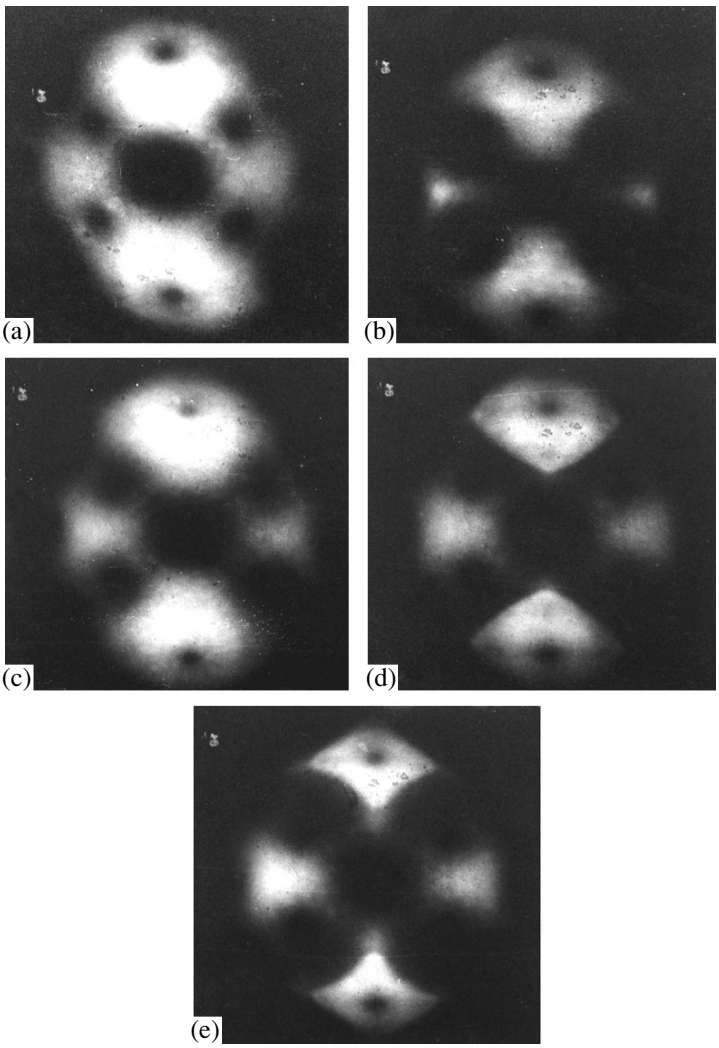

Fig. 1. FEM images of the tungsten point (point radius $r = 0.6$ μm) in the course of residual gas adsorption and desorption: (a) initial clean W surface ($U_{10} = 6350$ V); (b) after 1-h adsorption of residual gases and heating at $T = 500$ K, $t = 15$ s ($U_{10} = 6400$ V); (c) after H_2 desorption at $T = 900$ K, $t = 30$ s ($U_{10} = 6200$ V); (d) after heating to $T = 1265$ K, $t = 100$ s ($U_{10} = 6129$ V); (e) after heating to $T = 1265$ K, $t = 250$ s ($U_{10} = 6100$ V). U_{10} is the voltage necessary to obtain the emission current $i = 10$ nA.

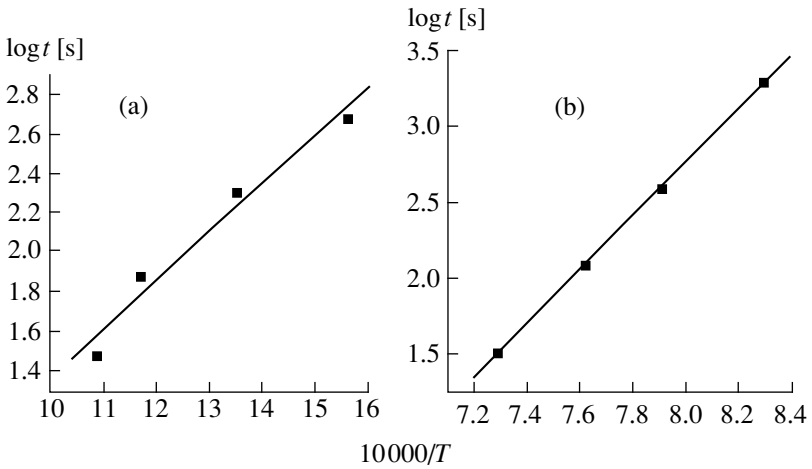

Fig. 2. Arrhenius plots for the thermostimulated desorption of residual gases from tungsten: (a) desorption of H_2 (initial state, Fig. 1b; final state, Fig. 1c); (b) desorption of CO (initial state, Fig. 1d; final state, Fig. 1a).

heating W in a CO atmosphere would lead to carbidization of the metal surface, similar to that observed upon heating W in the vapors of various hydrocarbons. However, not one of the works reported previously on the interaction of CO with W showed evidence of the tungsten carbide formation.

There are two interesting points that are worth noting. First, the film of CO adsorbed in the {001}W regions appears as bright on the emission pattern, which indicates that the adsorbate decreases the work function φ of these W faces. According to Klein [13], the adsorption of carbon monoxide markedly increases the φ value of tungsten, which implies that CO molecules are adsorbed with carbon atoms facing the substrate [14, 15]. However, the results of thermodesorption measurements [6] showed that CO molecules on (001}W may occur in five different states, including the primary adsorbed state (desorbed at T_d = 220 K), physically adsorbed state (T_d = 360 K), and three chemisorbed states β_1, β_2, and β_3 with T_d = 930, 1070, and 1375 K, respectively. All these states, except for β_3, increase the initial φ value of the {001}W face. The high-temperature β_3 state slightly decreases the work function beginning with $T > 820$ K ($\Delta\varphi = -0.1$ eV at $T = 1000$ K) and at $T > 1200$ K the φ value reaches the initial work function level of the {001}W surface. It is this last state, the desorption from which accounts for the weak contrast observed in Figs. 1d and 1e.

The second point to be noted is that, as is readily seen in Figs. 1d and 1e, the desorbing CO film retains a sharp boundary. Therefore, CO behaves as an adsorbate with the attractive lateral interaction. Upon reaching the state imaged in Figs. 1d and 1e, the adsorbate front (representing the regions of {310}–{311} faces) ceases to move and the adlayed desorbs, which is reflected by vanishing of the emission contrast. In these regions, the steps are featuring a transition from the {110} and {112} structures to {100} terraces. Near these terraces, the steps are wider and the molecules (CO dipoles) occur in the potential wells of the substrate at greater distances from each other. In the regions of {310}–{311} faces, the dipoles are closer to each other and may exhibit attractive lateral interactions, mediated by free C–C bonds, exceeding the possible Coulomb repulsion between dipoles. This may explain the existence of a sharp boundary of the adlayer and its motion over the W crystal point surface in these regions. The mutual attraction of dipoles does not conform to the model stipulating their orientation with the carbon atom facing the substrate and the oxygen atom facing vacuum, because this arrangement may feature only repulsive interactions.

In the experiments described above, CO molecules exhibit desorption rather than sublimation from the tungsten surface. This is confirmed by the fact that, after attaining the state corresponding to Fig. 1e, a decrease in the temperature is not accompanied by backward motion of the light front (toward {112} faces and the central {110} face), that is, no two-dimensional condensation takes place. Finally, note that the activation energy of desorption determined in our experiments (3.4 eV) is sufficiently high, which indicates that the CO film is sufficiently strong. Fracturing this film would require the energy to be spent both for the breakage of contacts with the substrate and for the rupture of bonds inside the adlayer.

All the observed features can be consistently interpreted assuming that CO molecules adsorbed on W in the region of ⟨100⟩ poles may form, under certain conditions, a dense network of dipoles oriented perpendicularly to the crystal surface, with the carbon atoms facing vacuum. This dipole layer exhibits a somewhat electropositive character. At the same time, carbon atoms with unsaturated bonds may provide for the attraction between dipoles. On the other hand, the contact of CO molecules with tungsten via oxygen favors their nondissociative desorption. The W–C bond of the carbide type would be stronger than the W–O contact.

This work was supported by the Russian Foundation for Basic Research, project no. 97-02-18066.

REFERENCES

1. G. A. Odishariya and V. N. Shrednik, Dokl. Akad. Nauk SSSR **182**, 542 (1968) [Sov. Phys. Dokl. **13**, 929 (1968)].
2. O. L. Golubev, T. I. Sudakova, and V. N. Shrednik, Zh. Tekh. Fiz. **70** (2000) (in press) [Tech. Phys. **45** (2000) (in press)].
3. V. N. Shrednik, in *Current Problems of Crystallography*, Ed. by B. K. Vaĭnshteĭn and A. A. Chernov (Nauka, Moscow, 1975), pp. 150–171.
4. V. M. Gavrilyuk, A. G. Naumovets, and A. G. Fedorus, Zh. Éksp. Teor. Fiz. **51**, 1332 (1966) [Sov. Phys. JETP **24**, 899 (1966)].
5. E. V. Klimenko and V. K. Medvedev, Fiz. Tverd. Tela (Leningrad) **10**, 1986 (1968) [Sov. Phys. Solid State **10**, 1562 (1969)].
6. C. Wang and R. Gomer, Surf. Sci. **90** (1), 10 (1979).
7. R. Gomer, R. Wortman, and R. Lundry, J. Chem. Phys. **26**, 1147 (1957).
8. R. Worthman, R. Gomer, and R. Lundy, J. Chem. Phys. **27**, 1099 (1957).
9. R. Gomer and J. K. Hulm, J. Chem. Phys. **27**, 1363 (1957).
10. C. Ehrlich and F. G. Hudda, J. Chem. Phys. **35**, 1421 (1961).
11. T. Engel and R. Gomer, J. Chem. Phys. **50**, 2428 (1969).
12. R. Gomer, in *Field Emission and Field Ionization* (Harv. Univ. Press, Cambridge, USA, 1961), pp. 125–126.
13. R. Klein, J. Chem. Phys. **31**, 1306 (1959).
14. T. Madey, J. Czyzewski, and J. T. Yates, Surf. Sci. **57**, 580 (1976).
15. R. J. Behm, K. Christmann, and G. Ert, J. Chem. Phys. **73**, 2984 (1980).

Translated by P. Pozdeev

Technical Physics Letters, Vol. 26, No. 6, 2000, pp. 517–519. Translated from Pis'ma v Zhurnal Tekhnicheskoĭ Fiziki, Vol. 26, No. 12, 2000, pp. 46–50.

Atomic Force Microscope in a Contactless Mode: Peculiarities of Force Interactions

S. Sh. Rekhviashvili

Institute of Applied Mathematics and Automation, Kabardino-Balkarian Scientific Center, Russian Academy of Sciences, Nalchik

Received December 27, 1999

Abstract—Forces of interaction between the atomic force microscope (AFM) probe and the surface of a solid are calculated with an allowance for the induced cantilever oscillations. A continuous approximation used in this work does not take into account discreteness of the sample and probe structures. Calculations have been performed for various AFM point shapes. It is theoretically demonstrated that the cantilever oscillations increase the interaction force. *© 2000 MAIK "Nauka/Interperiodica".*

The atomic force microscope (AFM) is one of the most promising tools in the studies of ultraweak forces and nanostructure technologies. Steadily developing, AFM techniques have reached a high level of perfection [1, 2]. An increase in the resolution is the main task of any applied probe microscopy. Modern AFMs exhibit a force resolution of about 1 pN and a spatial (depth) resolution of about 1 pm. However, the principles of quantum mechanics yield the limiting values of $\sim 10^{-18}$ N and $\sim 10^{-15}$ m, respectively [3]. Modulation methods realized at large scanning distances (exceeding, typically, 0.5 nm) allow one to increase the resolution. In this case the measurements of amplitude, frequency, and phase of cantilever oscillations make it possible to reconstruct the surface topography. This approach minimizes drift, noises, mechanical vibrations, and other negative factors.

Let us consider an oscillatory regime of the cantilever. Figure 1 shows a sine-modulated voltage applied to a piezotube. It can be expected that a probe tip displacement is described by the formula:

$$u(z) = a\cos(kz + w), \tag{1}$$

where a is the amplitude, k is the frequency, and w is the phase of oscillations. In the classical mechanics, a harmonic oscillator is localized in a segment from z to $z + dz$ with a probability $\omega(z)dz$ given by:

$$\omega(z)dz = \frac{1}{\pi a}\frac{dz}{\sqrt{1 - \frac{z^2}{a^2}}}. \tag{2}$$

With an allowance of the distribution function (2), a mean value of the force acting upon a probe can be written as:

$$\langle F\rangle = \int_{-a}^{a} F(|h - z|)\omega(z)dz, \tag{3}$$

where h is the distance between the probe tip and the surface (Fig. 1) and F is the interaction force.

In order to calculate integral (3), it is necessary to know the force as a function of the distance. In calculations, we use a continuous approximation for the van der Waals forces [4]:

$$F = -C\frac{\partial}{\partial h}\iiint\frac{d\Omega}{(z + h)^3}, \quad C = \frac{\hbar\bar{\omega}}{8\pi^2}, \tag{4}$$

with the integration over the probe volume. Here, C is the van der Waals interaction constant for two semi-infinite plates (for characteristic combinations of the probe and sample materials C falls within a narrow interval from 0.01 to 0.1 eV [5]) and $\bar{\omega}$ is a characteristic frequency of the absorption spectrum [6].

Expression (4) is valid provided that the probe dimensions are significantly greater than the scanning

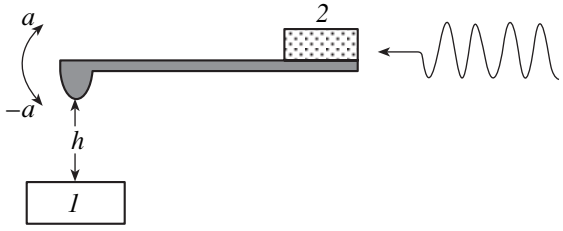

Fig. 1. A schematic diagram of the AFM contact showing (*1*) a sample and (*2*) a piezotube.

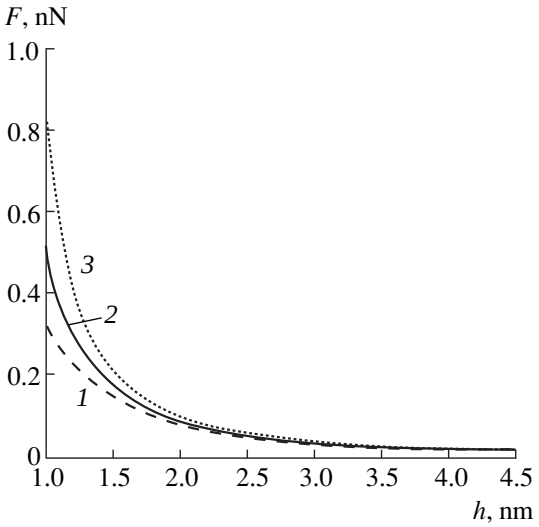

Fig. 2. Plots of the interaction force versus distance calculated (*1*) by formula (5) and (*2*, *3*) by formula (6) with a = 0.5 (*2*) and 0.7 nm (*3*).

distance. For this reason, we did not take into account the Kazimir forces acting upon the cantilever and the mesoscopic part of the probe. Note that the validity of this assumption is restricted to the scanning distances of less than 1.5–2 nm [7]. In addition, we renormalized the van der Waals constant for pairwise atomic interactions according to a rule proposed by Moiseev *et al.* [8].

Upon calculating the integral (4) and making further reasonable simplifications, we obtain the following expression for the point tips of different shapes:

$$F = \frac{A_n}{h^n}, \tag{5}$$

where A_n is a constant depending on the tip shape and the properties of the sample and probe materials, $n = 1$ for a cone and a tetragonal pyramid, $n = 2$ for a hemisphere and a paraboloid of rotation, and $n = 3$ for a circular cylinder. After substituting (2) and (5) in (3) and integrating, we arrive at the following expression for the interaction force:

$$\langle F \rangle = A_n \varphi_n(h), \tag{6}$$

where $\varphi_n(h)$ depends on the geometrical shape of the tip. The results of calculations are summarized in the table, where R_0 is the radius of a hemisphere or a cylinder, r_0 is the paraboloid curvature radius, d is the side of a pyramid base, and z_0 is the height of a cone or a pyramid.

Parameters in formulas (5) and (6)

Probe tip shape	A_n	$\varphi_n(h)$	n
Hemisphere	$\pi R_0 C$	$\dfrac{h}{\sqrt{(h^2 - a^2)^3}}$	2
Paraboloid	$\pi r_0 C$	Same as for hemisphere	2
Cone	$\pi R_0^2 C / z_0^2$	$\dfrac{1}{\sqrt{(h^2 - a^2)}}$	1
Pyramid	$d^2 C / z_0^2$	Same as for cone	1
Cylinder	$\pi R_0^2 C$	$\dfrac{(2h^2 + a^2)}{2\sqrt{(h^2 - a^2)^5}}$	3

Formula (6) is valid for $h^2 > a^2$. This condition is reliably satisfied in a contactless mode at small oscillation amplitudes. It can be easily demonstrated also that (5) follows from (6) for $a^2 \longrightarrow 0$, which corresponds to the case of a static cantilever.

Curves of the interaction force versus distance in Fig. 2 were calculated for a paraboloid probe at C = 0.03 eV (for a SiO_2–SiO_2 contact) and r_0 = 20 nm. It is seen that cantilever oscillations may play a significant role even at large distances (h is about 1 nm) and lead to an increase in the interaction force. The latter causes the known artifacts such as "sticking" of the probe to the sample surface. We arrive at the same conclusion considering a relative deviation of the force described by the formula:

$$\frac{\Delta F}{\langle F \rangle} = \frac{na}{h^{n+1}\varphi_n(h)} \sim \frac{na}{h}. \tag{7}$$

Formula (7) shows that the role of oscillations increases with decreasing distance h. Note that the oscillatory regime appears to be the most critical for a cylindrical probe.

Thus, an important conclusion proceeds from the results of the calculations: a "purely" contactless regime is provided by scanning at small amplitudes of the cantilever oscillations ($a < h/n$).

Finally, note that our results can be used for the precise calibration of AFM prior to force measurements or for the tip shape determination. However, more accurate calculations imply the knowledge of the dependence of amplitude, frequency, and phase on the scanning distance. Analysis of these and related problems will follow.

REFERENCES

1. V. S. Édel'man, Prib. Tekh. Éksp., No. 5, 25 (1989).
2. V. S. Édel'man, Prib. Tekh. Éksp., No. 1, 24 (1991).
3. S. Sh. Rekhviashvili and G. V. Dedkov, in *Proceedings of the Scientific Seminar Noise and Degradation Processes in Semiconductor Devices (Metrology, Diagnostics, and Technology)"* (Mosk. Nauch.-Tekh. O–vo Radioélektr. Svyazi im. A. S. Popova, Mosk. Énerg. Inst., Moscow, 1998), pp. 205–209.
4. U. Hartmann, Phys. Rev. B **42**, 1541 (1990).
5. H. Buttner and E. Gerlach, Chem. Lett. **5** (2), 91 (1970).
6. E. M. Lifshitz and L. P. Pitaevskiĭ, *Statistical Physics* (Nauka, Moscow, 1978).
7. G. V. Dedkov and S. Sh. Rekhviashvili, Zh. Tekh. Fiz. **69** (8), 124 (1990) [Tech. Phys. **44**, 982 (1999)].
8. Yu. M. Moiseev, V. M. Mostepanenko, V. I. Panov, *et al.*, Zh. Tekh. Fiz. **60** (1), 141 (1990) [Sov. Phys. Tech. Phys. **35**, 84 (1990)].

Translated by A. Chikishev

Technical Physics Letters, Vol. 26, No. 6, 2000, pp. 520–522. Translated from Pis'ma v Zhurnal Tekhnicheskoĭ Fiziki, Vol. 26, No. 12, 2000, pp. 51–57.

Hydroxyl Groups and *a*-C:H and *a*-C:H(Me) Structures

V. I. Ivanov-Omskiĭ

Kurchatov Institute of Atomic Energy

Ioffe Physicotechnical Institute, Russian Academy of Sciences, St. Petersburg, 194021 Russia

Received February 11, 2000

Abstract—IR absorption spectra of hydroxyl groups in *a*-C:H and *a*-C:H(Me) (Me = Cu, Co) films grown by magnetron cosputtering of graphite and metal targets in argon–hydrogen plasma were studied. The hydroxyl band shape was analyzed using published data on the dependence of the O–H stretching vibration frequency on the distance from the nearest oxygen atom. It is demonstrated that the hydroxyl band shape is related to the character of interaction between an encapsulated metal and a carbon backbone of the film. © *2000 MAIK "Nauka/Interperiodica"*.

Hydrogenated amorphous carbon films are widely used as coatings, including antireflection and protective layers in solar power engineering [1, 2]. The presence of hydroxyl groups inside hydrogenated amorphous carbon (*a*-C:H) structure is assumed to be related to shortcomings of the synthesis methods. Ultrahigh vacuum (about 10^{-9} Torr) treatment or aftergrowth annealing are usually employed so as to eliminate this impurity. The problem is that a characteristic absorption band of hydroxyl groups decreases optical transparency of the *a*-C:H films in the spectral interval of 3–4 μm. We will demonstrate, however, that the presence of hydroxyls in *a*-C:H and, especially, *a*-C:H(Me) films makes it possible to characterize the film structures. We have studied the IR absorption spectra of hydroxyl groups in *a*-C:H and *a*-C:H(Me) (Me = Cu, Co) films in the region of O–H stretching vibrations. The films were grown by magnetron cosputtering of graphite and metal targets. Growth methods are described in details elsewhere [3].

Figure 1 shows the region of vibrational bands of hydroxyl groups (3100–3700 cm^{-1}) in the absorption spectra of *a*-C:H, C:H(Cu) (atomic composition, 30% Cu and 70% C) and *a*-C:H(Co) (atomic composition, 40% Co and 60% C) films. All the spectra exhibit a broad hydroxyl band and a more or less developed discrete structure, typical of chemical substances of the hydrate type rather than of disordered structures such as *a*-C:H. Note the evolution of the hydroxyl band shape and structure in a series of *a*-C:H, *a*-C:H(Cu), and *a*-C:H(Co). The bands exhibit asymmetric shape, inhomogeneous structure, and a growth of the integral intensity in the above order. It is likely that a metal favors an increase in the hydroxyls concentration. An explicit heterogeneity of the band in the case of *a*-C:H(Co) can be related to the formation of hydrates of a metastable cobalt carbide [4]. Note that Fig. 1 displays a unique spectrum with the most clearly resolved structural elements that are much less pronounced in most of the measurements. One can assume that the character of metal–carbon interaction determines the hydroxyl band structure and intensity. Then a lower

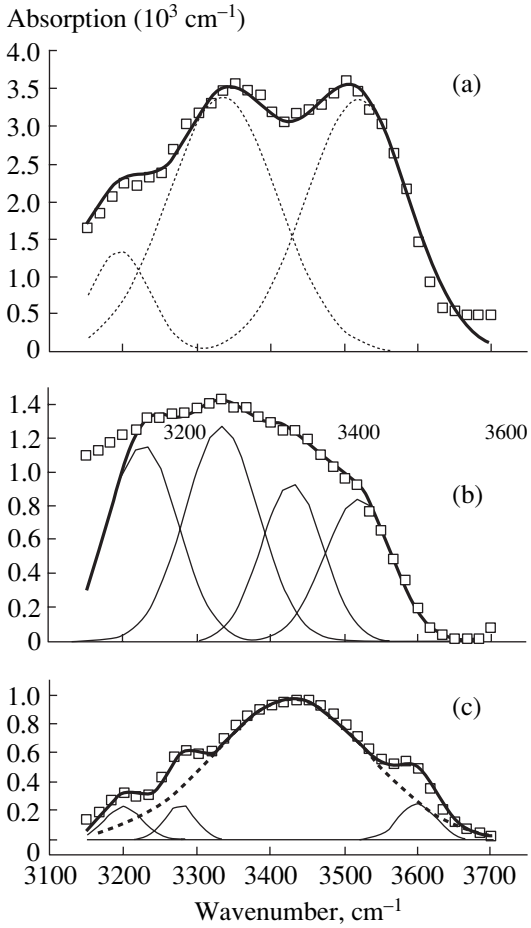

Fig. 1. Absorption bands of hydroxyl groups in the IR spectra of (a) *a*-C:H, (b) *a*-C:H(Cu), and (c) *a*-C:H(Co). Dashed and thin solid lines shows individual Gaussian components (see table for the parameters) and thick solid lines shows the sums of Gaussian components.

1063-7850/00/2606-0520$20.00 © 2000 MAIK "Nauka/Interperiodica"

intensity of the hydroxyl band in the case of *a*-C:H(Cu) agrees well with the facts that copper does not form stable carbides and its interaction with carbon is characterized by small binding energy [5]. Deconvolution of the bands into Gaussian components (Fig. 1) allowed us to perform a more detailed comparison of band shapes in all the three cases. Reconstruction of the bands by summing up the corresponding components was used to check for the accuracy of the fitting procedure. Parameters of the Gaussian components are summarized in the table. It is seen that the band structure of the second sample (encapsulated copper) can be fitted with nearly the same Gaussian components as that of the third sample (encapsulated cobalt), except for the additional component at approximately 3440 cm^{-1}. The latter coincides with the main component in the spectrum of *a*-C:H. Note, however, that the spectrum of *a*-C:H(Co) exhibits a spectral feature at this wavenumber that can be related to a weak band masked by strong absorption. For this reason, we can assume that a spectral component at ~3440 cm^{-1} belongs to a hydroxyl group typical of *a*-C:H itself, while all the other spectral features of the hydroxyl band emerge due to interaction with an encapsulated metal.

To elucidate the nature of peculiarities in the hydroxyl band structure, we used an excellent collection [6] of the optical and crystallographic data on the O–H stretching frequency dependence on the distance *d* from hydroxyl to the nearest oxygen atom that exchanges protons with the given hydroxyl group in the course of H-bond formation. Figure 2 shows a part of these data in a spectral interval corresponding to the *a*-C:H absorption band. It is seen that the experimental data can be well approximated by a function

$$d(\text{Å}) = 2.71 + 0.01\exp\left(\frac{WN - 3000}{160}\right), \qquad (1)$$

where *WN* is the wave number (in cm^{-1}) and *d* is the distance (in angstroms) to the nearest oxygen atom (ion). The quantity 2.71 Å approximately equals a doubled radius of a doubly charged oxygen ion and corresponds to the closest packing of oxygen.

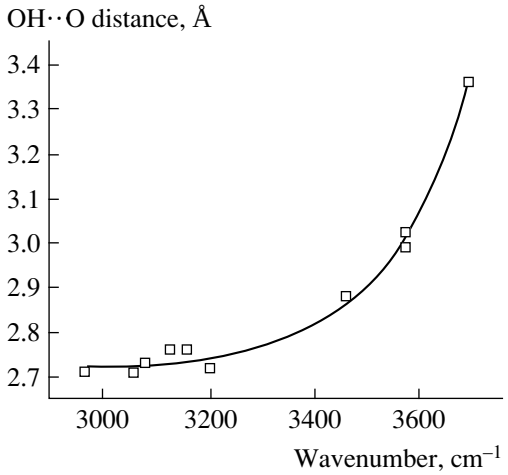

Fig. 2. Plot of the distance between a hydroxyl group and the nearest oxygen atom (H-bond length) versus the component wave number in the hydroxyl band contour: experimental data from [6] (squares) and the results of calculation by operation (1) (solid line).

Let us analyze the absorption band shapes of hydroxyl groups in *a*-C:H-based structures using equation (1). Assume that the oscillator strength of the O–H stretching mode does not change upon introduction of a metal. Then, the absorption coefficient $\alpha(WN)$ is proportional to the density of hydroxyls in the film: $\rho(\text{OH}) \sim \alpha(WN)$. Equation (1) relates the wave numbers *WN* of the hydroxyl band components to distances *d* between hydroxyl groups and the nearest H-bonded oxygen atoms. This transformation yields a distribution function of hydroxyls with respect to the H-bond length or the relative density of hydroxyl groups as a function of *d* (Fig. 3). A similar calculation relates Gaussian

Parameters of the Gaussian components (see spectra in Fig. 1)

Substance	Number of band	*WN*, cm^{-1} (wavenumber)	ΔW, cm^{-1} (bandwidth)	Integral intensity, 10^4 cm^{-2}	*d*, Å
a-C:H	1	3200	50	1.4	2.745
″	2	3280	50	1.2	2.77
″	3	3430	250	25.6	2.86
″	4	3590	50	1.6	3.11
a-C:H(Cu)	1	3220	100	13	2.75
″	2	3330	116	16	2.79
″	3	3430	100	9.7	2.86
″	4	3520	116	9.6	2.97
a-C:H(Co)	1	3200	82	11.7	2.745
″	2	3330	183	63.4	2.79
″	3	3520	184	59.5	2.97

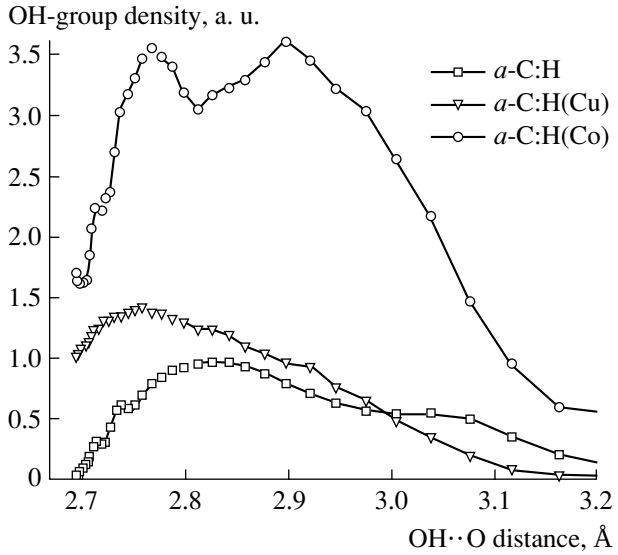

Fig. 3. Plots of the density of H-bonded hydroxyl groups versus the H-bond length *d* (distance between hydroxyl group and oxygen) for *a*-C:H (squares); *a*-C:H(Cu) (triangles); *a*-C:H(Co) (circles).

components (see table) to the corresponding H-bond lengths. Thus, the absorption band shape of hydroxyl groups appears to be determined by their distribution with respect to the parameter *d* related to the internal structure of *a*-C:H and *a*-C:H(Me) films.

Oxygen atoms and hydroxyl groups form H-bonds of various lengths which results (see table and Fig. 3) in a broad hydroxyl band. A correlation in the mutual arrangement of oxygen atoms in the film structure, showing two special mean distances of 2.86 and 3.11 Å accounts for the asymmetric band in the *a*-C:H spectrum. All the samples exhibit an O–O distance of 2.86 Å (corresponding to a spectral feature at 3430 cm^{-1}) that is likely to be an essential characteristic of the *a*-C:H structure grown by the magnetron sputtering of graphite. In addition, clearly manifested are the oxygen pairs with interatomic distances of 2.74 and 2.77 Å coinciding with the distances between oxygen atoms in hexagonal and less symmetric ice phases, respectively [7]. Metal-free films contain isolated oxygen atoms (at a distance of about 3.1 Å from each other), whereas introduction of a metal facilitates the formation of structures with higher density of hydroxyl groups. The *a*-C:H(Me) structures exhibit a minimum distance of 2.71 Å corresponding to the closest packing of doubly charged oxygen ions.

Of special interest is the possibility of detecting hydroxyl groups at a mean distance between the nearest oxygen ions of ~2.9 Å typical of liquid water. The plots in Fig. 3 indicate that such groups are virtually absent in *a*-C:H, appear in *a*-C:H(Cu), and significantly contribute to the *a*-C:H(Co) structure. Therefore, the analysis of the IR spectra indicates that no liquid water is present in the pores of *a*-C:H grown by magnetron sputtering of graphite and yields a chaotic distribution of hydroxyl groups inside this structure (which follows from a large width of the band at 3430 cm^{-1}). However, it does not rule out the formation of small amounts of ice in the pores. The metal containing structures exhibit traces of liquid water: the stronger the interaction of metal with the carbon backbone, the higher the water content inside the structure.

The authors are grateful to T.K. Zvonareva for growing the films and to G.S. Frolova for spectral measurements.

REFERENCES

1. J. Robertson, Adv. Phys. **35**, 317 (1986).
2. G. A. Dyuzhev, V. I. Ivanov-Omskiĭ, E. K. Kuznetsova, *et al.*, Mol. Cryst. Liq. Cryst. Sci. Technol., Sect. C **8**, 103 (1996).
3. T. K. Zvonareva, V. I. Ivanov-Omskiĭ, A. V. Nashchekin, and L. V. Sharonova, Fiz. Tekh. Poluprovodn. (St. Petersburg) **34**, 96 (2000) [Semiconductors **34**, 98 (2000)].
4. Y. M. Yu Liu and D. J. Sellmyer, J. Appl. Phys. **85**, 4319 (1999).
5. V. I. Ivanov-Omskiĭ and É. A. Smorgonskaya, Fiz. Tekh. Poluprovodn. (St. Petersburg) **32**, 931 (1998) [Semiconductors **32**, 831 (1998)].
6. K. Nakomoto, M. Matgoshes, and R. E. Rundle, J. Am. Chem. Soc. **77**, 6480 (1955).
7. P. V. Hobs, *Ice Physics* (Clarendon Press, Oxford, 1974).

Translated by A. Chikishev

Technical Physics Letters, Vol. 26, No. 6, 2000, pp. 523–525. Translated from Pis'ma v Zhurnal Tekhnicheskoĭ Fiziki, Vol. 26, No. 12, 2000, pp. 58–63.

Effects of Molecular Hydrogen, Water Vapor, and High Vacuum on the Conductivity and Magnetic Properties of Lanthanum–Calcium Manganite in the 78–300 K Temperature Range

Yu. M. Baĭkov, E. I. Nikulin, B. A.-T. Melekh, Yu. P. Stepanov, and Yu. N. Filin

Ioffe Physicotechnical Institute, Russian Academy of Sciences, St. Petersburg, 194021 Russia

Received February 2, 2000

Abstract—The conductivity and magnetoresistance in a magnetic field of 0.5 T were studied for the first time in fused samples of a $La_{0.67}Ca_{0.33}MnO_{3-\alpha}$ composition with variable oxygen nonstoichiometry ($0.3 \geq \alpha \geq 0$) modified by exposure to H_2, H_2O vapor, and high vacuum (10^{-4} Pa). © *2000 MAIK "Nauka/Interperiodica".*

Now, it is commonly accepted that the ratio of ions $Mn^{4+}/Mn^{3+}/Mn^{2+}$ is the main parameters determining the effect of colossal negative magnetoresistance (CMR) observed in solid solutions of lanthanum and alkali metal manganite [1]. Equilibrium between various charged states $2Mn^{3+} \Leftrightarrow Mn^{2+} + Mn^{4+}$ may shift to either side upon changing the cation composition and/or oxygen content in the system.

For a particular series of solid solutions such as $La_{1-x}Ca_xMnO_{3-\alpha}$, the ratio of three charged forms of manganese $y_4(Mn^{4+}) : y_3(Mn^{3+}) : y_2(Mn^{2+})$ can be determined with an allowance for three factors, including the trivial relationship $y_4 + y_3 + y_2 = 1$ and the conditions of electroneutrality and thermodynamic equilibrium. Assuming the solid solution containing manganese ions to be ideal and taking into account the charges of other ions (La^{3+}, Ca^{2+}, O^{2-}), we obtain the following expression for the fraction of Mn^{4+} ions:

$$y_4 = 0.5\{4K + d(4K-1) - [4K - d^2(4K-1)]^{1/2}\}(4K-1)^{-1}, \quad (1)$$

where K is the equilibrium constant for the charged forms of manganese ions and $d = x - 2\alpha$; the fraction of Mn^{2+} is determined as $y_2 = y_4 - d$. Equation (1) shows that, at a constant temperature (K = const), all members of a series of lanthanum–calcium manganite solutions with equal d will possess the same values of y_4. The electrical and magnetic properties of manganite being determined to a considerable extent by the content of Mn^{4+}, we may expect that the characteristics of compounds in the above series with the same d values will be sufficiently close even despite having different x and α parameters. In particular, the end member of this series, $LaMnO_3$ ($x = \alpha = 0$) with $d = 0$ may form a solid solution with $x > 0$, nonstoichiometric with respect to oxygen ($\alpha = x/2 > 0$).

In this work, we have compared the properties of compounds $LaMnO_3$ and $La_{0.67}Ca_{0.33}MnO_{2.84 \pm 0.01}$ with respect to the temperature variation of electric conductivity (resistance) and magnetoresistance measured in the range from 78 to 300 K. The oxygen nonstoichiometry parameter α was modified, at a constant cation composition, by exposure to molecular hydrogen. The extraction of oxygen from oxide under the action of hydrogen proceeds under the conditions markedly softer than those accompanying the thermovacuum treatments. It was also of interest to study the intercalation of protons into the lattice, which can be effected, in principle, by reactions with both H_2 and H_2O (vapor), although we will restrict consideration in this paper to the latter factor. Methods employed for the H_2 and H_2O vapor treatments and the corresponding analytical procedures were described elsewhere [3]. The experimental conditions are given in the table. In the case of hydrogen intercalation, the d value changes as described by the formula $d = x - 2\alpha - h$, where h is the number of incorporated protons per formula unit ($La_{1-x}Ca_xMnO_{3-\alpha}H_h$).

The initial materials were $La_{0.67}Ca_{0.33}MnO_{2.70}$ (see table, sample 5) and $LaMnO_3$ (sample 7) synthesized by the method of induction melting in "cold" crucible [2]. The ingot (15–20 mm in size) was cut into samples with the dimensions $2 \times 2 \times 5$ mm. The measurements were performed on a sample placed inside a massive copper cylinder, the temperature of which was slowly varied from room temperature down to 78 K. The temperature was measured with a copper–constantan thermocouple. The sample resistance was determined by a dc four-point-probe technique. The magnetic measurements were performed by placing samples between the poles of an electromagnet generating a magnetic field

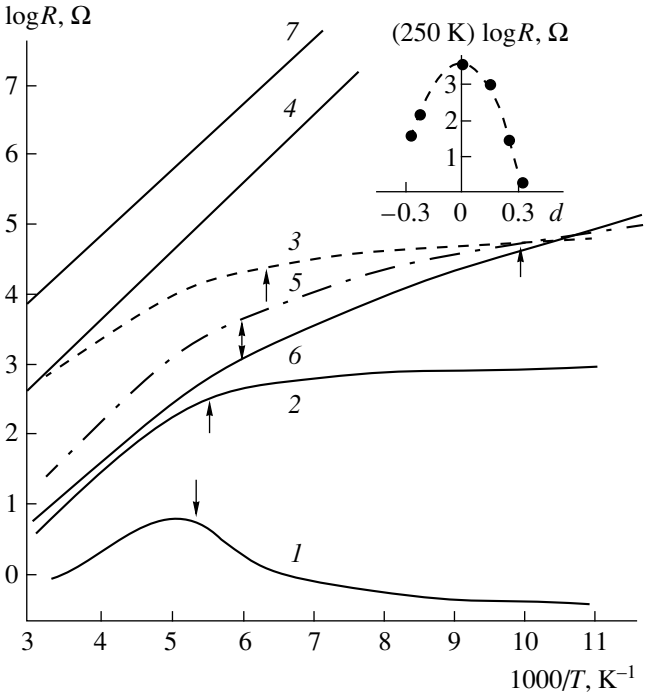

Fig. 1. Temperature variation of the resistance R (numbers at the curves correspond to sample numbers in the table). Arrows indicate positions of the maximum CMR effect in Fig. 2. The inset shows $R(d)$ at 250 K. The dimensionality factor for all samples is 10 cm^{-1}.

with a strength of 0.5 T. The magnetoresistance was determined as the relative difference of resistances with (R_H) and without ($R_{H=0}$) applied magnetic field: $MR = 100(R_{H=0} - R_H)/R_{H=0}$ (%).

The results of our experiments are presented in Figs. 1 and 2.

The data obtained confirmed validity of the above considerations concerning possible similarity in the behavior of samples with equal d values. Indeed, both studied compounds ($LaMnO_3$ and $La_{0.67}Ca_{0.33}MnO_{2.84\pm0.01}$) having equal $d = 0$ exhibit no dependence of the sample resistance R on the magnetic field strength and are characterized by the same trends in R(T) in the temperature rage studied (78–300 K), which is represented by a straight line in the coordinates of $\log R$ versus T^{-1}. This behavior is markedly different from the shape of $R(T)$ in other samples, which exhibits clear variations in the region of the magnetic phase transition (arrows at the curves *1–3*, *5*, and *6* in Fig. 1 correspond to the maximum MR in Fig 2, the latter being attributed to T_c [1]). Neglecting this correlation, we might speak of a transition from intrinsic to impurity conductivity in samples 2, 3, 5, and 6. However, the fact of negative CMR is evidence in favor of the transition from conductivity in a disordered system occurring in the paramagnetic state to conductivity of the ordered system in the ferromagnetic state.

The inset in Fig. 1 shows a typical dependence of the resistance on the parameter d for La–Ca manganite samples, plotted in the coordinates of $\log R$ versus d at 250 K. The curve exhibits a clear extremal character, similar to that observed in complex oxide systems with variable oxygen content during the transition from conductivity of the *p*-type at a high partial oxygen pressure to that of the *n*-type at a low oxygen pressure [4]. Judging by the sign of thermo emf, samples 1 and 3 possess room-temperature conductivity of the *p*-type, while samples 5 and 6 belong to the *n*-type. We failed to unambiguously determine the thermo emf sign in samples 3 and 4. Nevertheless, we may suggest that a paramagnetic phase of $La_{0.67}Ca_{0.33}MnO_{3-\alpha}$ with $d > 0$ has a conductivity of the *p*-type, while $d = 0$ corresponds to the intrinsic conductivity and $d < 0$, to conductivity of the *n*-type (for all samples above 250 K, $E_g = 0.4 \pm 0.1$ eV).

As for the behavior of MR as function of the parameter d, we note two special features. The first refers to the magnitude of the CMR effect. Samples 5 and 6 with

Regimes of treatment and compositions of $La_{1-x}Ca_xMnO_{3-\alpha}H_h$ samples

No.	Initial sample*	Treatment conditions		x	Parameters upon treatment		
		gas phase (pressure, Pa)	temperature, K		α	h	d
1	5	O_2, 40	1000	0.33	0	0	0.33
2	1	H_2O, 8	520	0.33	0	0.1	0.23
3	1	H_2, 1	850	0.33	0.09	0	0.15
4	1	H_2, 2	850	0.33	0.16	0	0
5		As synthesized		0.33	0.27	0	–0.21
6	5	Vacuum (10^{-6} Torr)	1000	0.33	0.30	0	–0.27
7		As synthesized		0	0	0	0

* Number of the initial sample treated as indicated in the third column to acquire parameters indicated in the last three columns.

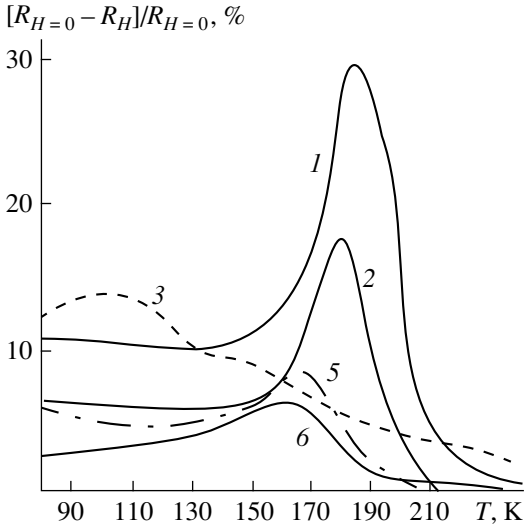

Fig. 2. Temperature variation of the relative magnetoresistance $MR = 100(R_{H=0} - R_H)/R_{H=0}$ (%) (numbers at the curves correspond to sample numbers in the table).

the *n*-type conductivity exhibit a markedly lower CMR in the maximum (6 and 8%, respectively) as compared to that observed in samples 1–3 belonging to the *p*-type (28, 18, and 14%, respectively). The second feature is related to the temperature variation of CMR in a sample with $\alpha = 0.09$ obtained upon the extraction of oxygen by treating with molecular hydrogen. Here, the *MR* maximum was shifted by 85 K and the curve exhibited a broad temperature intervals of large *MR* values (note: a decrease in the *MR* value to 5% at $T > T_{max}$ is reached in sample 1 when the temperature changes by 25 K, while in sample 3 the same decrease is observed only after 90 K). Apparently, this possibility of "controlling" the CMR affect may be used in applications.

From the standpoint of CMR as a fundamental problem, it is interesting to consider the temperature variation of *MR* in sample 2 which, being stoichiometric with respect to oxygen, contains incorporated protons ($\alpha = 0$, $h = 0.1$). Note that the behavior of *MR* in this sample is similar to that in sample 1 ($\alpha = 0$, $h = 0$), but differs from the pattern observed for sample 3 ($\alpha = 0.09$, $h = 0$).

In concluding, it should be emphasized that the combination of thermochemical factors used in this work, including molecular hydrogen and water vapor, has proved to offer an effective means of controlling the properties of the lanthanum–calcium manganite solid solutions with constant cation composition.

The authors are grateful to N.F. Kartenko for the X-ray diffraction analysis of samples.

This work was supported by the Russian Foundation for Basic Research, project no. 97-03-33466a.

REFERENCES

1. É. D. Nagaev, Usp. Fiz. Nauk **166**, 833 (1996) [Phys. Usp. **39**, 781 (1998)].
2. B. A.-T. Melekh, Yu. N. Filin, V. I. Bakharev, *et al.*, in *Proceedings of the IV International Conference "Crystals: Growth, Properties, Real Structure, Application", VNIISIMS, Aleksandrov, 1999*, Vol. 1, pp. 162–165.
3. Yu. M. Baĭkov, Zh. Neorg. Khim. **43** (1), 27 (1998).
4. V. M. Smyth, Prog. Solid State Phys. **15**, 145 (1984).

Translated by P. Pozdeev

Technical Physics Letters, Vol. 26, No. 6, 2000, pp. 526–527. Translated from Pis'ma v Zhurnal Tekhnicheskoĭ Fiziki, Vol. 26, No. 12, 2000, pp. 64–69.

Optimal Control of Particle Motion by Means of a Random Force

A. P. Nikitin

Saratov State University, ul. Universitetskaya 42, Saratov, 410601 Russia

Received December 29, 1999

Abstract—The overdamped motion of a particle controlled by a time-correlated random force in a spatially periodic potential is studied theoretically. The correlation time of the force is essentially assumed to be much greater than the time required for the particle to traverse one period of the potential. It is demonstrated that a bimodal distribution of the force optimizes the control for power demand. © *2000 MAIK "Nauka/Interperiodica".*

The rate of state change of a random process is often characterized by a correlation time, τ_c, as well as by the predictable time interval: for certain types of noise, a large τ_c indicates that the state changes slowly. This paper addresses the problem of the one-dimensional motion of a particle in a spatially periodic potential $dV(x)$ [1–12] under the overdamping conditions:

$$\dot{x} = -\frac{dV(x)}{dx} + \eta(t), \tag{1}$$

where x is the particle coordinate and $\eta(t)$ is a random force. Let $\eta(t)$ be a very slow ergodic process. Then we can use the adiabatic approximation (also known as the quasi-static approximation [10]). In the context of solving equation (1), the idea of the approach is as follows. Suppose that the particle has traversed several periods of $V(x)$, shown in Fig. 1, during an observation time τ_o ($\tau_o < \tau_c$). Let the random force $\eta(t)$ vary so slowly that the probability for $\eta(t)$ to change appreciably during τ_o is negligibly small. Then the resultant total velocity ν of the particle is obtained by calculating the mean velocity $\nu_\tau(\eta)$ over the time τ_o as a function of η, followed by averaging $\nu_\tau(\eta)$ over the values of η assuming that the force η has a stationary distribution $P(\eta)$.

Instead of averaging the velocity over the observation time τ_o, it may be convenient to take the velocity ν_T averaged over time T required for the particle to traverse one spatial period of $V(x)$, which simplifies the computation. Note that $\nu_\tau(\eta)$ tends to coincide with ν_T for $\tau_c \longrightarrow \infty$, i.e., in the limit of the infinitely slow variation of the noise $\eta(t)$. Indeed,

$$\lim_{\tau_o\to\infty}\nu_\tau = \lim_{\tau_o\to\infty}\frac{1}{\tau_o}\int_0^{\tau_o}\frac{dx(t)}{dt}dt = \lim_{\tau_o\to\infty}\frac{x(\tau_o)-x(0)}{\tau_o}$$
$$= \lim_{n\to\infty}\frac{nL+\Delta x}{nT+\Delta t} = \frac{L}{T} = \frac{1}{T}\int_0^{T}\frac{dx(t)}{dt}dt = \nu_T, \tag{2}$$

where L is the length of one spatial period, $\Delta x \in [0, L)$, $\Delta t \in [0, T)$, and n is a nonnegative integer. Thus, the adiabatic approximation enables one to reduce calculating ν to determining ν_T as function of η.

We aim to answer the following question: what stationary distribution must have the random force in order to provide for the energetically optimum control over the particle motion? In other words, we seek to maximize the resultant mean particle velocity at a minimum intensity of the force.

To this end, we derive and analyze an expression for the average velocity ν as function of the parameters characterizing the distribution $P(\eta)$ and the potential $V(x)$. The analytical solution to equation (1) is obtained in this study under the following assumptions.

Assumption 1. The potential $V(x)$ is a piecewise linear function:

$$V(x) = \begin{cases} a(x - Ln), & Ln < x < L(n + b/(a + b)); \\ -b(x - L(n + 1)), & L(n + b/(a + b)) < x < L(n + 1), \end{cases} \tag{3}$$

where $a > 0$, $b > 0$, and $n = 0, \pm1, \pm2, \ldots$. Note that a and b characterize the asymmetry of $V(x)$ and that $V(x) = V(L + x)$.

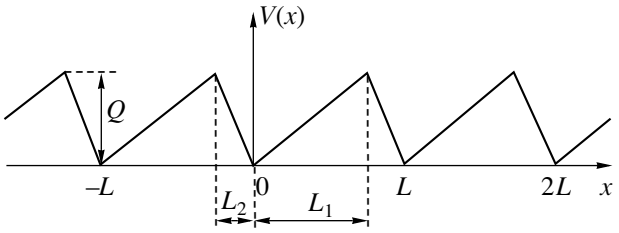

Fig. 1. Piecewise linear periodic potential $V(x)$: L is the period, L_1 and L_2 are the length of the low and high slope portions, Q is the barrier height, where $a = Q/L_1$ and $b = Q/L_2$.

1063-7850/00/2606-0526$20.00 © 2000 MAIK "Nauka/Interperiodica"

Assumption 2. The distribution $P(\eta)$ is symmetric and defined as

$$P(\eta) = \begin{cases} \alpha\eta + 1/(2A) - \alpha A/2, & \eta \geq 0; \\ -\alpha\eta + 1/(2A) - \alpha A/2, & \eta < 0, \end{cases} \quad (4)$$

where A is the amplitude of η and α is a parameter such that $-1/A^2 < \alpha < 1/A^2$. If $\alpha < 0$, then $P(\eta)$ is a unimodal distribution. If $\alpha > 0$, then $P(\eta)$is a bimodal distribution. If $\alpha = 0$, then $P(\eta)$ is a uniform distribution.

Assumption 3. The correlation time τ_c of the random force η is much greater than the time T required for the particle to travel over a potential period. An exception is the case where the particle cannot move over the potential barriers; then we set $\nu = 0$.

Assumption 3 enables us to solve the problem within the adiabatic approximation. Based on an analytical solution of (1), we obtain

$$\nu = \begin{cases} 0, \quad A < a; \\ \alpha((A^3 - a^3)/3 - abA + a^2 b \\ + ab(b-a)\ln|(A+b-a)/b|) \\ + (1/(2A) - \alpha A/2)(A^2/2 - a^2/2 \\ - ab\ln|(A+b-a)/b|), \quad a < A < b; \\ \alpha(b^3/3 - a^3/3 - ab^2 + a^2 b) \\ + (1/A - \alpha A)(b^2 - a^2)/4 \\ + \alpha ab(b-a)\ln|(A+b-a)(-A+b-a)/(ab)| \\ + (1/A - \alpha A)ab\ln|(-A+b-a)b/(A+b-a)/a|)/2, \\ b < A. \end{cases} \quad (5)$$

Expressions (5) suggest the following conclusions:

(1) The resultant mean speed ν is independent of L (due to the adiabatic condition).

(2) There is a maximum value of ν as a function of the force intensity σ_η (see Fig. 2). Here, $\sigma_\eta = \sqrt{D}$, where D is the second moment of $P(\eta)$.

(3) The maximum value of ν monotonically rises with α.

(4) The maximum maximorum value of ν is attained with a bimodal distribution ($\alpha = 1/A^2$).

(5) Characterized by $K = \nu/\sigma_\eta$, the conversion of noise energy η into controlled particle motion is most efficient if the distribution is bimodal ($\alpha = 1/A^2$).

The last conclusion implies that a bimodal distribution optimizes the control from the energetic standpoint, provided the correlation time of the random force is sufficiently large.

We think that the results of this study could be applied to macroscopic directed transport of particles in the absence of a constant gradient of external forces [11–14].

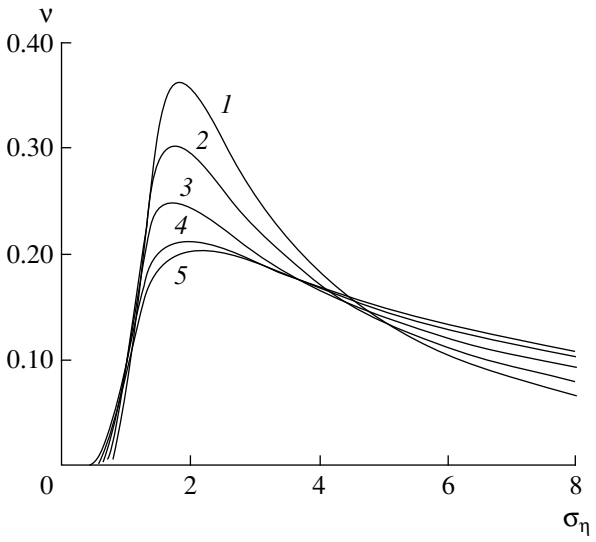

Fig. 2. Resultant mean speed of the particle vs. random force intensity at $L = 2\pi$; $a = 1$; $b = 2$; and $\alpha = 1/A^2$ (*1*), $1/(2A^2)$ (*2*), 0 (*3*), $-1/(2A^2)$ (*4*), or $-1/A^2$ (*5*).

This study was carried out under the auspices of the Ministry of High Education of the Russian Federation (Basic Natural Sciences Program, project no. 97-0-8.3-47).

REFERENCES

1. M. Magnasco, Phys. Rev. Lett. **72**, 2656 (1994).
2. Ch. R. Doering, W. Horsthemke, and J. Riordan, Phys. Lett. **72**, 2984 (1994).
3. R. D. Astumian and M. Bier, Phys. Rev. Lett. **72**, 1766 (1994).
4. M. Bier, Phys. Lett. A **211**, 12 (1996).
5. A. P. Nikitin, Izv. Vyssh. Uchebn. Zaved. PND **5** (1), 30 (1997).
6. D. É. Postnov, A. P. Nikitin, and V. S. Anishchenko, Pis'ma Zh. Tekh. Fiz. **22** (9), 24 (1996) [Tech. Phys. Lett. **22**, 352 (1996)].
7. A. P. Nikitin and D. É. Postnov, Pis'ma Zh. Tekh. Fiz. **24** (2), 47 (1998) [Tech. Phys. Lett. **24**, 61 (1998)].
8. P. S. Landa, Izv. Vyssh. Uchebn. Zaved. PND **6** (5), 3 (1998).
9. A. N. Malakhov, Pis'ma Zh. Tekh. Fiz. **24** (21), 9 (1998) [Tech. Phys. Lett. **24**, 833 (1998)].
10. R. L. Stratonovich, in *Selected Problems in the Theory of Fluctuations in Radio Engineering* (Sov. Radio, Moscow, 1961).
11. L. P. Faucheux, L. S. Bourdieu, P. D. Kaplan, and A. J. Libchaber, Phys. Rev. Lett. **74**, 1504 (1995).
12. L. Gorre-Talini and P. Silberzan, J. Phys. I, No. 7, 1475 (1997).
13. L. Gorre-Talini and P. Silberzan, Phys. Rev. E **56**, 2025 (1997).
14. R. D. Astumian, Science **276**, 917 (1997).

Translated by A. Sharshakov

Technical Physics Letters, Vol. 26, No. 6, 2000, pp. 528–530. Translated from Pis'ma v Zhurnal Tekhnicheskoĭ Fiziki, Vol. 26, No. 12, 2000, pp. 70–75.

Anomalous Temperature Dependence of the Cavitational Strength of Water

A. S. Besov and D. N. Pokrovskiĭ

Lavrentiev Institute of Hydrodynamics, Siberian Division, Russian Academy of Sciences, Novosibirsk, 630090 Russia

Received January 10, 2000

Abstract—It is experimentally demonstrated for the first time that the temperature variation of the cavitational strength of water exhibits an extremal character with a minimum at 35–40°C and a maximum near 50°C. The further increase in the temperature is accompanied by decreasing cavitational strength and increasing absorption of the shock waves. A mechanism explaining this phenomenon is proposed, which is based on the concept of microscopic gas bubbles retained by convective flows, the velocity of which grows linearly with the temperature and exceeds the velocity of equilibrium bubble flotation at 50°C. © *2000 MAIK "Nauka/Interperiodica".*

Experimental data available on the temperature dependence of the cavitational strength of water are rather contradictory. For example, the curve of ultimate negative pressure versus temperature presented in [1] exhibits an extremal character with a maximum near 15°C, while the dependence reported in [2] is linear, and that in [3]—nonlinear but monotonically decreasing. These discrepancies are apparently explained by imperfect methods used in the early works and can be removed only by correct independent experiments. We have selected a capacitance technique [4] reflecting integral dynamics of the whole cavitation cluster, with a maximum error of the cavitation threshold determination not exceeding 8–10%. The method is applicable even for the study of cavitational processes in nontransparent suspensions [5].

Figure 1 shows a schematic diagram of the experimental setup. A shock wave is generated in cell *1* by the pressure of a pulsed magnetic field on the conducting membrane *3*, which transfers the pressure into liquid. The magnetic field is generated by discharge of a low-inductance capacitor battery *10* in the flat coil *4* placed between the shock membrane *3* and copper disk *5*. Controlled discharge gap *8* allows the shock wave pressure to be varied from 1 to 10 Mbar. Resistor *9* (*R*) provides for the production of a single pressure pulse. The plane shock wave with a duration of 4–5 μs propagates in the form of a 25- to 30-mm-diam disk toward the free surface of water *2*. Reflection of the shock wave from the surface gives rise to a discharge wave propagating downward and initiating the growth of cavitation nuclei, which leads to the formation of a cavitation cluster under the free water surface [4]. The cell can be heated through a massive flange *6* by three heating elements *7*.

An advantage of this experimental setup is the absence of wall effects upon the process studied. Indeed, for a cell diameter of 80 mm and a water column height of 25 mm, the process of shock wave reflection from the free water surface terminated 20–30 μs before the unloading wave arrived to the near-surface region. The experiments were performed with distilled water allowed to stand for not less than 24 h prior to experiment. By setting a controlled value of current through the heating elements *7*, water in the cell could be heated within 20–30 min to a definite temperature, which was subsequently maintained virtually constant. At every temperature, water was allowed to stand for 2 h (until the process of gas evolution ceased, which was evidence for the air–water system to reach the state of thermodynamic equilibrium. In order to reduce the evaporation of water, cell *1* was non-hermetically closed with a Lavsan film. Air bubbles evolved on heating were removed from the cell floor and walls with a pipette. The capacitive transducer *11* had a temperature equal to that of water.

The shock wave parameters and the experimental results are presented in Fig. 2, where curve *1* describes

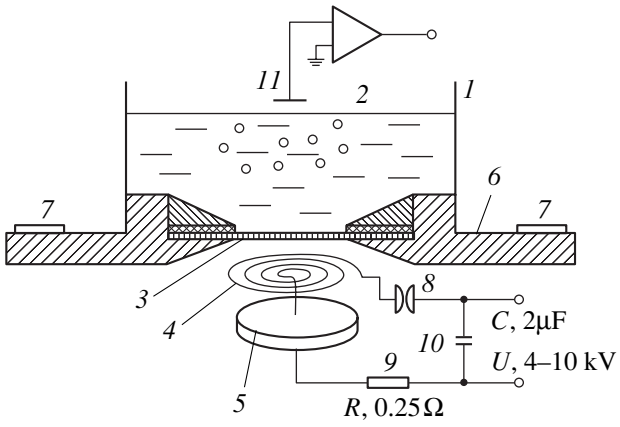

Fig. 1.

dynamics of the free water surface $X(t)$ upon reflection of the discharge wave in a pre-cavitation regime and curve *2* is a profile of the free water surface velocity (obtained by differentiating curve *1*), which corresponds to the shock wave profile in the absence of cavitation. The AA line indicates the time instant when the shock wave reflects from the free surface. The rise of the free surface (curve *1*) to a certain level reflects the elastic stretching of water in the field of a discharge wave propagating downward. Curve *3* corresponds to a threshold loading, which results in the inertial development of the cavitation cluster at 18.5°C, as evidenced by the appearance of a nonzero slope U in the curve of the free surface displacement [4–6]. This slope, observed on the right of the *AA* boundary line in Fig. 2, is related to an increase in the bubble size and in volume of the loaded water sample.

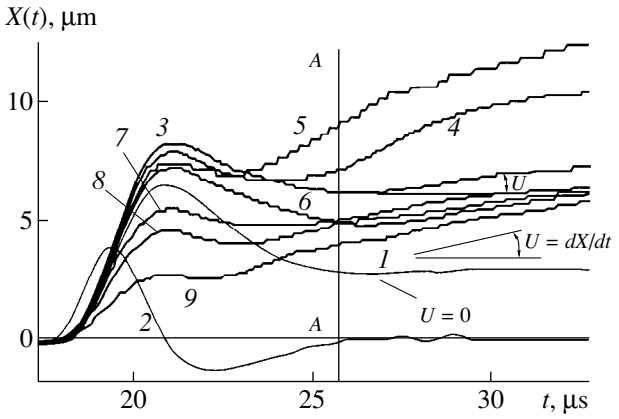

Fig. 2.

For the experimental scheme employed, the slope U of all curves showing the free surface displacement kinetics is related to the specific volume of bubbles α by a simple relationship $\alpha = U/c$ [5] (where U is the free surface velocity and c is the velocity of sound in water) characterizing the intensity of cavitation. The appearance of a nonzero slope U is selected as a criterion of the cavitation onset, and the amplitude of the corresponding shock wave is considered as a threshold amplitude [6]. Curves *4–9* reflect dynamics of the free water surface at various temperatures of water in the system studied (33, 42, 52, 66, 74, and 84°C, respectively). Initially, an increase in the temperature leads to a several-fold increase in intensity of the cavitation process (cf. curves *4* and *5* in Fig. 2, corresponding to 33 and 42°C) as evidenced by the U angle criterion. However, the intensity of cavitation at 52°C drop to almost the initial level, which reflects increasing cavitational strength of water. Further increase in the temperature again increases the intensity of cavitation and leads to a sharp growth in absorption of the shock wave intensity, as seen from the drop in amplitude of the free water surface displacement upon the shock wave reflection (curves *7–9*).

Absorption of the shock wave is usually related to increasing gas content in the medium [4], while a decrease in the cavitational strength of water is caused by the growth of cavitation nuclei [2]. In order to provide for a correct comparison of intensity of the cavitation development at various temperatures, the initial amplitude of the shock wave at 52 and 66°C was increased so as to make the free water surface displacement equal to the initial value at 18.5°C. The character of the observed temperature-dependent variation remained unchanged.

The drop in the cavitational strength of water observed upon heating to 42°C can be explained by increasing equilibrium radius of microscopic gas bubbles always present in water [7, 8], determining the cavitational strength and the initial dynamics of the cavitational process development. It would be reasonably to assume that the microscopic gas bubbles grow in size on heating. At 50°C, the bubble size increases so as to cause their flotation and a drop of the cavitational strength of water. This was confirmed by a sharp increase in the number and size of gas bubbles growing on the cell floor and walls in the course of heating to 50°C. As the water temperature increases above this level, the rate of gas evolution considerably decreases. Increasing temperature is accompanied by exponential growth in the saturated water vapor pressure and by a significant decrease in the surface tension σ. This facilitates the development of cavitation on mechanical inclusions and may compensate, on reaching certain temperature, for the "lack" of microscopic free gas bubbles in the medium, thus providing for the experimentally observed decrease in the cavitational strength of water. However, the fact of a sharp increase in absorption of the shock wave energy beginning with a temperature of 66°C (Fig. 2, curves *7–9*) can be explained by the increasing gas content α in water.

We may suggest that the equilibrium radius of stable microscopic gas bubbles in water is a nonmonotonic function of the temperature, with a maximum near 52°C, but a more probable assumption is that the equilibrium radius growing with the temperature results in increase in the bubble flotation velocity V. Proceeding from equality of the Stokes and Archimedes forces, this velocity can be expressed as

$$V = 2\rho g R^2/9\eta, \qquad (1)$$

where ρ is the density, η is the dynamic viscosity of liquid, R is the current radius of microscopic bubbles, and g is the acceleration of gravity. Assuming that the bubbles are formed by the ideal gas and the number of gas molecules N does not vary with the temperature, we may use a relationship $(P_0 + 2\sigma/R)4\pi R^3/3 = NkT$, which implies that $R \sim T^{1/2}$ for $2\sigma/R \gg P_0$ and $R \sim T^{1/3}$ for $2\sigma/R \ll P_0$ (where k is the Boltzmann constant and P_0 is the atmospheric pressure). According to equation (1) the stable cavitation nuclei have $R_0 \approx 1.5$ μ [8] for

$2\sigma/R_0 \approx P_0$ and their subsequent growth leads to $R \gg 2\sigma/P_0$ and $V \sim T^{2/3}$. This implies that the heating-induced growth rate of the cavitation nuclei is slower than the rate of increase in the velocity of convective flows, which is a linear function of the temperature for a horizontal layer [9] and reaches a level of several mm/s at 40–60°C. This velocity is sufficient for the microscopic bubbles with a diameter of 10–30 μm to be retained in the volume. This effect may explain a sharp growth in the gas content and the corresponding increase in the shock wave energy absorption observed in water at 66°C and above.

The final judgment on the operative mechanism of these phenomena can be made only upon accomplishing additional experimental investigations. It is interesting to note that a minimum in the cavitational activity of water at 52°C exactly coincides with the maximum of cavitational erosion and the maximum efficiency of cleaning contaminated surfaces in aqueous solutions of detergents. Probably, there exists a fundamental relationship between these phenomena and the anomalous behavior of the compressibility of water, which decreases with increasing temperature below 50°C and begins to grow with the temperature above this level [10].

Thus, an original experimental scheme employed in this work and advantages of the capacitance measuring technique allowed us to minimize the statistical scatter of the cavitation thresholds and reveal true trends in their temperature dependence for water.

REFERENCES

1. L. Y. Briggs, J. Appl. Phys. **21**, 721 (1950).
2. A. D. Pernik, *Cavitation Problems* (Sudostroenie, Leningrad, 1966).
3. M. Connoly and F. E. Fox, JASA **26** (5) (1954).
4. A. Besov and V. Kedrinskiĭ, in *Proceedings of the International Symposium on Bubble Dynamics and Interface Phenomena, Birmingham, UK, 1994*, pp. 93–103.
5. A. S. Besov and V. V. Zaĭtsev, Akust. Neodnor. Sred, DSS (Novosibirsk) **112**, 43 (1997).
6. A. S. Besov, V. K. Kedrinskiĭ, and E. I. Pal'chikov, Pis'ma Zh. Tekh. Fiz. **15** (16), 23 (1989) [Sov. Tech. Phys. Lett. **15**, 630 (1989)].
7. A. S. Besov, V. K. Kedrinskiĭ, and E. I. Pal'chikov, Pis'ma Zh. Tekh. Fiz. **10** (4), 240 (1984) [Sov. Tech. Phys. Lett. **10**, 100 (1984)].
8. A. S. Besov, V. K. Kedrinskiĭ, and Y. Matsumoto, DSS (Novosibirsk) **104**, 16 (1992).
9. A. I. Leont'ev and A. G. Kirdyashkin, in *Proceedings of the 3rd All-Union Conference on Heat Transmission and Mass Transfer, Moscow, 1968*, Vol. 1, pp. 661–664.
10. G. N. Zatsepina, *Physical Properties and Structure of Water* (Mosk. Gos. Univ., Moscow, 1987).

Translated by P. Pozdeev

Technical Physics Letters, Vol. 26, No. 6, 2000, pp. 531–532. Translated from Pis'ma v Zhurnal Tekhnicheskoĭ Fiziki, Vol. 26, No. 12, 2000, pp. 76–81.

Effect of Thermal Treatment on the Exoelectron Emission Spectrum of a $Fe_{64}Co_{21}B_{15}$ Amorphous Metal Alloy

V. I. Boldyrev, A. S. Veksler, and A. A. Gavrilyuk

Irkutsk State University, Irkutsk, 664033 Russia

Received January 10, 2000

Abstract—The spectrum of the photoinduced exoelectron emission (PEE) current from heat-treated ribbons of a $Fe_{64}Co_{21}B_{15}$ amorphous metal alloy was studied. The shape and intensity of the PEE spectrum depend on the material treatment conditions. It is suggested that internal stresses and surface oxidation are the main factors affecting the PEE spectrum. © *2000 MAIK "Nauka/Interperiodica".*

The stable interest in amorphous metal alloys (AMAs) is explained by their possessing a unique combination of properties and offering the ability of wide practical applications. One of the main tasks of investigations devoted to AMAs consists in assessing stability of their properties with respect to thermal treatments. The purpose of our work was to study the kinetics of temperature induced structural changes in AMAs of the $Fe_{64}Co_{21}B_{15}$ system by the method of photoinduced exoelectron emission (PEE). The AMA samples were obtained by rapid quenching from melt and had the form of 10- to 20-mm-wide 30-μm-thick ribbons. The PEE measurements offer a method highly sensitive toward structural changes in AMAs upon their thermal treatment [1–3]. At the same time, the effect of thermal treatment on the spectrum of exoelectron yield (or the initial exoemission photocurrent [4]) $I(\lambda)$ has remained virtually uninvestigated.

The PEE spectra were studied on an experimental setup described in detail elsewhere [5]. The measurements of the PEE current I as function of the stimulating light wavelength λ were performed for the initial (not heat-treated) ribbons and the samples heat-treated in vacuum (10^{-4} Pa) and cooled to room temperature (the latter samples were measured either immediately or after holding for 24 h at room temperature).

In this work, we have studied the PEE spectra of the AMA samples were heat-treated in the following regimes.

1. A sample was heated in vacuum to a temperature of 970 K markedly exceeding the base alloy crystallization temperature [3]. The $I(\lambda)$ spectrum was measured upon cooling the sample to room temperature. The thermal treatment resulted in increasing PEE current intensity in the entire wavelength studied. Figure 1 shows the PEE yield spectrum normalized to the maximum value in the heat-treated sample (i.e., the relative initial exoemission photocurrent versus light wavelength). The subsequent 24-h holding at room temperature resulted in a significant decrease in the I value.

2. A sample was heated in vacuum to a temperature of 690 K, corresponding to the initial stages of the base alloy crystallization [3], and measured upon cooling to room temperature. This thermal treatment also resulted in increasing PEE current intensity as compared to that for the initial sample (Fig. 2), but to even greater extent than in the preceding case. The subsequent 24-h holding at room temperature resulted in a significant decrease in the I value over the entire wavelength range studied.

3. A sample was heated under isothermal conditions in air at 470 K for 100 or 200 h and then cooled to room temperature and measured. (Fig. 3). Here, the I value of the heat-treated samples increased in the entire wave-

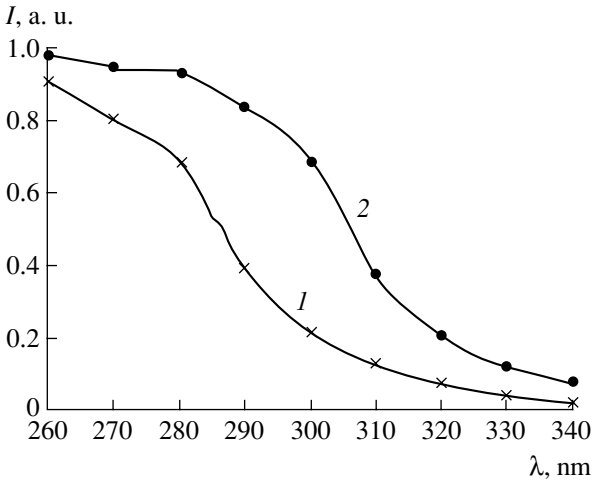

Fig. 1. Plots of the relative initial exoemission photocurrent versus excitation light wavelength for a $Fe_{64}Co_{21}B_{15}$ alloy: (*1*) initial sample; (*2*) sample heat-treated in vacuum at 970 K and measured upon cooling to room temperature.

1063-7850/00/2606-0531$20.00 © 2000 MAIK "Nauka/Interperiodica"

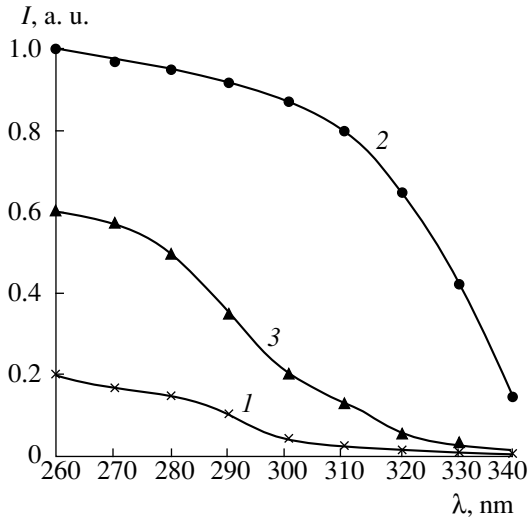

Fig. 2. Plots of the relative initial exoemission photocurrent versus excitation light wavelength for a $Fe_{64}Co_{21}B_{15}$ alloy: (*1*) initial sample; (*2*) sample heat-treated in vacuum at 690 K and measured upon cooling to room temperature; (*3*) heat-treated sample kept for 24 h under isothermal conditions at room temperature.

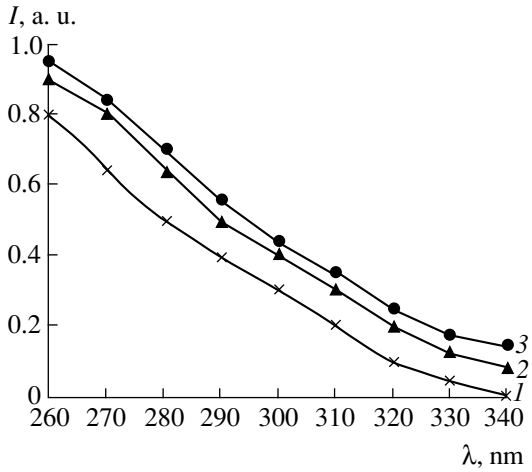

Fig. 3. Plots of the relative initial exoemission photocurrent versus excitation light wavelength for a $Fe_{64}Co_{21}B_{15}$ alloy: (*1*) initial sample; (*2*, *3*) samples heat-treated under isothermal conditions in air at 473 K for 100 and 200 h, respectively, and measured upon cooling to room temperature.

length range as compared to that of initial ribbon, the effect enhancing with the duration of isothermal exposure.

The results described above can be interpreted as follows. An increase in the initial exoemission photocurrent intensity after thermal treatments is related to a decrease in the exoelectron work function E of the sample surface. A change ΔE in the exoelectron work function can be estimated by the formula

$$\Delta E = (\hbar c/\lambda_{av}^2)\Delta\lambda,$$

where c is the velocity of light, λ_{av} is the average value of the excitation light wavelength for the same level of the exoelectron yield from the initial and heat-treated samples, and $\Delta\lambda$ is the difference of the light wavelength for the same level of signal intensity in the initial and heat-treated samples. For the $Fe_{64}Co_{21}B_{15}$ alloy heated to 970 K, we obtain for λ_{av} = 300 nm a wavelength shift of $\Delta\lambda$ = 20 nm, which corresponds to an 0.25 eV decrease in E as compared to the value in the initial sample. At the same time, the treatment at 690 K leads to an 0.60 eV decrease in E (assessed at λ_{av} = 280 nm), while the isothermal treatment in air at 470 K for 200 h decreases the E value by only 0.20 eV.

Summarizing the experimental data obtained, we may suggest that an increase in the exoelectron yield I upon thermal treatment of AMA samples in the first two regimes is related to the level of internal stresses in the samples increasing as a result of crystallization processes [6]. Indeed, a decrease in the exoelectron work function with increasing level of internal stresses in crystalline alloys was reported in [4, 7]. The isothermal holding at room temperature is accompanied by relaxation of the crystallization-induced internal stresses, which leads to decreasing exoelectron yield. The increase in the exoelectron yield upon isothermal heating of the AMA samples in air can be attributed to the process of surface oxidation.

Thus, the heat-treatment-induced increase in the photoinduced exoelectron current is always related to changes in the surface structure of AMA caused by this treatment. The maximum growth in the exoelectron emission intensity in the entire wavelength range of the exciting radiation (as well as the most pronounced change in the electron work function) was observed in AMAs treated at temperatures corresponding to the initial crystallization stages. This is explained by an increase in the level of internal stresses caused by the crystallization processes.

REFERENCES

1. G. Z. Gorecki, Poverkhnost', No. 7, 63 (1993).
2. V. I. Boldyrev, A. S. Veksler, and O. V. Lemzyakov, Neorg. Mater., No. 11, 1300 (1998).
3. V. I. Boldyrev, A. S. Veksler, N. I. Noskova, *et al.*, Fiz. Met. Metalloved. **87** (5), 83 (1999).
4. G. L. Sagalovich, V. P. Melekhin, and Yu. D. Dekhtyar, *Exoelectron Spectroscopy of Defects in Solids* (NTO, Riga, 1981).
5. V. S. Kortov, A. I. Slesarev, and V. V. Rogov, *Exoemission Control of the Surface of Articles upon Processing* (Naukova Dumka, Kiev, 1986).
6. V. I. Boldyrev and A. S. Veksler, Izv. Vyssh. Uchebn. Zaved. Fiz., No. 9, 94 (1999).
7. L. Grünberg, in *Exoelectron Emission* (Inostrannaya Literatura, Moscow, 1962), pp. 118–144.

Translated by P. Pozdeev

Technical Physics Letters, Vol. 26, No. 6, 2000, pp. 533–534. Translated from Pis'ma v Zhurnal Tekhnicheskoĭ Fiziki, Vol. 26, No. 12, 2000, pp. 82–85.

Electrical Phenomena in a Hydrogen-Containing Heterogeneous System Palladium–Strontium Cerate–Barium-Yttrium Hydrocuprate

Yu. M. Baĭkov

Ioffe Physicotechnical Institute, Russian Academy of Sciences, St. Petersburg, 194021 Russia

Received February 11, 2000

Abstract—The proton conductivity of barium-yttrium hydrocuprate $H_xYBa_2Cu_3O_{7+y}$ ($x \le 2$, $-0.1 \le y \le 0.1$) was determined for the first time. The proton conductivity (10^{-6} S cm^{-1} at 470 K, with an activation energy of –0.6 eV) accounts for 0.1% of the total dc conductivity. Owing to the proton conductivity of strontium cerate ($H_zSrCe_{0.9}Y_{0.1}O_3$, $z < 0.1$) and hydrocuprate layers in the Pd/cerate/hydrocuprate/cerate/Pd sandwich structure, this heterogeneous system exhibits the properties of an electric accumulator with emf = 0.6–1.2 V. © *2000 MAIK "Nauka/Interperiodica".*

Important components of heterogeneous systems studied within the framework of the "Hydrogen Energetics" research and development program, one of the science and technology priority directions, are the intermediate compounds capable of providing effective electrical and/or chemical contacts between essentially dissimilar materials, for example, between metal hydride based hydrogen sources with electron conductivity and oxide membranes with proton conductivity. Unfortunately, no materials possessing electron- proton conductivity, especially at moderately high temperatures (200–400°C) are practically available.

In this context, it was interesting to try a barium-yttrium hydrocuprate composition $H_xYBa_2Cu_3O_{7+y}$ ($x \le 2$, $-0.1 \le y \le 0.1$) as a mixed electron-proton conductor. This attempt was based on the phenomenon of high diffusion mobility of hydrogen in this compound previously discovered by the author [1]. The hydrogen self-diffusion coefficient in this compound is 10^{-8} cm^2/s at 470 K, which, according to the Nernst–Einstein law, corresponds to a proton conductivity of the order of 10^{-4} S/cm. Since the total (electronic *p*-type) conductivity of the above hydrocuprate at 470 K is markedly greater (10^{-3} S/cm) [2], it might be expected that the proton conductivity will account for about 10%. However, this effect was not reported until now. This circumstance gave impact to the experiments described below.

Te ion (proton) component contribution to the total conductivity was evaluated by a well-known method. According to this, a sample of the material studied (hydrocuprate) is pressed between solid electrolyte layers possessing a transfer number for the corresponding ions (protons) of the order of unity. In this work, the role of solid electrolyte was played by $H_zSrCe_{0.9}Y_{0.1}O_3$ ($z < 0.1$) referred to below as strontium cerate. The current-carrying electrodes were made of Pd, the hydride-forming properties of which were expected to provide for the symmetry of the measuring cell during the dc conductivity measurements. However, it was found that the Pd/cerate/hydrocuprate/cerate/Pd sandwich structure was polarized by dc current and retained the emf for a large time (one day or even longer). This phenomenon rendered the cell an object of investigation rather than merely a tool.

Ceramic cerate and cuprate pellets with a diameter of 10 mm and a thickness of 1 mm were prepared by method of solid-state reactions involving the corresponding oxides. The edge surfaces of the samples were coated with palladium black and pressed between Pd foil. The reference electrodes (~100-μm-thick wire probes) were placed between pellets. Cerate pellets were saturated with hydrogen by exposure to water vapor at high temperatures (2.7 kPa, 850 K, 24 h) prior to assembling a measuring cell. Then the cell was placed in a vessel connected to a pumping stage and a gas admission system. The hydrogenation of cuprate and Pd was effected immediately in the measuring vessel (27 kPa, 450 K) as described in [2].

A summary of the main experimental results, clearly illustrating the observed features of conductivity of the whole cell and its parts is presented in the table. Prior to the cuprate hydrogenation, the total cell resistance at 470 K could hardly be measured because of a very low electron conductivity of the initial cerate (10^{-8} S/cm [3]), whereas the proton conductivity of hydrogenated cerate was blocked by cuprate. As the cuprate hydrogenation proceeded, the situation changed and, when the hydrogen content in the cuprate reached $x = 1.8$, the cell resistance dropped by two orders of magnitude. The resistance of the cuprate layer, measured separately with the aid of reference

1063-7850/00/2606-0533$20.00

Resistances (kΩ) of the whole cell and partial resistances of component cerate and cuprate layers with respect to the electron and proton conductivity before and after hydrogenation

Charge carrier	Layer		Cell
	cerate	cuprate	
	Before hydrogenation		
Electrons	>25000	10^{-5}	>25000
Protons	200	∞	
	After hydrogenation		
Electrons	25000	0.1	
Protons	200	100	300

wire electrodes, increased upon the hydrogenation by almost five orders of magnitude to reach 100 Ω. This behavior is fully consistent with the hydrogenation-induced drop in the conductivity of cuprate reported in [2]. At the same time, the resistance of the cuprate layer determined from the voltage drop across this layer and the overall current passing through the whole cell was about 100 kΩ.

The above results are most simply explained by hydrogen intercalation into the cuprate layer, rendering it a proton-conductor and creating a through proton conductivity channel across the cell (blocked, prior to hydrogenation, by the purely electron-conducting layer of $YBa_2Cu_3O_7$). Therefore, the conductivity of the cuprate layer operating in the cell is reasonably assigned to the proton conductivity component of hydrocuprate. This conductivity was 10^{-6} S/cm at 470 K, which is lower as compared to the estimate based on the diffusion coefficient (see above). The total conductivity of the cuprate layer, measured without cerate layers blocking the electron current, was 10^{-3} S/cm. Thus, the proton conductivity contribution does not exceed 0.1% of the total dc conductivity.

The phenomenon of polarization, observed for the whole cell upon prolonged passage of a dc current through the sample structure, was rather unexpected, since the cell was initially symmetric. Moreover, the hydrogenated Pd was initially suggested to maintain the symmetry, by serving as a source of protons on the anode and their acceptor, on the cathode. However, it was found that an emf of the order of 1 V was developed across the cell electrodes, which retained almost unchanged value in some cases over a time period of not less than 100 h. The sign of this emf could be determined by polarization with a reverse current. It was established that the emf of a cell polarized at 470 K in water vapor was 0.8–1 V, and reached up to 1.2 V upon polarization in an oxygen atmosphere (or an oxygen-air mixture). The gas medium, to which the cell was exposed, not only determined the magnitude of emf, but influenced stability of the cell operation in the open-circuit regime as well. Indeed, the value of emf generated upon exposure to water vapor at a pressure of 0.2–2.5 kPa was retained for many days. At the same time, the emf generated in the cell exposed in the atmosphere of H_2 or O_2 (air) dropped at 470 K to 100 mV within a few hours. Detailed mechanisms of this phenomenon and the possibility of using sensitivity of the cell to the gas phase composition in chemical sensors are now investigated.

The discharge currents of the resulting electric accumulator in a load or in the short-circuit regime are determined by internal resistance of the cerate layers. In our experiments, these currents reached tens of nanoamperes at 470 K. By increasing the working temperature and using cerate compositions possessing a higher conductivity (such as, e.g., $BaCe_{1-x}Nd_xO_3$), it is possible to pass to microampere currents at a voltage of 1 V, which may be of interest for practical applications.

This work was supported by the Russian Foundation for Basic Research, project no. 97-03-33466a.

REFERENCES

1. Yu. M. Baĭkov, Zh. Neorg. Khim. **43**, 192 (1998).
2. Yu. M. Baĭkov, S. E. Nikitin, Yu. P. Stepanov, *et al.*, Fiz. Tverd. Tela (St. Petersburg) **39**, 823 (1997) [Phys. Solid State **39**, 729 (1997)].
3. K. D. Kreuer, Chem. Mater. **8**, 610 (1996).

Translated by P. Pozdeev

Technical Physics Letters, Vol. 26, No. 6, 2000, pp. 535–538. Translated from Pis'ma v Zhurnal Tekhnicheskoĭ Fiziki, Vol. 26, No. 12, 2000, pp. 86–94.

A Method for Reducing Pocklington's Equation of Electric Vibrators to a Singular Integral Equation

V. A. Neganov, I. V. Matveev, and S. V. Medvedev

Samara State University, Samara, Russia

Received November 15, 1999

Abstract—A mathematically correct approach to the analysis of Pocklington's equation for thin electric vibrators, based on the theory of singular integral equations, is suggested. A new singular integral equation is obtained for the derivative of the surface current with respect to the longitudinal coordinate. Numerical treatment demonstrates rapid convergence and computational simplicity of the proposed method. © *2000 MAIK "Nauka/Interperiodica".*

The design of electric vibrators normally entails computing current distribution. Pocklington's and Harrington's integro-differential equations as well as Hallen's integral equation are available for this purpose [1–3]. The most widely employed technique to solve these equations is the method of moments together with its modifications, using appropriate basis and weighting functions. In our opinion, the main disadvantage of this approach is that singular kernels (written in an implicit form) are replaced by regular (Fredholm) kernels to obtain the Fredholm-type integral equations of the first kind. Solving these equations is known to present an Ill-posed problems [4]. Also, it remains to be proven that the result obtained is a true solution of the original problem and has physical significance. As a further step in development of this approach, Éminov [5] suggested a new class of basis functions (called the eigenfunctions of an integro-differential operator) to be used in solving such problems. However, use of the new functions considerably complicates the numerical algorithm.

In contrast, this study rests on the mathematical formalism of the theory of singular integral equations developed in the context of microstrip lines and slotlines for SHF and EHF integrated circuits [6, 7]. Specifically, we use an algorithm to transform Pocklington's equation into a singular integral equation with a singularity of the Cauchy type [8].

Formulation of the Problem in Terms of an Integral Equation of the First Kind

Consider a straight wire of length $2l$ and radius a with the feed points $z = l_0 - b$ and $z = l_0 + b$, as shown in Fig. 1. The antenna is excited by an rf oscillator. A singular integral equation will be derived within the framework of a commonly accepted thin electric vibrator approximation ($a \ll l, \lambda$). According to this, the longitudinal electric current density η_z^e and the equivalent magnetic current density η_z^m in the gap are replaced by a thin filament of the longitudinal electric current $I_z(z) = 2\pi a \eta_z^e(z)$. Flowing in the axis of the wire, the current is assumed to be continuous in the gap and to vanish at the ends of the vibrator. We neglect the edge currents of the cylinders. At $\rho = a$, the E_z component of the electric field produced by the current filament is zero for all $z \in [-l, l]$, except for a $2b$-wide gap region, where we set $E_z = E^{\text{ext}}(z)$, the latter denoting an external field.

Being independent of φ, the radiation can be described by Pocklington's equation [1]

$$\left(\frac{d^2}{dz^2} + \gamma^2\right)\int_{-l}^{l} I_z(z)\frac{e^{-i\gamma R}}{4\pi R}dz' = -i\omega\varepsilon_0\varepsilon E^{\text{ext}}(z), \qquad (1)$$

where $R = \sqrt{(z-z')^2 + a^2}$, $\gamma^2 = k^2\varepsilon\mu$, $k = \omega/c$ is the

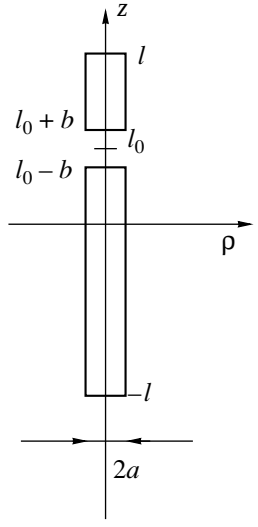

Fig. 1.

1063-7850/00/2606-0535$20.00 © 2000 MAIK "Nauka/Interperiodica"

wavenumber, and ε and μ are the permittivity and permeability of the environment, respectively.

According to a well-known Green's function expansion [5]:

$$\frac{e^{-i\gamma R}}{R} = -\frac{i}{2}\int_{-\infty}^{\infty} e^{-ih(z-z')} J_0(-ia\sqrt{h^2-\gamma^2}) \times H_0^{(2)}(-ia\sqrt{h^2-\gamma^2})dh, \quad (2)$$

where $J_0(x)$ and $H_0^{(2)}(x)$ are the Bessel function of the first kind and the first-order Hankel function of the second kind, respectively. Substituting this expression into equation (1), we arrive at the integral equation

$$\int_{-l}^{l} I_z(z')G_1(z,z')dz' = \omega\varepsilon\varepsilon_0 E^{\text{ext}}(z), \quad (3)$$

where

$$G_1(z,z') = \frac{1}{8\pi}\int_{-\infty}^{\infty} (\gamma^2-h^2) J_0(-ia\sqrt{h^2-\gamma^2}) \times H_0^{(2)}(-ia\sqrt{h^2-\gamma^2}) e^{-ih(z-z')}dh. \quad (4)$$

Equation (3) is a nonhomogeneous integral equation of the first kind.

Singular Integral Equation

Obviously, the integrand function $G_1(z, z')$ in (4) grows as $|h|$ if $|h| \longrightarrow \infty$ so that the integral diverges. To eliminate the divergence, let us replace $I_z(z)$ in equation (3) by its derivative $I_z' = dI_z/dz$. Since $I_z(-l) = I_z(l) = 0$ (zero current at the vibrator ends), we can write

$$\int_{-l}^{l} I_z(z')e^{ihz'}dz' = \frac{i}{h}\int_{-l}^{l} I_z'(z')e^{ihz'}dz'. \quad (5)$$

Using (5), we recast (3) as

$$\omega\varepsilon_0\varepsilon E^{\text{ext}}(z) = \int_{-l}^{l} I_z'(z')G(z,z')dz', \quad (6)$$

where

$$G(z,z') = \frac{1}{8\pi}\int_{-\infty}^{\infty} e^{-ih(z-z')}g(h)dh, \quad (7)$$

$$g(h) = i\frac{\gamma^2-h^2}{h} J_0(-ia\sqrt{h^2-\gamma^2}) \times H_0^{(2)}(-ia\sqrt{h^2-\gamma^2}). \quad (8)$$

In order to solve equation (6), let us determine the asymptotic behavior of $g(h)$ for $|h| \longrightarrow \infty$. Using representations of the Bessel and Hankel functions of the complex argument [9],

$$J_0(-ix) = I_0(x), \quad H_0^{(2)}(-ix) = \frac{2i}{\pi}K_0(x),$$

we obtain,

$$\lim_{|h|\to\infty} g(h) = \text{sgn}(h), \quad (9)$$

where

$$\text{sgn}(h) = \begin{cases} 1, & h > 0 \\ -1, & h < 0. \end{cases}$$

The corresponding asymptotic kernel is

$$G_\infty(z,z') = \frac{1}{8\pi}\int_{-\infty}^{\infty} \text{sgn}(h)e^{-ih(z-z')}dh. \quad (10)$$

Using the relationship [10]

$$\int_{-\infty}^{\infty} e^{-ih(z-z')}\text{sgn}(h)dh = \frac{2i}{z-z'}, \quad (11)$$

we obtain

$$G_\infty(z,z') = \frac{i}{4\pi(z-z')}. \quad (12)$$

Thus, the kernel $G_\infty(z, z')$ in equation (6) implicitly has a singularity of the Cauchy type (12) and, hence, (6) is a singular integral equation.

After simple transformations, (6) can be rewritten as

$$4i\omega\varepsilon_0\varepsilon E^{\text{ext}}(z) = \frac{1}{\pi}\int_{-l}^{l}\frac{I_z'(z')}{z'-z}dz' + \int_{-l}^{l} I_z'(z')K(z,z')dz', \quad (13)$$

where

$$K(z, z') = \frac{i}{2\pi}\int_{-\infty}^{\infty} e^{ih(z'-z)}\Delta g(h)dh,$$
$$\Delta g(h) = \frac{\gamma^2 - h^2}{h} J_0(-ia\sqrt{h^2-\gamma^2}) \quad (14)$$
$$\times H_0^{(2)}(-ia\sqrt{h^2-\gamma^2}) + \mathrm{sgn}(h).$$

Relationship (13) is a singular integral equation of the first kind for determining I_z, the integrand function in the kernel (14) tending to zero as $|h| \longrightarrow \infty$ due to $\Delta g(h) \longrightarrow 0$. To our knowledge, no such equation has been reported.

Solving the Singular Integral Equation: Numerical Results

Let the vibrator be symmetric: $l_0 = 0$. To solve the singular integral equation, we will define new variables τ and τ' as follows: $z = l\tau$ and $z' = l\tau'$. With $J(\tau') = I_z'(l\tau')$, equation (13) becomes

$$\frac{1}{\pi}\int_{-l}^{l}\frac{J(\tau')}{\tau'-\tau}d\tau' \quad (15)$$
$$= 4i\omega\varepsilon_0\varepsilon E^{\mathrm{ext}}(\tau) - l\int_{-l}^{l} J(\tau')K(\tau, \tau')d\tau' \equiv F(\tau),$$

where

$$K(\tau, \tau') = \frac{i}{2\pi}\int_{-\infty}^{\infty} e^{ihl(\tau'-\tau)}\Delta g(h)dh. \quad (16)$$

Applying the inversion formula of the Cauchy integral to singular integral equation (15) yields [6].

$$J(\tau) = \frac{1}{\pi\sqrt{1-\tau^2}}\left[a_0\tau - \int_{-l}^{l}\frac{\sqrt{1-\tau'^2}}{\tau'-\tau}F(\tau')d\tau'\right], \quad (17)$$

where a_0 is an unknown constant. This quantity is evaluated from the condition that I_z vanishes at $z = -l$ and $z = l$, which implies

$$\int_{-l}^{l} J(\tau)d\tau = 0.$$

This expression also states that the total charge on the vibrator is zero. Being a nonhomogeneous Fredholm equation of the second kind, (17) lends itself to numerical treatment readily.

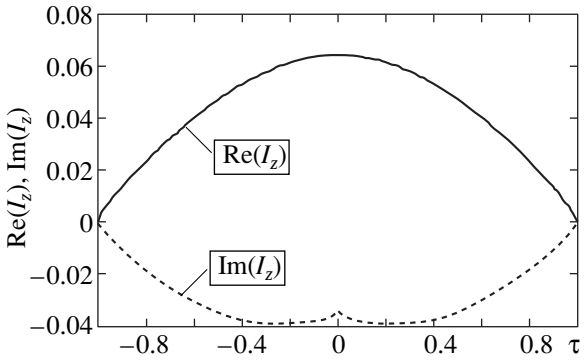

Fig. 2.

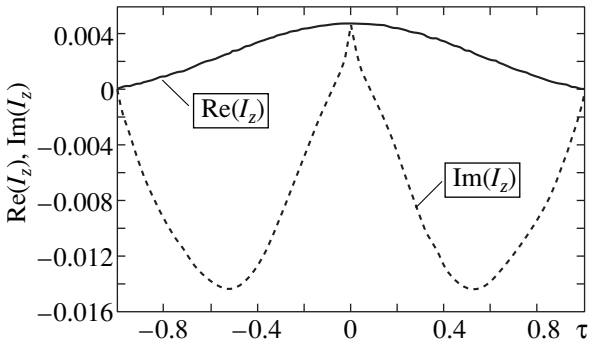

Fig. 3.

Based on (17), we have computed the surface current density. Figures 2 and 3 show typical distributions of the real part (solid curves) and the imaginary part (dashed curves) of I_z for $l/\lambda = 1/4$ or 1/2, respectively, with $b/l = 1/100$ and $a/\lambda = 1/400$. The computation was carried out under the assumptions that E^{ext} is uniform over the gap and that $\omega\varepsilon_0\varepsilon E^{\mathrm{i}} = a/\lambda$. The results agree well with [11].

CONCLUSION

We suggested a correct approach to analysis of a thin electric vibrator, using singular integral equations to compute surface current density. This strategy provides for a considerably improved convergence of the solutions and eliminates the phenomenon of relative convergence that may occur take place in solving the Fredholm-type equations of the first kind [6, 7]. In principle, the technique presented here makes it possible to theoretically estimate the accuracy of the solution. The approach can be extended with ease to coupled vibrators in the free space or over conducting surfaces.

REFERENCES

1. *Computer Techniques for Electromagnetics*, Ed. by R. Mittra (Pergamon, Oxford, 1973; Mir, Moscow, 1977).

2. D. M. Sazonov, *SHF Antennas and Devices: A Handbook for Radio Engineering Specialties of High School* (Vysshaya Shkola, Moscow, 1988).

3. G. A. Erokhin, O. V. Chernyshev, N. D. Kozyrev, and V. G. Kocherzhevskiĭ, *Antenna Devices and Radio Wave Propagation: A Handbook*, Ed. by G. A. Erokhin (Radio i Svyaz', Moscow, 1996).

4. A. N. Tikhonov and V. Ya. Arsenin, *Solutions of Ill-Posed Problems* (Nauka, Moscow, 1986, 3rd ed.; Halsted Press, New York, 1977).

5. S. I. Éminov, Radiotekh. Élektron. (Moscow) **38**, 2160 (1993).

6. V. A. Neganov, E. I. Nefedov, and G. P. Yarovoĭ, *Strip Lines and Slot Lines for Super High and Extremely High Frequencies* (Nauka, Moscow, 1996).

7. V. A. Neganov, E. I. Nefedov, and G. P. Yarovoĭ, *Modern Methods of Designing Transmission Lines, SHF and EHF Resonators* (Pedagogika-Press, Moscow, 1998).

8. V. A. Neganov and I. V. Matveev, Fiz. Voln. Protsessov Radiotekh. Sist. **2** (2), 27 (1999).

9. *Handbook of Mathematical Functions*, Ed. by M. Abramowitz and I. A. Stegun (Dover, New York, 1971; Nauka, Moscow, 1979).

10. F. D. Gakhov and Yu. I. Cherskiĭ, *Convolution Type Equations* (Nauka, Moscow, 1978).

11. S. I. Éminov, *Method of Eigenfunctions of Singular Operators in the Diffraction Theory in Application to Electrodynamic Analysis of Vibrators and Slit Antennas*, Author's Abstract of Doctoral Dissertation in Mathematical Physics (Novgorod, 1995).

Translated by A. Sharshakov